NATURAL AND ENGINEERED SURFACES FOR ENHANCED PHASE CHANGE HEAT TRANSFER

BY

JUNHO OH

DISSERTATION

Submitted in partial fulfillment of the requirements
for the degree of Doctor of Philosophy in Mechanical Engineering
in the Graduate College of the
University of Illinois at Urbana-Champaign, 2019

Urbana, Illinois

Doctoral Committee:

Assistant Professor Nenad Miljkovic, Chair and Director of Research
Professor Anthony M. Jacobi
Professor Paul V. Braun
Dr. Donald M. Cropek, CERL-ERDC, US Army Corps of Engineers
Dr. Marianne Alleyne

ABSTRACT

Phase change of water is a ubiquitous process that occurs throughout nature and in a wide range of engineering systems. Over the last century, many researchers have studied the effect of surface wettability on the enhancement of phase change heat transfer. Interestingly, interfacial phenomena tailored for the manipulation of water can be found in nature. Many natural plant and insect surfaces have evolved to repel or attract water in order to adapt to external evolutionary pressures and to help them survive. This dissertation focuses on nature-inspired surfaces with desirable wettability characteristics that can enhance phase change heat transfer. We begin by investigating the wettability of natural surfaces to understand why and how hydrophobicity is achieved. We reveal that hydrophobicity of cicada wings, stemming from both chemistry and structure, is governed by life history and reproductive strategy, rather than habitat. We utilize the knowledge of natural surface chemistries to develop hydrophobic materials for environmentally friendly superhydrophobic coatings. Furthermore, we answer a key scientific controversy regarding the wettability of rare earth oxides by conclusively showing that hydrophobicity is driven by hydrocarbon adsorption. The findings were leveraged to design, develop, and demonstrate a novel concepts of condensation heat transfer capable of enhancing performance of state-of-the-art sytems by leveraging thin film condensation and jumping-droplet induced localized hot spot cooling.

The journey has just begun…

ACKNOWLEDGEMENTS

First to last, thank to God for giving me the strength and wisdom to study for the last four years. I want to thank my family, who have supported me during my entire life and Ph.D. years. I especially want to recognize my father, Dr. Sangkyoung Oh, the "Big Dr. Oh," who has enlightened me as a scientist and engineer and raised me as a grown-up. Without you, I would not be able achieve the dream of "Little Dr. Oh" becoming a real doctor. I would also like to thank my mother, Kyounghae Kim, and my sister, Hyunju Oh for their encouragement and support. I would also like to thank the most amazing woman, my best friend, and the love of my life, Dr. Nayoun Kim, for her love and support.

I would like to thanks my doctoral advisor, Prof. Nenad Miljkovic for great discussions on science, all the support, helpful advice, and fun pep talks. I want to thank all of the dissertation committee members who have collaborated and advised me with valuable comments; Prof. Anthony M. Jacobi, Prof. Paul V Braun, Dr. Donald M. Cropek, and Dr. Marianne Alleyne. I want to thank the MechSE department and research centers such as POETS, I2CNER and ACRC for their continued financial support. I also want to thank my other collaborators in the Army Construction Engineering Research Lab (CERL) for very fruitful research discussions. Also, I would like to specifically acknowledge Prof. Dani Orejon at the University of Edinburgh and Yukihiro Yokoyama from the Japanese Patent Office for his help and discussions, for a chapter of my dissertation. I would like to thank Dr. Ryan Enright at Nokia Bell Labs Ireland, for all the research activities and insightful discussion we had during my internship and after. I would also like to acknowledge my mentors and advisors from South Korea throughout my academic career; Dr. Changkook Ryu, Dr. Moon Ki Kim, Dr. Jaeboong Choi, and Dr. Jinkee Lee.

For the past four years at Illinois, I have continually encountered people who are bright, kind, and awesome. Specially thanks to Je Won Hong for all the fun we had together whichever it was, Chullhee Cho, my fantastic wedding singer, late night companion at MEL like “working dead” and stress reliever by going karaoke together. Dr. Alperen Gunay, my Altaic younger brother, without you, my life during my Ph.D. would have been much more boring. My DH’s, Dr. Soumyadip Sett, thank you for your advice and discussions as my senior postdoc, Kalyan Boyina, thank you for your care, and Kazi Fazle Rabbi, my late night MEL buddy in later years, “Kazi, Just go home”. I will miss you guys more than any other. I also have to mention my Korean fellow lab mates, Moonkyung Kim and Hyeongyun Cha, Longnan Li, thank you for your help during the first year and beyond. Junyoung Kim, and Hochan Chang, thank you very much as well and all the same to you. I would also like to thank my labmates, Dr. Shreyas Chavan, Jingcheng Ma, and Dr. Xiao Yan, whom I shared great research discussions with. Thomas Foulkes and Dr. Patrick Birbarah, you two were great collaborators with whom we could make many projects possible together. I would also like to mention all of my fellow ETRL’ers for your support and friendship. In addition, I would like to thank the undergraduate and graduate students that I mentored during my four years at Illinois: Jonah, Sabrina, Adam, Wooyoung, Geonwoo and Youngsung. I would like to share my gratitude to my neighborhood labmate Juyoung, Yerim, Keong, and Peter for great discussions. I would like to acknowledge Shin Hum Cho who is currently studying at UT Austin for helpful discussions regarding the physics and chemistry of surface science.

Last but not least, I would like to thank again all of my family and people around me who supported and motivated me. This is just the beginning of my long journey to the ultimate science and engineering that I have dreamed of exploring. I cannot wait for the next steps to come. The journey has just begun.

TABLE OF CONTENTS

LIST OF SYMBOLS AND ABBREVIATIONS

R	Droplet Radius (μm)
θ_{app}	Apparent Contact Angle (°)
θ^a	Advancing Contact Angle (°)
θ^r	Receding Contact Angle (°)
Oh	Ohnesorge Number
R	Surface Roughness
Φ	Solid Fraction
D	Diameter
P	Perimeter
H	Height
κ	Permeability
XPS	X-ray Photoelectron Microscopy
ToF-SIMS	Time-of-Flihgt Secondary Ion Mass Spectroscopy
SEM	Scanning Electron Microscopy

AFM	Atomic Force Microscopy
TGA	Thermogravimetric Analysis
PMMA	Polymethylene Methacrylate
HTMS	Heptadecafluoro Trimethoxy Silane
SAM	Self-Assembled Monolayer
RMS	Root Mean Squre
θ_{th}	Theoretical Maximum Contact Angle
α	Opening Angle
θ_{CB}	Contact Angle at Cassie-Baxter State
CVD	Chemical Vapor Deposition
DCC	Dicyclohexylcarbodiimide
LED	Light Emitting Diode
FPSI	Focal Plane Shift Imaging
Ce	Cerium
Yb	Ytteribium

Gd	Gadolinium
Ho	Holium
Cu	Copper
Si	Silicon
REO	Rare Earth Oxide
REE	Rare Earth Element
HPB	Hydrophobic
SHPB	Superhydrophobic
IPA	Isopropyl Alcohol
UHV	Ultra High Vacuum
VOC	Volatile Organic Compounds
NIO	Nickel Inverse Opal
DI	Deionized
L_{h}	Characteristic Length (μm)
LPD	Liquid Phase Deposition

GaN	Galium Nitride
Bo	Bond Number
We	Weber Number
Ca	Capillary Number
g	Gravitational Acceleration ($\mathrm{m/s^2}$)
μ_v	Dynamic Viscosity (Pa·s)
ρ	Density ($\mathrm{kg/m^3}$)
γ	Liqud-Vapor Surface Tension (mN/m)
$\dot{m}$	Condensation rate
m	Mass (μg)
γ_o	Interfacial Tension of Oil in Air (mN/m)
γ_l	Interfacial Tension of Liquid in Air (mN/m)
γ_ol	Interfacial Tension of Oil in Liquid (mN/m)
t	Inverse Opal Thickness (s)
ΔP	Pressure Drop (Pa)

LIST OF FIGURES

LIST OF TABLES

CHAPTER 1: INTRODUCTION

1.1. Overview

Throughout the history of humanity, humans have engineered tools and adapted to the environment in the pursuit of life, libery, and happiness. Sometimes, creativity and intellectual ability, two principle ingredients for every invention are not enough. We, as an engineers, and our ancestors have routinely found inspiration from nature in the pursuit of solving everyday problems. In fact, all our knowledge and all ingredients for engineered systems are based on mother naturegu, as we hymans are undoubtedly natural beings. Henceforth, as the opening remarks of my doctoral dissertation discussing nature-inspired engineering, I would like to provide my own definition. I classify all engineered materials, devices and technologies having a different extent of being either actively or passively nature-inspired. However, our knowledge was built on the understanding of nature. From a very broad perspective, we cannot entirely exclude the lessons leared from nature in our engineering product.

Herein, I will focus on natural and engineered surfaces to enhance phase change heat transfer, specifically focusing on vapor-to-liquid condensation phenomena. For over one hundred years, researchers have attempted to develop coatings, surfaces, and engineered systems to increase the heat transfer efficiency for different phase change processes, namely, condensation, boiling, and freezing. In the last several decades, the advent of nanoscience and nanotechnology have led us to a new horizon by modifying surface chemistry and structures at smaller length scales and higher precisions. Within this dissertation, I seek to answer why and how natural surfaces and materials benefit from wettability patterns, especially surfaces that repel water or have hydrophobicity and

how we as humans can utilize these phenomena to enhance phase change heat transfer for state-of-the-art engineering applications.

1.2. Background

Phase change heat transfer is a ubiquitous natural phenomenon found in meteoric events[1] as well as engineering systems[2-3] such as thermal cycles. Due to the existence of latent heat, which is the energy required for a material to change its phase, phase change heat transfer processes are very efficient at transferring large amounts of heat. Among all phase change materials, due to its abundance, necessity for life, and high latent heat, phase changes of water is universal. Boiling and condensation of water can be found in a plethora of engineering applications related to the energy-water nexus such as power generation[2, 4-8], water harvesting, water purification and desalination[9-14], and heating, ventilation and air conditioning (HVAC) systems[15]. Thus, enhancing boiling and condensation heat transfer will allow us to decrease energy consumption and increase the overall energy efficiency[16]. Over the past several decades, researchers have made numerous progress in increasing the effectiveness of boiling[17-20] and condensation[6, 19-21] heat transfer.

When water vapor condenses on a surface, the condensate droplets on the surface behave distinctively in accordance with the wettability of the surface. On a hydrophilic surface, droplets are devoid as a continuous liquid film forms on the wetting surface. This regime of condensation is called filmwise condensation (FWC) as the liquid condensate film grows up to a thickness of ~100 μm as it continuously drains downward from the surface in the presence of gravity. Conversly, on a hydrophobic surface, the liquid condensate forms distinct droplets since they cannot fully wet the surface. This regime of condensation is termed dropwise condensation (DWC).

Under FWC conditions, the liquid film remaining on the surface significantly decrease the heat transfer between the condensing vapr and surface by limiting the direct access of vapor to the surface and due to the relatively low thermal conductivity of the water film (≈0.6 W/(m·K)).[22] Therefore, the resulting condensation heat transfer coefficient is on order of 1-10 kW/(m^2·K). Unlike FWC condition, during DWC, condensate droplets sporadically shed from the surface due to gravity or vapor shear, leading to the continuous creation of fresh nucleation sites on the surface[23]. The continuous condensate removal[24-33] results in a condensation heat transfer coefficient approaching 50-100 kW/(m^2·K), 5 to 10 times higher compared to FWC condition[24]. Most recently, researchers have studied jumping droplet condensation on superhydrophobic surfaces which are capable of further enhancing heat transfer by ~200% compared to the DWC.[24] However, current state-of-the-art materials and methods available to achieve hydrophobic surfaces are not durable enough (~weeks) compared to the operational cycle or lifetime of relevant heat transfer systems (~years).[34] Thicker promoter coatings have higher durability but deteriorate heat transfer performance due to the added parasidic thermal resistance of the polymer-based, low thermal conductivity coating.[35]

Recently, researchers have discovered interesting examples of surfaces in nature exhibiting superhydrophobicity[36-37] or other multi-functionalities such as self-cleaning[38-40], anti-fogging[38, 41-43], anti-biofouling[44-45], and anti-microbial behavior[46-48]. These natural surfaces range from insect wings[49-52] and eyes[53-54], to gecko feet, to plant leaves[55-56] showing ability to tune their biochemical substances on the surface as well as their micro-and nanostructures.[37, 57-58] Along with the advances in nanofabrication technologies, recent works have attempted to replicate the desirable nanostructured surfaces inspired by nature.[54, 59-61] In this dissertation, from the perspective of heat

transfer, I study how natural surfaces can be applied to engineering applications to understand and enhance phase change heat transfer.

1.3. Outline of the Dissertation

The dissertation consists of a series of chapters including the results of several separate studies conducted to understand the wettability of natural and engineered surfaces, to design and develop engineered surfaces for the purpose of enhancing condensation heat transfer, and to adopt the understanding gained to other engineering applications. Chapter 2 presents an interdisciplinary study focused on comprehending why and how natural surfaces (insect wings) exhibit hydrophobicity and wether their non-wetting attributes are related to their adaptation to biological surroundings. Inspired on the findings of Chapter 2, Chapter 3 details a study to develop environment-friendly and sustainable superhydrophobic coating methods using extracts from natural substances such as tropical fruits and plants. Chapter 4 presents a study of the intrinsic wettability of inorganic materials by exploring the wettability transition of rare earth oxides from hydrophilic to hydrophobic due to hydrocarbon adsorption on the surface from its natural surroundings. Chapter 5 develops the concept of thin film condensation on nanoconfined surfaces using biphilic inverse opal structures that can achieve high heat transfer coefficients comparable to those observed in dropwise condensation. Chapter 6 demonstrates active hot spot cooling for enhanced thermal management of the electronics. Chapter 7 summarizes the key contributions of this dissertation and suggests future work.

CHAPTER 2: EXPLORING THE ROLE OF HABITAT ON THE WETTABILITY OF CICADA WINGS*

2.1. Introduction

Insect wings have been shown to possess nanostructures that affect wettability, and induce a plethora of functionalities such as droplet jumping[51-52], self-cleaning[52, 62], anti-fogging[38], anti-microbial activity[49-50] and anti-reflectivity[51, 63-64]. The nanostructured wings of an Australian species of cicada, *Psaltoda claripennis*, were shown to be superhydrophobic[65] and under the right conditions, self-propelled jumping condensate could be observed[52]. Similar nanoscale surface structures were found on the wings of other cicada species[51, 65-67], various species of dragonflies[62, 68], damselflies[62], butterflies[69] and other insects[66, 70]. There is great interest in these types of natural surfaces since detailed information on wing surface topography and resulting wettability characteristics has the potential to act as a rational design tool for the development of novel engineered materials. In addition, data on topography and wettability may provide insights into whether insect species distribution and life histories are constrained by structural and chemical features present on the exoskeleton, or whether the insect habitat provides the evolutionary pressure to dictate the wing nanoarchitecture[10, 71-72].

Artificial non-wetting surface structures, or superhydrophobic surfaces, have many technological applications. For instance, dropwise condensation has been shown to enhance heat transfer by ten-fold when compared to filmwise condensation on wetting substrates[73-74], enable self-cleaning[52, 56,

* This chapter was reprinted (adapted) with permission from *ACS Appl. Mater. Interfaces*, **2017**, *9* (32), pp 27173–27184. Copyright © 2017 American Chemical Society. Junho Oh is the first author of the publication. He contributed to the study via conducting experiments, analyzing data and writing the manuscript. Dr. Donald M. Cropek, Dr. Marianne Alleyne and Dr. Nenad Miljkovic guided the research and revised the manuscript as co-corresponding authors.

[75-76], and has led to the development of a litany of devices with previously unattainable efficiencies or functionalities such as thermal diodes[77], vapor chambers[78], atmospheric electrostatic energy generators[79] and active hot spot thermal management[80]. Under certain conditions, self-propelled jumping droplet condensate has been shown to form on superhydrophobic surfaces, driven by the surface-to-kinetic energy transfer occuringduring the coalescence of two or more droplets[28, 81]. The need for better understanding of the '*ideal*' or '*most efficient*' surface structure design has led many researchers to utilize biomimicry to artificially copy the surface topology designs observed on the aforementioned insects[38, 52, 57, 61]. But a single insect species, the *Psaltoda claripennis* cicada (Hemiptera: Cicadidae), has dominated studies on superhydrophobic wings[49-52]. Furthermore, prior works have not examined the spatial dependence of wing wettability, nor has an attempt been made to establish the crucial link between cicada wing functionality and its natural habitat.

The objective of the present study is to investigate the relation between the wing functionalities of multiple cicada species, such as wing wettability, topology, and droplet jumping behavior and the associated lifecycle, habitat and species relatedness. In this work, we focused on comparing cicada wings of four different species including homogeneity over different cells of the same wing. Specifically, we examined: *Neotibicen pruinosus* (Say 1825)[82], *Neotibicen tibicen* (Linnaeus 1758)[83], *Megatibicen dorsatus* (Say 1825)[82] and *Magicicada septendecim* (Linnaeus 1758)[83]. The first three of these species are relatively closely related and have similar life histories, emerging annually over several months during the summer. These species occur in very different habitats, including swampy bottomland forest, urban areas, and prairies. The fourth species (*Ma. septendecim*), a periodical cicada, was chosen due to it being distantly related and having quite a different life history from the other three species, emerging in large numbers every 13 or 17 years in a region. Using spatially resolved micro-goniometry, scanning electron microscopy, atomic

force microscopy, and optical microscopy, we show that within cicada species, the wettability of wings is spatially homogeneous across wing cells, irrespective of their distal versus proximal location relative to the body, or anterior versus posterior location on the wing. All four species were shown to have truncated conical pillars, with differing length scales ranging from 50 nm to 400 nm in height. Three species wings were found to be superhydrophobic with high advancing contact angle (> 150°) and low contact angle hysteresis (< 5°), resulting in stable droplet jumping behavior. The fourth, non-related species (*Ma. septendecim*), however, showed only hydrophobic behavior and gravitational shedding. Correlation between habitat characteristics and wing wettability yielded little connection. The results point to species relatedness and reproductive strategy as a more important factor for predicting wettability and surface structure, as opposed to habitat. This work not only elucidates the differences between inter- and intra-species cicada wing topology, wettability, and water shedding behavior, but allows predictions as to which other insects may have evolved superhydrophobic strategies to enhance survivability.

2.2. Methods

2.2.1. Insect Collection

At least 18 species of cicadas can be found in Illinois[84]. These species occur on trees and forbs in varied habitats such as prairies, swamps, forests and urban parks. Most species are annual cicadas which live in the soil for multiple years and emerge as adults in the summer with an estimated 30 day adult life span. We focused on four different cicada species from four different habitats (Fig. 2-1). *Neotibicen pruinosus* is a central United States species that can be found on a number of deciduous trees[85] including those in urban parks throughout the state. *N. pruinosus* likely has the largest range throughout Illinois of all cicada species, including those in this study. Hardwood

forests serve as *Neotibicen tibicen* habitats. In Illinois, *N. tibicen* is commonly found in the floodplains, including in cypress swamps in the lower Cache river region of Southern Illinois. *Megatibicen dorsatus* is a species that is found on forbs in mesic prairies in central Illinois. *Me. dorsatus* appears to be more sensitive to anthropogenic disturbance as it can typically only be found in remnant prairies, has stricter host-plant requirements, and is adapted to the fire regime that is vital for the maintenance of tallgrass prairies. Although they occur in such diverse habitats, *N. pruinosus, N. tibicen* and *Me. dorsatus* are all annual cicadas. Periodical cicadas also occur in Illinois, including *Magicicada septendecim*. The immatures of periodical cicada species spend 13 or 17 years in the soil and emerge in large numbers during the spring and early summer, at which time they eclose to adults. During the period of our study, there were no known emerging broods of *Ma. septendecim* in Illinois but we were able to collect individuals of this species from Brood V in Ohio during the spring of 2016.

Adult cicadas were caught by net or hand and, when possible, collected soon after emergence from the ground after which individuals were brought indoors to complete their molt. This latter method was preferred over net capture to ensure wings were not exposed to harsh conditions or excessively dirty prior to analysis.

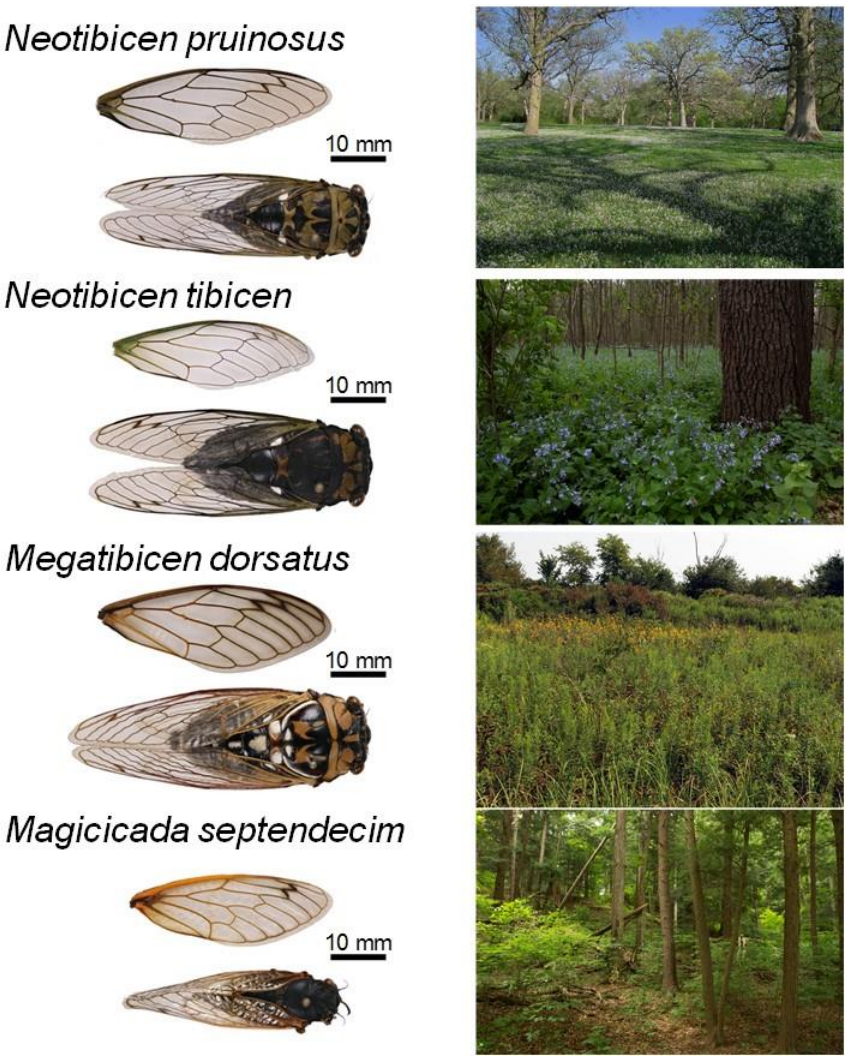

Figure 2-1 Photographs of the top view and detached forewings of the four cicada species (left column), and the habitats from which they were collected, including urban park, bottomland forest, mesic prairie, and mixed-mesophytic hardwood forest for *N. pruinosus*, *N. tibicen*, *Me. dorsatus*, and *Ma. septendecim*, respectively.

N. pruinosus was collected in central Illinois at Carle Park, Urbana, IL (40°06'14"N, 88°12'44"W) and Crystal Lake Park, Urbana, IL (40°07'35"N, 88°12'34"W) as they were emerging from the ground. *N. tibicen* was collected when possible during emergence from the ground, but also by net

and from lights in the evening. *N. tibicen* specimens were collected in southern Illinois at the towns of Metropolis (37°08'36"N, 88°43'36"W), Belknap (37°20'06"N, 88°56'19"W), and Cypress (37°18'42"N, 89°01'04"W). *Me. dorsatus* was collected from railroad right-of-way prairies along US45 between Urbana and Buckley, IL (40°34'56"N, 88°02'41"W). At these sites, it was not possible to easily find emerging final instars due to the vegetation, so *Me. dorsatus* individuals were always collected by net as adults. Multiple broods of the 17-year periodical cicada *Ma. septendecim* occur in Illinois but during our study (Spring-Summer 2016) none of these broods emerged in the state. Instead, we collected individuals from Brood V in Brecksville, OH (41°18'48"N, 81°37'24"W).

2.2.2. Wing Preparation

Adult cicadas were briefly chilled prior to removal of wings with forceps. After wings were removed, the body of the cicada was frozen for later species identification. The dorsal side of the large transparent forewings were the focus of this study. The wing cells were chosen by alternating neighboring cells to obtain a spatial representation of the entire wing, *i.e.*, cells close to the proximal, distal, posterior, and anterior ends, in addition to one cell located near the center of the wing (Fig. 2-2). Focusing on specific cells enabled us to make comparisons among the same cells both inter- and intraspecifically. Wing cells were cut out using a sterilized scalpel. For scanning electron microscopy (SEM) and condensation observational studies, the dissected cell samples were attached to a 1 x 1 cm polished copper substrate (Multipurpose 110 Copper, 1/32” thickness, McMaster-Carr) using silver paint (PELCO conductive silver paint, Ted Pella Inc.). For atomic force microscopy (AFM), a wing cell sample was attached to a magnetic AFM chip with generic gel-type super glue for stronger fixation.

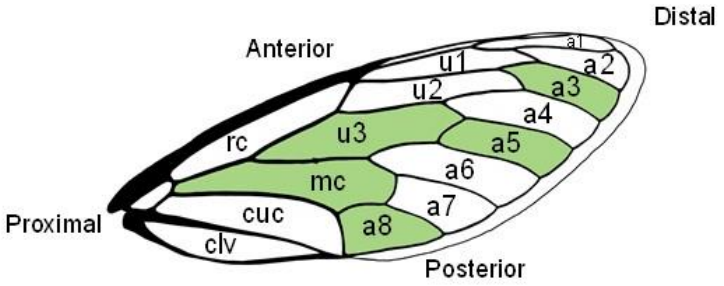

Figure 2-2 Generalized forewing map based on *Magicicada septendecim* with major wing cells labelled according to Moulds[86]. (a1-a8) apical cells; (clv) clavus; (cuc) cubital cell; (mc) medial cell; (rc) radial cell; (u1-u3) ulnar cells. Shaded cells indicate the cells included in this study.

2.2.3. Atomic Force Microscopy (AFM)

Topological characteristics of the cicada wings were investigated using an Asylum Research MFP-3D atomic force microscope in tapping mode. Since the wing membrane was very soft, flexible and thin, it was essential to fix the membrane to a stiff substrate to obtain the best AFM results. As mentioned in Section 2.2.2, we used a magnetic AFM chip and gel-type strong glue (Loctite Gel Super Glue) to fix it properly. Because of the high aspect ratio (up to 5) and small spacing (~100 nm) between nanopillars, tilt-compensated high aspect ratio AFM tips were used (NanoWorld, NW-AR5T-NCHR). The AFM scan area was 2 μm by 2 μm with a 0.5 Hz scan frequency. The average force constant was 42 N/m with an average 330 kHz resonance frequency. The drive amplitude was approximately 120 mV. Each AFM scan profile was flattened to be leveled at the base. We used an open-source software, Gwyddion, to process, analyze and visualize the AFM scan data[87]. The AFM height profile was flattened to eliminate the effect of wing base curvature.

2.2.4. Scanning Electron Microscopy (SEM)

Low and high resolution field emission scanning electron microscopy (FESEM) images of each cicada species wing were obtained using an FEI Quanta 450 ESEM in high vacuum operation mode. The accelerating voltage was set to 5 kV and emission current was approximately 30 pA, with a spot size of 2 nm, to prevent charging and sample damage by the electron beam. Prior to FESEM, the wing samples were sputter coated with a 5 nm thick layer of Au-Pd. Nanopillar shape and overall surface topology were characterized by positioning the sample perpendicular to the electron beam (top view) or at a 45° inclined orientation (side view). The side view was utilized to estimate the size of nanostructures and surface roughness to validate the AFM data.

2.2.5. Wing Thickness Measurements

The wing membrane thickness was measured using the Focal Plane Shift Imaging (FPSI) method[88]. We first placed sub 25μm-sized PMMA particles (Cospheric Clear Poly(methyl methacrylate) Microspheres, PMPMS-1.2) on both sides of the whole wings. Using an optical microscope (Eclipse LV100, Nikon) and high-resolution camera (Nikon DS-Qi2), we measured the z-location when the focal plane was at the mid-point of the particles (maximum radius) on either side of the wing surface. The wing membrane thickness was calculated by subtracting the particle radii from the total z- coordinate travel distance during focal plane shifting. Note that particles had to be used for observation due to the strongly anti-reflecting nature of the wing nanostructures, making it extremely difficult to measure the wing-air interface location on top and bottom of the wing.

2.2.6. Water Droplet Advancing and Receding Contact Angles

Contact angle measurements of ≈100 nL water droplets on all samples were performed using a microgoniometer (MCA-3, Kyowa Interface Science). The advancing and receding contact angles were measured at multiple spots on each wing cell sample. Within each cell (u3, mc, a3, a5, and a8 from Fig. 2), five measurements were taken at distinct locations and the results averaged. To grow droplets, the piezoelectric dispenser was placed above each surface with a spacing ranging from 5 to 10 mm, and turned on to dispense monodisperse microscale droplets. The surface-dispenser spacing was chosen to have close control of the dispensed droplet trajectory, which is not possible at larger spacings due to the presence of random air currents which act to deflect microscale droplets. Droplets were injected at a rate of 60-80 droplets/sec. Due to the relatively

small size of departing droplets (~5 μm), the shape of droplets remained spherical during flight. This assumption is justified given that the Bond, Webber, and Capillary numbers are all much less than one. As the microscale droplets landed on the surface, they began to accumulate and grow to form a single larger droplet. The camera focal plane was located at the growing droplet mid-plane for the desired optical zoom level. Simultaneously, while the droplet was growing, contact angle measurements on the surface were performed. All contact angle data were analyzed using the image processing software (FAMAS, interFAce Measurement & Analysis System) with the circle fitting method.

2.2.7. Jumping Droplet Condensation Characterization

Jumping droplet condensation experiments were performed using a customized top-view optical light microscopy setup[88]. A high speed camera (Phantom, V711, Vision Research) was attached to the upright microscope (Eclipse LV100, Nikon) for top view analysis, performing video recordings at variable frame rates up to 500,000 frames per second. Samples were horizontally mounted to a cold stage (TP104SC-mK2000A, Instec) and cooled to the test temperature of T_w = 2-5 ± 0.5°C, in a laboratory environment having air temperature, T_{air} = 23 ± 0.5°C, and relative humidity, ∅ = 30 - 50 ± 1% (Roscid Technologies, RO120). Once the temperature was set and stabilized, the LED light was turned on and imaging performed. LED lighting did not show any effect on the sample wettability over time. Illumination was supplied by an LED light source (SOLA SM II Light Engine, Lumencor). The LED light source was specifically chosen for its high-intensity, low power consumption (2.5W) and narrow spectral range (380-680 nm) to minimize heat generation at the surface due to light absorption. Furthermore, by manually reducing the condenser aperture diaphragm opening size and increasing the camera exposure time, we were

able to minimize the amount of light energy needed for illumination and hence attenuate local heating effects during condensation experiments. Imaging was performed with a 20X (TU Plan Fluor EPI, Nikon), 50X (TU Plan Fluor EPI, Nikon), or 100X (TU Plan Fluor EPI, Nikon) objective. All experiments were conducted at supersaturations, S = 1.02 ± 0.035, below the critical supersaturation, $S_c \approx 1.12$, associated with surface flooding conditions for superhydrophobic surfaces ($S = P_v/P_{sat}(T_w) < S_c$, where P_v and $P_{sat}(T_w)$ represent the vapor pressure of the laboratory air and saturation pressure at the sample temperature (T_w), respectively). This was done in order to remain in the droplet jumping regime to study the coalescence and departure dynamics. Prior to observation, the LED light source was turned off until condensation initiated.

2.3. Results and Discussion

2.3.1. Cicada Wing Topography

The topography of the surface of the five identified wing cells (Fig. 2-2) for all four cicada species (Fig. 2-1) was analyzed using AFM and SEM. The 3D images of the wing surface structures showed the existence of uniformly distributed nanopillars (Fig. 2-3). The shape profiles of the nanopillars from different wing cells of the same cicada species were approximately uniform in height, diameter, and center-to-center spacing or pitch (Fig. 2-4). The nanopillars present on *N. pruinosus* and *N. tibicen* are similar (Fig. 2-3a&b), and tallest (350-400 nm) among the species studied (Fig. 2-4). *Me. dorsatus* nanostructures are similar in shape to *N. pruinosus* and *N. tibicen* (Fig. 2-3c) but shorter in height (≈ 250 nm, Fig. 2-4). Of the four species studied, *Ma. septendecim* had the shortest nanopillars (≈ 50 nm, Fig. 2-4). Due to the finite size of the AFM tip, exact dimensional scans for the pillar height was difficult to obtain. Hence, high angle (45°) SEM imaging was also utilized to obtain pillar heights.

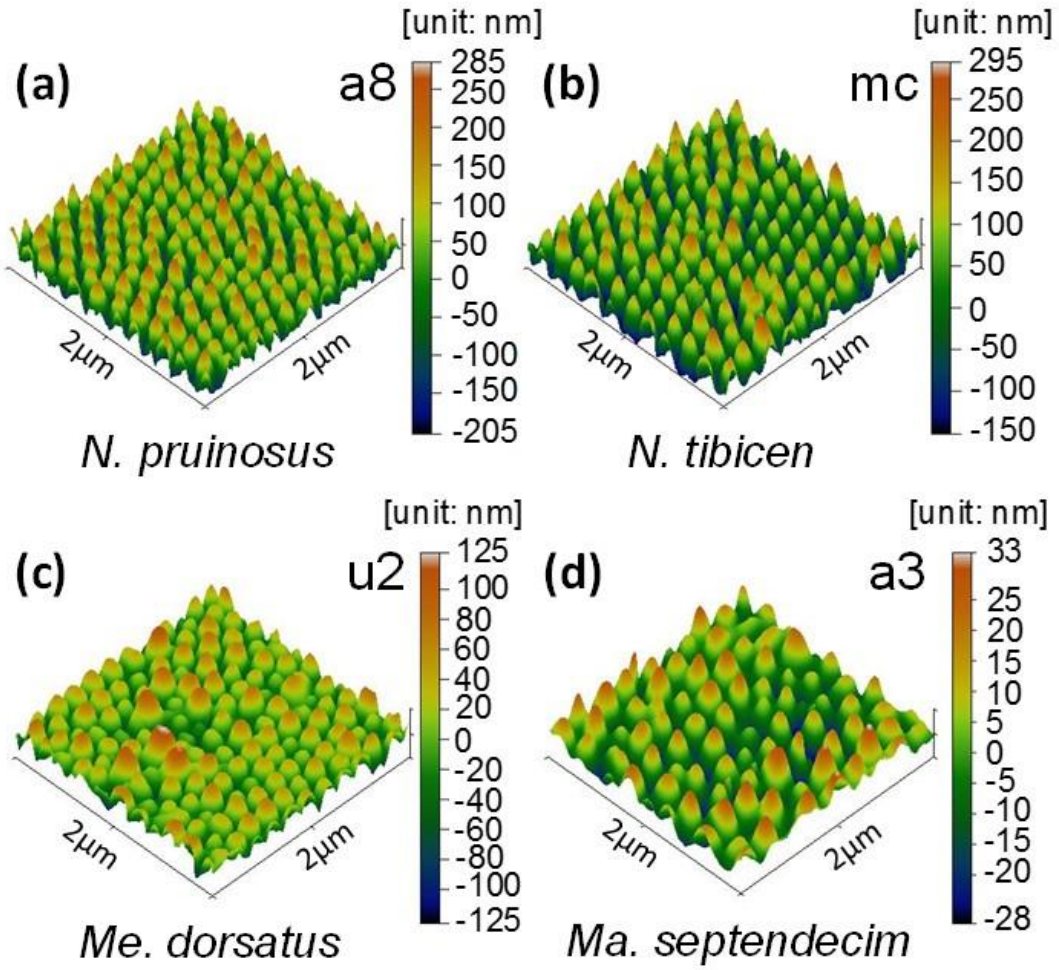

Figure 2-3 Atomic force microscopy (AFM) scans of the wings of (a) *N. pruinosus*, (b) *N. tibicen*, (c) *Me. dorsatus*, and (d) *Ma. septendecim*. Nanopillars for each wing species were found to be uniform and independent of cell location on the wing. The scale bar to the right of each figure indicate the z-coordinates. The color scale bars represent the measured minimum and maximum of the entire scanned area, which includes effects of macroscale roughness, and pillar non-uniformity, therefore, the height data is only an approximate representation. Note, due to the finite size of the AFM probe tip (≈10 nm), the z-coordinates represent a lower bound on the nanopillar height due to the inability of the probe tip to reach the wing base between the nanopillars. (For a comparison of all wing cell AFM data, please see Appendix A, Section A.2)

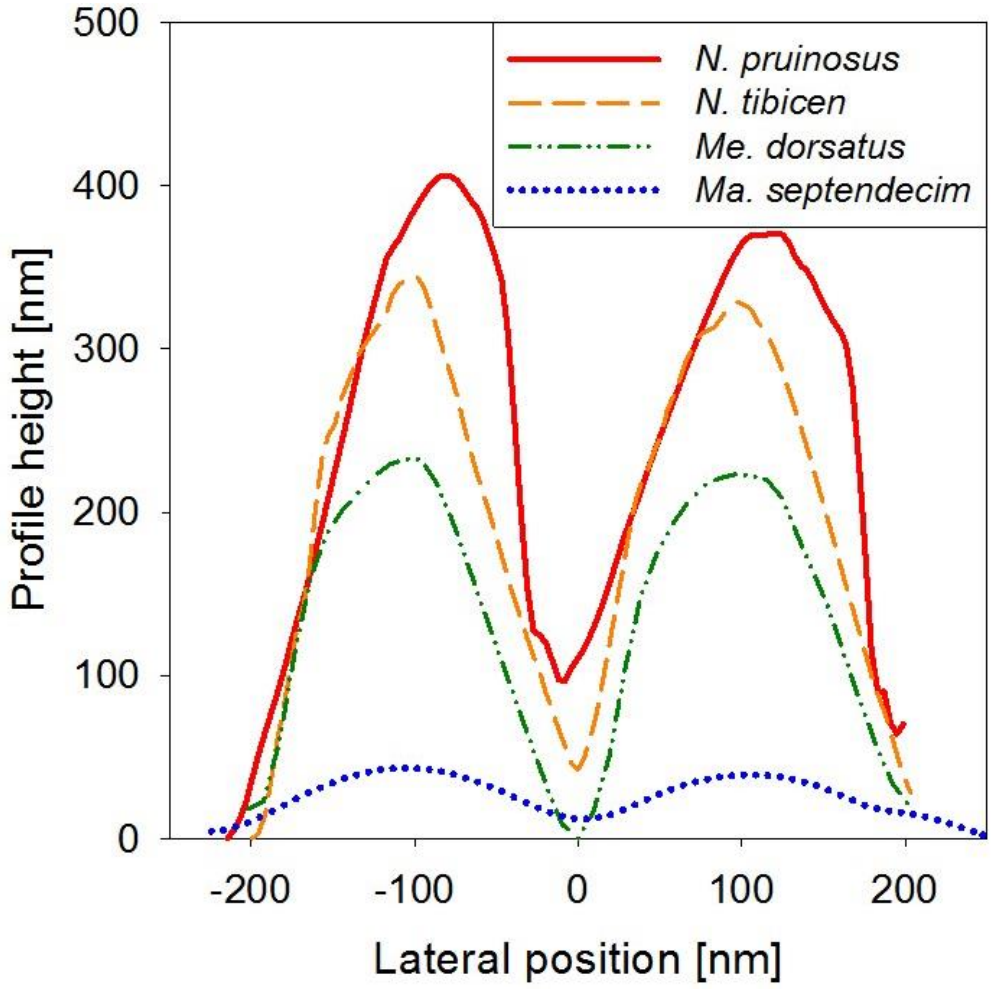

Figure 2-4 Comparison of the averaged AFM line scan height profiles of two adjacent nanopillars of *N. pruinosus*, *N. tibicen*, *Me. dorsatus*, and *Ma. septendecim*. The standard deviations of the *N. pruinosus*, *N. tibicen*, *Me. dorsatus*, and *Ma. septendecim* nanopillar heights calibrated from the 3D scans shown in Figure 2-3 were 29.6 nm, 18.2 nm, 10.2 nm, and 6.5 nm, respectively. Note, profiles were re-zeroed based on the lowest z-coordinate while calculating profile heights.

For all four cicada species, the arrangements of the nanopillars on the wing surface were found to have a regular hexagonal lattice with a ≈200 nm pitch (Fig. 2-5 insets). To quantify the nanostructure topology and compare the results to AFM scans, all SEM images were processed using MATLAB and ImageJ software via circle fitting[89]. The AFM scan resolution was approximately 8 nm, equivalent to the AFM tip radius which acts as a lower lateral resolution limit. However, the AFM scans provide a much higher resolution (≈ 0.1 nm) with respect to the z-coordinate (pillar height) compared to the lateral profile[90]. In contrast, SEM imaging is preferred for gathering higher resolution data in the lateral directions. Combining both AFM and SEM data analyses allowed us to better understand the topological features such as pitch (P), height (H), diameter (D) and opening angle (α) of the nanostructures present on cicada wings (Table 2-1) (for a detailed schematic with all geometric dimensions labeled, see Figure A-1 of Appendix A).

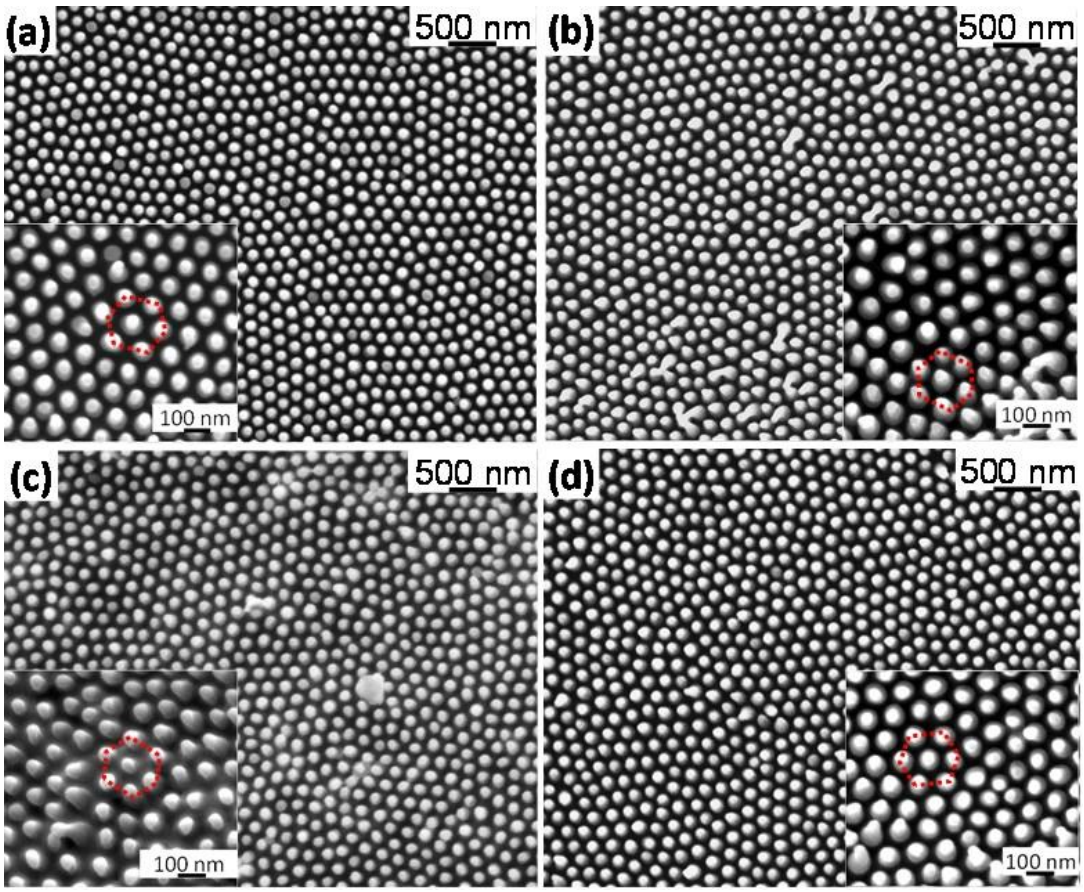

Figure 2-5 Top-view scanning electron microscopy (SEM) image of the mc cell for (a) *N. pruinosus*, (b) *N. tibicen*, (c) *Me. dorsatus*, and (d) *Ma. septendecim*. Each inset image represents a high resolution SEM of the pillars and outlines the hexagonal pattern of the nanopillar locations (dotted red hexagons). The hexagons for all four species were found to be similar in size.

To determine the nanopillar solid fraction (φ) defined as the fraction of solid area exposed on pillar tops normalized by the projected surface area, and the roughness (r) defined as the total pillar surface area normalized by the projected surface area, we used the following equations:

$$\varphi = \frac{\pi D^2}{4(D + (P - 2(H \tan \alpha))^2} \quad \text{(Eq. 2-1)}$$

$$r = \frac{(D + (P - 2(H \tan \alpha))^2 + \pi DH}{(D + (P - 2(H \tan \alpha))^2} \quad \text{(Eq. 2-2)}$$

Interestingly, the results of Table 2-1 reveal a self-similar topology of the cicada wing nanostructures, with approximately equal solid fraction and hexagonal structure that is independent of species. This is in good agreement with the previously observed structures on other cicada species[49, 65-67, 70, 91-92]. Note, the calculated solid fraction from Eq. 2-1 represents an upper bound due to the unknown nature of water droplet contact with the pillar protuberances that are spherically capped and have a radius of curvature at the apex in the range of 25–45 nm.

Table 2-1 Topological data of the cicada species studied. Values in parenthesis represent standard deviation. Values in curved brackets represent the calculated height from SEM imaging. Roughness, solid fraction, and opening angle were calculated from the SEM data.

	Diameter D [nm]	Pitch P [nm]	Height H [nm]	Roughness r	Solid fraction φ	Opening Angle α
N. pruinosus	197.2 (7.82)	217.6 (33.4)	405 {405}	6.29	0.65	13.7°
N. tibicen	210.8 (13.38)	224.4 (35.2)	345 {462}	7.07	0.69	12.9°
Me. dorsatus	195.8 (8.22)	226.7 (31.5)	250 {183}	3.19	0.59	28.1°
Ma. septendecim	210.2 (11.04)	227.1 (30.2)	50 {111}	2.42	0.67	43.4°

2.3.2. Wing Thickness

In addition to examining the inter-species and intra-species topological structure on the wings, we also characterized the wing thickness for each species using the focal plane shift imaging technique[88]. Table 2-2 shows the wing membrane thickness for the cells of interest (Fig. 2-2) for all four cicada species. Although the variation is not significant, the wing membrane thickness tends to be thinner at the distal and posterior parts of the wing (a3, a5, a8). We believe the thinner cells arise due to the proximity of the thicker wing vein near the proximal part of the wing which gives the wing curvature. The intra-species wing thickness variation was negligible. Furthermore, no clear relationship seems to exist between wing thickness and habitat wetness.

Table 2-2 Wing thickness of the cicada species corresponding to the cells of interests (Fig. 2-2). [units: μm] The values in parentheses refer to the standard error.

Species \ Cell	u3	mc	a3	a5	a8
N. pruinosus	6.8 (0.21)	7.6 (0.32)	6.3 (0.27)	6.5 (0.35)	6.2 (0.36)
N. tibicen	5.5 (0.45)	6.1 (0.64)	4.2 (0.32)	4.4 (0.21)	4.7 (0.33)
Me. dorsatus	6.6 (0.52)	5.7 (0.38)	7.1 (0.53)	6.8 (0.37)	5.8 (0.36)
Ma. septendecim	8.5 (0.36)	7.7 (0.58)	7.4 (0.94)	6.6 (0.35)	7.7 (0.59)

2.3.3. Wing Edge Structure

To characterize the microstructures on a wing edge and to see whether nanostructures were present, we examined the edges of all four cicada species using optical microscopy. Unlike the nanopillars observed in the wing cells, the wing edges have spikes and directional scale microstructures (Fig. 2-6). The spike-shaped microstructures on the wing membrane and scale-shaped structures on the wing vein were asymmetric, leading toward the distal end of the wing. We hypothesize that the directional structures allow condensed and deposited water droplets to more easily flow or roll-off toward the distal end of the wing and act to pin any motion toward the proximal end, as previously observed on superhydrophobic wings of certain butterfly species[93]. All cicada species examined had similar microstructures, irrespective of their habitat or phylogenetic closeness.

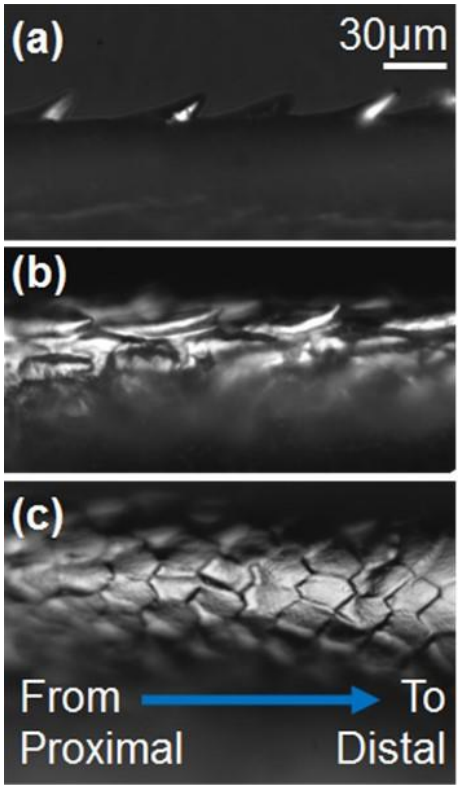

Figure 2-6 Microscale structures at the posterior edge (Fig. 2-2) of the cicada wing membrane (a) near the proximal end, (b) near the distal end, and (c) shark scale-like microstructures on the thick wing vein at the anterior edge of the wing. The images were obtained using optical microscopy at 50X on an *N. pruinosus* wing.

2.3.4. Cicada Wing Wettability

To better understand the function of the cicada structures, it is important to not only characterize the wing nanostructure topology, but also the resulting water contact angle behavior (wettability). Contact angle measurements show that *N. pruinosus, N. tibicen* and *Me. dorsatus* have superhydrophobic wings with droplets residing in the Cassie-Baxter state (apparent advancing contact angle > 150°), whereas the wings of *Ma. septendecim* are hydrophobic (advancing contact angle between 90 and 150°) with droplets residing in the Wenzel state as characterized by the large contact angle hysteresis (Fig. 2-7). The wings of *N. pruinosus* and *N. tibicen* showed higher superhydrophobicity than *Me. dorsatus*, which was only marginally superhydrophobic, but all had an exceptionally low contact angle hysteresis (< 10°). The low contact angle hysteresis of the three superhydrophobic cicada species suggest that the observed nanostructures on the wing surface are coated with a non-polar lipid, most likely a thin and conformal layer of a lipid which acts to reduce the surface energy and attain superhydrophobicity as observed analogously in different insect and plant species[61, 94-96]. Due to the non-re-entrant nature of the wing nanostructures[97], the superhydrophobic nature of cicada wings cannot be attributed to structural hydrophobicity alone[98]. Indeed, removal of the hydrophobic lipid layer would lead to superhydrophilicity on the wing surface. Figure 2-8 shows the measured water contact angle on the five different wing cells of interest (u3, mc, a3, a5, a8) for all four cicada species. For *N. pruinosus, N. tibicen* and *Me. dorsatus* wettability of wing membranes did not differ significantly (varying within 5°) between cells on the same wing. The results also indicate that the superhydrophobic wings of the three cicada species studied should have high droplet mobility[27]. However, *Ma. septendecim* showed comparably larger variation between the cells (within 10°) on the same wing and greater contact angle hysteresis, indicating larger water-droplet adhesion.

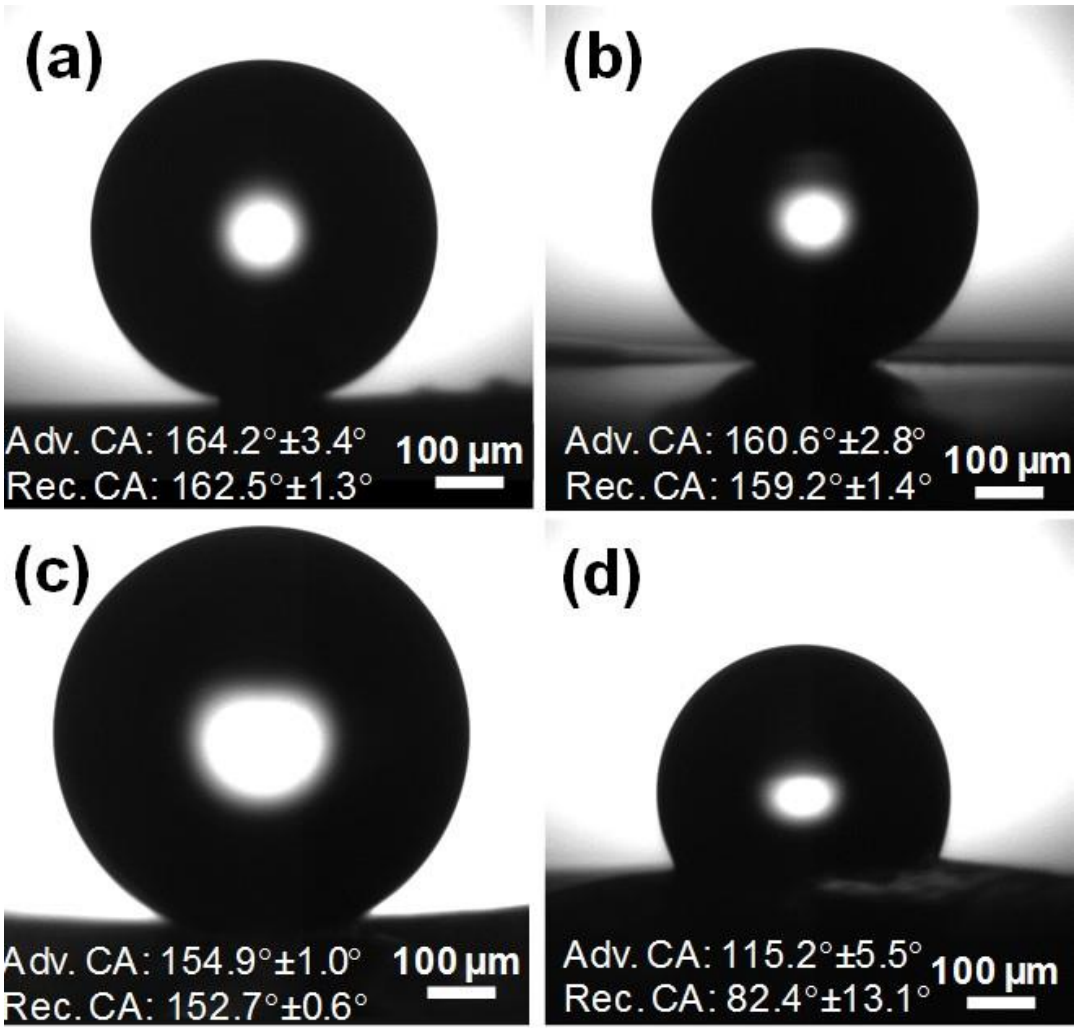

Figure 2-7 Water droplets residing in the receding state on the wing surface of (a) *N. pruinosus*, (b) *N. tibicen*, (c) *Me. dorsatus*, and (d) *Ma. septendecim*.

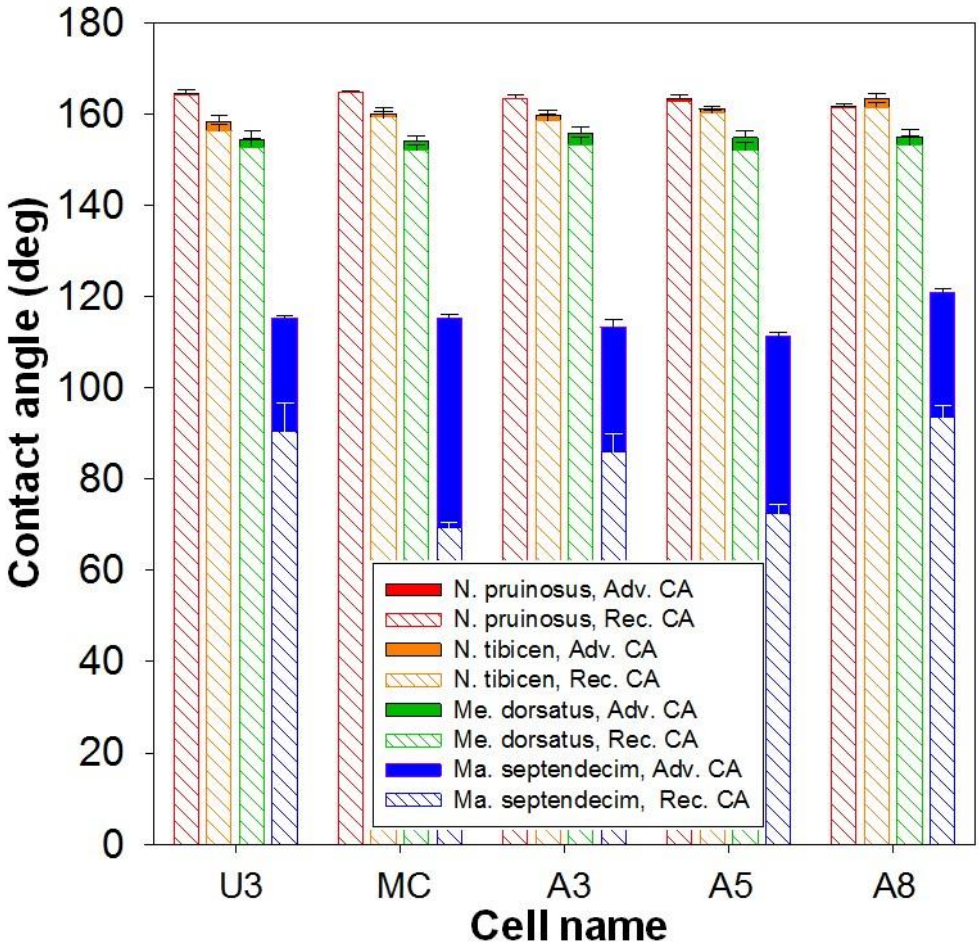

Figure 2-8 Advancing (total length of the bar) and receding (only cross-hatched portion of the bar) contact angles for all 4 cicada species (shown in different colors) and selected wing cells (horizontal axis. Fig. 2-2).

The similarity in the contact angle behavior between the differing species arises due to the self-similar topography (diameter and pitch) of the nanopillars (Table 2-1), as well as the almost identical upper bound on the solid fraction (φ). Although the pillar heights and corresponding roughness (r) of each species differs markedly, droplets residing in the Cassie-Baxter state have little dependence on pillar height for pillars having vertical side-walls. Indeed, a previous study showed that multiple superhydrophobic cicada species have poor correlation between pillar height and advancing contact angle[92]. The dominating factor affecting the contact angle, hysteresis, and adhesion, is the solid fraction, as also evidenced by the Cassie-Baxter equation:

$$\cos\theta_{\mathrm{CB}} = \varphi(\cos\theta_{\mathrm{a}} + 1) - 1 \qquad \text{(Eq. 2-3)}$$

where θ_{CB} is the apparent advancing contact angle in the Cassie-Baxter state on the nanopillar surface, and θ_{a} is the intrinsic advancing contact angle on a smooth surface. Equation 2-3 suggests that not only are the nanopillar solid fractions very similar (as shown in Table 2-1), but that the surface chemistry on the pillars, or the intrinsic wetting angle, is similar as well. Given the propensity of nature to utilize non-polar hydrogenated lipids to achieve hydrophobicity[61, 94-96], the latter can be assumed with confidence. It is interesting to note, if we use an intrinsic advancing contact angle of $\theta_{\mathrm{a}} \approx 105^{\circ}$[91, 99-100], appropriate for smooth surfaces functionalized with hydrogenated lipids, with the apparent advancing contact angles on the nanopillar surfaces (Figure 2-8), we estimate the effective solid fraction of the superhydrophobic surface to be $\varphi = (\cos\theta_{\mathrm{CB}} + 1)/(\cos\theta_{\mathrm{a}} + 1) \approx 0.05$, 0.09, and 0.14 for *N. pruinosus, N. tibicen* and *Me. dorsatus*, respectively. The low calculated solid fractions are more realistic representations of what occurs when a water droplet resides on the nanopillars and help explain the ultra-low contact angle hysteresis and adhesion observed on the wings. It is important to note, the discrepancy between the calculated solid fractions of Table 1 and Eq. 2-3 is mainly due to the lack of knowledge of the

wetting state on the pillars when using the SEM analysis (Table 2-1). The results of Table 2-1 assumed that the entire pillar tops (areas of high contrast with the base, Figure 2-5) were fully wetted. This may include partial imbibition of the droplet on the pillar as predicted from the calculated pillar radius. However, the results of Eq. 2-3 utilize the measured advancing contact angles in order to estimate the effective wetted area beneath each droplet, which is more accurate due to its use of experimental inputs.

Furthermore, although the pillar heights correlate somewhat with the measured apparent contact angles of the species studied here (Figure 8), the presence of variable opening angles for each species inexorably links the surface solid fraction directly to species pillar height, with taller pillars having lower solid fraction than shorter pillars. Furthermore, the presence of pillar protuberances that are spherically capped having radii of curvature at the apex in the range of 25–45 nm make it particularly difficult to predict the wetted area and true solid fraction beneath each droplet in the Cassie-Baxter state.

The emergence of the Wenzel wetting state on the wing of *Ma. septendecim* can be explained by the high opening angle, α of the nanostructures (Table 2-1, Fig. A-1 of Appendix A). To ensure stable non-wetting (Cassie-Baxter droplets), the local contact angle at the water-solid sidewall (θ_μ) must satisfy $\theta_\mu = \alpha + 90° < \theta_a$, while for the complete wetting situation, the Wenzel state[40], $\theta_\mu > \alpha + 90° > \theta_a$, must be satisfied. Assuming $\theta_a \approx 105°$, the Cassie-Baxter state droplets will be stable if $\alpha \leq 15°$. Indeed, the only cicada species which did not fulfill the Cassie-Baxter criterion by a significant margin was *Ma. septendecim*, with $\alpha = 43.4°$. It is important to note, although *Me. dorsatus* also failed to satisfy $\alpha \leq 15°$, the presence of a Wenzel droplet was not favorable due to two main factors. First, the opening angles determined in Table 2-1 did not use the AFM data for pillar height and spacing (Figure 2-4), rather they used the calculated SEM pillar height, which

underestimated the true pillar heights. Based on the opening angles determined using the AFM data, the opening angle of *Me. dorsatus* was 20°, above the criterion of $\alpha \leq 15°$, but closer to the critical value. The opening angles of *N. pruinosus*, *N. tibicen*, and *Ma. septendecim* based on AFM data (Figure 2-4) were: 9°, 17°, and 67°, respectively. Furthermore, the clear presence of a Cassie-Baxter state droplet on *Me. dorsatus* indicated that the assumption of a 105° intrinsic advancing contact angle represents a lower bound on the true intrinsic contact angle on the surface. Indeed, the actual intrinsic contact angle is more hydrophobic, in the range of 110 to 115° (resulting in $\alpha \approx 20$ to 25°).

The correlation between wing wetting behavior and aspects of cicada habitat was poor. The wings of cicadas living in drier habitats (e.g., *Me. dorsatus*) were observed to be just as superhydrophobic as those of species living in wet environments (e.g., *N. tibicen*). As in topology, the greater predictor of wetting behavior was the relatedness of the cicada species, with *Ma. septendecim* having the most distinct wetting and topological structure from the other three closely related species. The fact that species relatedness is a greater predictor of wetting behavior than habitat has important implications for biomimicry of related functions such as anti-microbial properties and self-cleaning ability. To put this observation to the test, we examined the jumping droplet behavior on the cicada wing, a phenomenon with close correlation to cicada self-cleaning ability[52] and anti-fogging properties[38].

2.3.5. Jumping Droplet Condensation

Droplet jumping is a process governed by the conversion of excess surface energy into kinetic energy when two or more droplets coalesce and involves a symmetry-breaking surface. For the simplest case of two, equally sized inviscid spherical droplets coalescing on a surface with no adhesion, an energy balance gives a characteristic jumping speed that follows an inertial capillary scaling. Coalescence-induced droplet jumping is an inherently inefficient process with only a small fraction of the available excess surface energy (< 6%) being converted to useful internal flow momentum to provide the jumping droplet with translational kinetic energy[28]. Droplet growth on the cicada wing surfaces was characterized using optical microscopy in ambient conditions. Condensed droplets with diameters as small as 2 μm demonstrated large apparent contact angles similar to the macroscopically measured value (Fig. 2-8). An estimate of the droplet radius-dependent advancing angle indicated that all measured droplet jumping events were in a constant contact angle growth mode[101]. Since the characteristic pillar spacing length scales (pitch ≈ 200 nm) were significantly smaller than the smallest droplet jumping diameter measured (≈ 5 μm), we were able to access a droplet growth regime well above the flooding limit[27].

Figure 9 shows top-view time-lapse images of condensation on the wing. Partially wetting droplets nucleated within a unit cell (area between pillars), and while growing beyond the confines of the unit cell, their apparent contact angle increased and they spread across the tops of the pillars in the shape of a balloon with a liquid bridge at the base of the pillars.[102-104] Before coalescence with neighboring droplets, an increasing proportion of the droplet contact area was in the Cassie-Baxter state as observed in the deposited droplets during microgoniometry. Upon coalescence, the droplet jumped away from the wing surfaces of all three superhydrophobic species, *N. pruinosus*, *N. tibicen* and *Me. dorsatus*. Droplet jumping was not observed on the *Ma. septendecim* cicada wing

due to the Wenzel wetting state, corresponding high contact angle hysteresis, and droplet-surface adhesion.

Internal viscous dissipation plays a limited role in the jumping process for the experimentally accessible low Oh number regime studied here ($Oh = \mu/(\rho R\gamma)^{1/2} < 0.1$, where μ, ρ, R, and γ are the liquid droplet dynamic viscosity, density, radius, and surface tension, and Oh is the ratio of viscous to inertial and surface tension forces). Instead, finite droplet-surface adhesion dominates the jumping process. Due to the ultra-low contact angle hysteresis (< 10°) and homogeneous topology and wetting of the *N. pruinosus, N. tibicen* and *Me. dorsatus* species (Fig. 2-8), we observed vigorous droplet jumping in all cells of interest. However, due to the lower advancing contact angle of *Me. dorsatus*, we observed less frequent jumping compared to *N. pruinosus* and *N. tibicen*, and usually involved larger droplets. Furthermore, the minimum droplet departure size on each surface was determined to be dependent on the advancing contact angle, and weakly dependent on cell location.

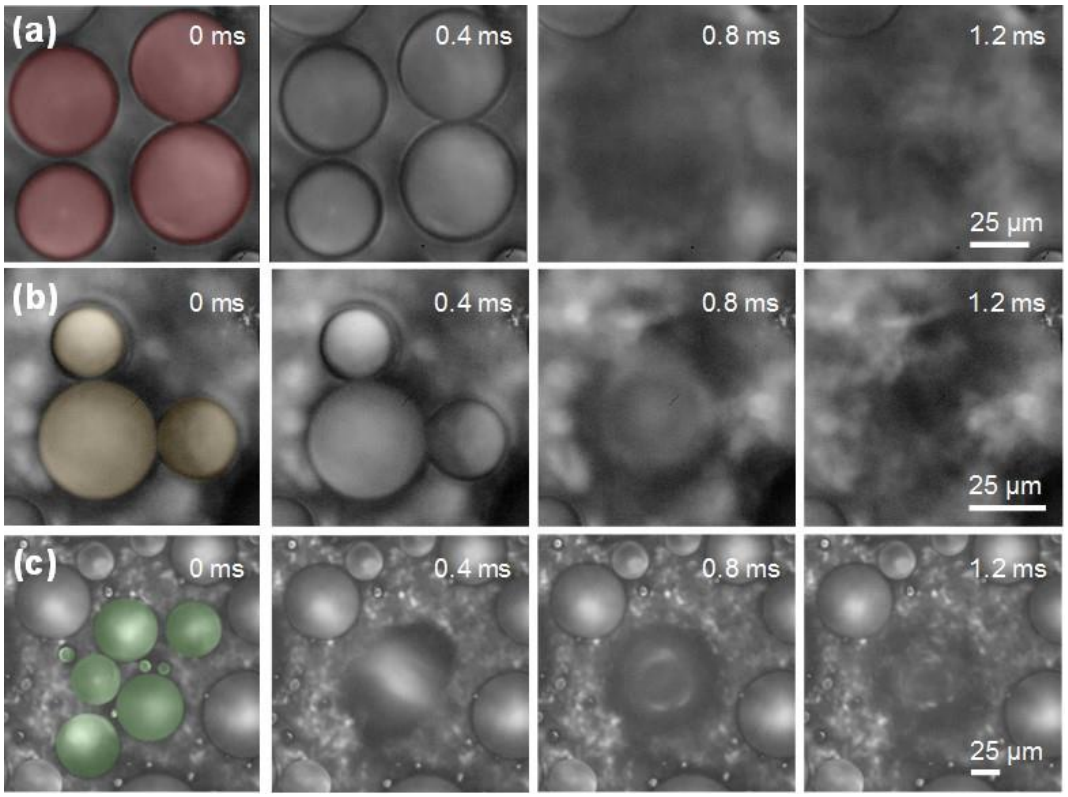

Figure 2-9 Time lapse images of droplet jumping on wing cells of (a) *N. pruinosus* (cell u3) (b) *N. tibicen* (cell mc), and (c) *Me. dorsatus* (cell mc). Wings were horizontally oriented. The false colored droplets at 0 ms jumped upon coalescence. The droplets of interest have jumped out of the frame of view after 1.2 ms.

For the *Me. dorsatus*, *N. tibicen*, and *N. pruinosus* species, the minimum observed droplet jumping sizes were: ≈7.1 ± 0.5, 4.5 ± 0.8, and 2.3 ± 0.9 μm, in accordance to previous experimental[27-28, 38] and theoretical[27] studies, which implicate droplet surface adhesion and advancing contact angle as the mechanisms limiting the minimum droplet departure size on structured surfaces. We predict that the evolved pillar length scale and topology of the superhydrophobic cicada wings allows the coalescence-induced jumping of water nanodroplets[27]. In considering the design of surface structures for jumping droplet functionality, the combined effects of adhesion, contact angle hysteresis, and initial wetting behavior governed by the surface structure morphology and length scale play a defining role. Indeed, it is the coupling of both hydrodynamic and wetting mechanisms that ultimately governs both the minimum droplet jumping size on any given superhydrophobic surface and the reduction in jumping speed at low droplet radii[27]. Interestingly, the topologies observed on *N. pruinosus*, *N. tibicen* and *Me. dorsatus* all fit within the optimum structure length scale and topology to minimize droplet jumping radii, and hence maximize self-cleaning, anti-fogging, and anti-reflecting efficacy.

As observed in the wetting behavior results, the natural habitat of the cicada species held little predictive ability of the resulting jumping-droplet efficacy. Instead, cicada relatedness was a greater predictor, with the more closely related *N. pruinosus*, *N. tibicen* and *Me. dorsatus* species all showing vigorous droplet jumping, and more distant *Ma. septendecim* cicada showing no jumping.

2.3.6. Importance of Life History

Superhydrophobicity in our study is seen in the annual cicadas, *N. tibicen*, *N. pruinosus*, and *Me. dorsatus*. The periodical cicada, *Ma. septendecim*, did not demonstrate superhydrophobicity or droplet-jumping behavior. We propose that the difference in life history strategy may be a driving factor in the range of hydrophobicity seen in these Midwestern species. *Ma. septendecim* adults emerge *en masse* every 17 years and live for only two to four weeks aboveground. This life history strategy of a long life-cycle and synchronized emergence is thought to avoid an abundance of predation[105]. The annual cicadas, however, emerge over a longer period, throughout the summer and early fall (July through September, sometimes later), hence their chance of reproductive success relies on their longer survival in the wild, where superhydrophobic features having a multitude of functionalities would help to achieve this. Habitat may play a role in a smaller range of hydrophobicity where *Me. dorsatus* has the lowest hydrophobicity due to lack of evolutionary driving forces/pressure in drier prairie systems. Both *N. pruinosus* and *N. tibicen* live in a variety of woodland habitats (occasionally in grasslands) across a broad geographic range. In fact, the specimens of *N. tibicen* used in this study were collected near a cypress swamp in Southern Illinois, presumably exposed to large amounts of humidity, moist soil, and higher rainfall.

Table 2-3 lists a summary of the studied cicada species, their wettability, topology, and predicted self-cleaning (jumping behavior). The present study shows that the evolved function of the cicada wing nanostructures cannot be attributed to wetting only. If wetting was the only function of the pillars, we would expect all cicada species living in wet habitats to demonstrate superhydrophobicity and self-cleaning behavior, which is not true as observed on the *Ma. septendecim* species and some other cicada species. Instead, the structure topology, length scale, and functionality blend to achieve multiple evolved functions. For example, while exposure to fog

strongly compromises the water-repellency of hydrophobic structures, this failure can be minimized by scaling the texture down to the nanoscale[38].

Table 2-3 Topological and wetting data of cicada species.

Cicada Species	Habitats	Wettability	Structure Length Scale	Droplet Jumping	Reference
Subfamily-Tribus: Cicadinae – Cryptotampanini					
Neotibicen pruinosus (North American)	Urban parks, grasslands, and hardwood forest	SHPB	~ 100 nm	YES	This Study
Neotibicen tibicen (North American)	Bottomland hardwood forest and swamps	SHPB	~ 100 nm	YES	This Study
Megatibicen dorsatus (North American)	Forbs in prairie habitat	SHPB	~ 100 nm	YES	This Study
Psaltoda claripennis (Australian)	Open forest, woodland and gardens.	SHPB	~ 100 nm	YES	[51-52]

* Table continues on the next page
**SHPB: Superhydrophobic, HPB: Hydrophobic

Table 2-3 (cont.) Topological and wetting data of cicada species.

Subfamily-Tribus: Cicadettinae – Taphurini					
Magicicada septendecim (North American)	Periodical (13-17yrs), widespread, Mixed-mesophytic hardwood forest (in this study)	HPB	~ 50 nm	NO	This Study
Aleeta curvicosta (Australian)	Humid areas of open forest, mangroves, paperbark woodlands city parks and suburban gardens.	SHPB	~ 100 nm	YES (Predicted)	[51]
Subfamily-Tribus: Cicadettinae – Cicadettini					
Gudanga sp. nr adamsi (Australian)	Eucalyptus and/or acacia woodland	SHPB	~ 100 nm	YES (Predicted)	[66]
Ewartia oldfieldi (Australian)	Acacia thickets	SHPB	~ 100 nm	YES (Predicted)	[66]
Subfamily-Tribus: Cicadettinae – Chlorocystini					
Cystosoma schmeltzi (Australian)	Dry sclerophyll forest and woodland. Small trees and shrubs around rural towns	HPB	~ 100 nm	NO (Predicted)	[66]

* Table continues on the next page
**SHPB: Superhydrophobic, HPB: Hydrophobic

Table 2-3 (cont.) Topological and wetting data of cicada species.

Subfamily-Tribus: Cicadinae: Dundubiini				
Megapomponia intermedia (Southeast Asia)	HPB	~ 100 nm	NO (Predicted)	[67]
Megapomponia intermedia (Southeast Asia)	HPB	~ 100 nm	NO (Predicted)	[92]
Ayuthia spectabile (Southeast Asia)	HPB	~ 100 nm	NO (Predicted)	[67]
Subfamily-Tribus: Cicadinae: Cryptotympana				
Cryptotympana atrata (South Korea, China)	HPB	~ 100 nm	NO (Predicted)	[60, 106]
Cryptotympana aquila (Southeast Asia)	HPB	~ 100 nm	NO (Predicted)	[67]

**SHPB: Superhydrophobic, HPB: Hydrophobic

The observed correlation in Table 2-3 between annual cicada species phylogenetic relatedness and its wing superhydrophobic properties begs the question of whether it is possible to predict wing functionality for other untested cicada species. Wettability and topology for other cicada species are presented in Table 3 together with our prediction for self-cleaning by the jumping droplet phenomenon. As illustrated in Table 2-3, wettability of a cicada wings seems to correlate well with its taxonomy – tribes tend to be either superhydrophobic or hydrophobic. Although the number of species studied so far is limited, previous studies and our current study results suggest a relationship between tribe and wettability.

The clear outlier in Table 2-3 is the Taphurini tribe in the subfamily Cicadettinae; however the tribe member, *Ma. septendecim* is the only periodical cicada in this set. With regard to functional

similarities, lifecycle attributes may supersede taxonomic relatedness. These considerations may serve to highlight next choices of cicada species for study, depending on the desired functionality. Annual cicada species with longer emergent times will likely possess enhanced protective properties, while these features are less important to periodical cicada species.

Going forward, we encourage researchers who take a biomimetic or bioinspired approach to give detailed taxonomic and biological information when reporting and discussing their results. Biological systems are incredibly diverse and only by linking detailed engineering parameters (material properties, biomechanics, etc.) to evolutionary and environmental analyses, can the most desirable combination of traits be determined and incorporated into viable bioinspired innovations[107]. Cicadas and other insects provide a large data set on how to achieve a variety of desirable material properties. However, single species studies are limiting when trying to determine which traits are most desirable to mimic. Incorporating the evolutionary and life history of an organism will be more efficient in the end for informing bioinspired material design.

2.4. Conclusions

Here, we studied taxonomic, life history and topological influences on the wettability of cicada wings. Among the four species studied, three annual cicadas showed superhydrophobicity with jumping droplet phenomena while the periodical cicada species, *Ma. septendecim* was hydrophobic. The nanopillar arrays were distributed similarly (≈200 nm in pitch) in the lateral direction for all species, with distinctive pillar heights ranging from 50 to 400 nm. In addition to topological differences, we examined how phylogenetic relatedness and habitats of cicadas affect wing wettability through a comparative approach, showing that habitat, although having a mild effect on degree of hydrophobicity, was a poor predictor of wing wettability. Rather, the results

pointed to species relatedness as a better predictor of surface wettability and multi-functional behavior. In addition, our results point to cicada reproductive strategy and length of life after emergence as the evolutionary pathway for wing superhydrophobicity to increase the likelihood of survival, and hence reproductive success. This work not only elucidates the differences between inter- and intra-species cicada wing topology, wettability, and water shedding behavior, but enables the development of rational design tools for the manufacture of artificial surfaces for energy and water applications such as anti-icing, self-cleaning, anti-fogging, water harvesting, and enhanced phase change heat transfer.

CHAPTER 3: SUPERHYDROPHOBIC SURFACES MADE FROM NATURALLY DERIVED HYDROPHOBIC MATERIALS*

3.1. Introduction

Superhydrophobic surfaces are defined as substrates which will cause a residing water droplet to take on an apparent advancing or receding contact angle greater than 150°, when measured from the liquid-solid interface to the liquid-vapor interface[108]. Due to the low droplet-surface adhesion, characterized by low contact angle hysteresis and roll-off angle[109-110], superhydrophobic surfaces have many uses in self-cleaning[56], anti-fogging[38, 41-43, 111], anti-fouling[44-45], anti-corrosion[112-114], anti-bacterial[46-48], anti-icing[46, 115-116], enhanced condensation[25, 103, 117], energy harvesting[28, 118-119], and drag reduction[120-122] applications. The past decade has seen a large increase in research by academics, industrial scientists, and engineers related to the fabrication of superhydrophobic surfaces which require a combination of meso/micro/nanoscale structure with a conformal hydrophobic coating[123-124]. The surface roughness and surface energy govern the wettability of water of superhydrophobic surfaces. In general, low surface energy, high coating conformality with few defects, and high roughness results in larger water droplet apparent advancing contact angle, lower hysteresis, and greater superhydrophobicity[108, 125-126].

Due to their ultra-low surface energy (≈10 mJ/m^2), perfluorinated or alkyl-based synthetic chemicals are typically utilized as the conformal hydrophobic coating to achieve high intrinsic

* This chapter was reprinted (adapted) with permission from *ACS Sustainable Chem. Eng.*, **2017**, *5* (12), pp 11362–11370 Copyright © 2017 American Chemical Society. Junho Oh was a co-first-author. He conducted surface characterization experiments and analyzed the data with the other co-first-author, Dr. Mohamad Seyed Razavi. Junho Oh partially wrote the manuscript with Dr. Nenad Miljkovic as the corresponding author of the publication.

contact angles (> 90°).[127-129] The most common chemicals for coatings are organosilanes that are terminated with silanol group from the hydrolysis process of trialkoxysilanes. Among three silanol groups, generally, only one silanol group react with a hydroxyl group on a substrate at the interface. The other silanol groups mostly condense with other organosilane molecule or stand free at the end of the condensed molecule which forms self-assembled monolayer (SAM) coating[130].

Due to the cost of processing and materials, toxicity, and environmental hazards associated with the emission of organosilane and fluorine compounds, alternative hydrophobic coatings have begun to be heavily investigated[131-132]. Numerous researchers have reported the importance of replacing fluorinated compounds in industries such as textile manufacturing[133]. Many fluorinated organics, especially perfluorinated compounds (PFC), are environmentally persistent, bio-accumulative, and potentially harmful[134]. Although perfluorinated materials have been the subject of many prior studies that have shown high levels of bio-accumulative in wildlife and bio magnification potential in food webs[135], not enough it known about the occurrence, transport, biodegradation, and toxicity of these compounds in the environment[134]. Another concern is that certain volatile fluorinated compounds can be oxidized in the troposphere, yielding nonvolatile compounds such as trifluoroacetic acid[134]. Material safety data sheets for perfluorinated and alkyl-based organosilanes list a number of hazardous thermal-decomposition products for the coatings such as hydrogen fluoride (HF), perfluoroisobutylene, carbon dioxide, carbon monoxide, and known carcinogens such as methyl ethyl ketoxime[133]. At the processing level, researchers working with fluorinated organic compounds (FOC) have shown organic fluorine levels in their blood serum from 1 to 71 ppm (normal organic fluorine level in blood serum is 0 to 0.13 ppm)[134]. Apart from health and environmental concerns, the processing of fluorocarbon polymers is difficult and expensive. Therefore, it is very desirable to find replacements for these hydrophobic chemicals.

In this study, we develop two hydrophobic and superhydrophobic coating methods with alternative non-fluorinated and non-organosilane synthetic chemicals, based on naturally derived compounds. The chemicals are derived from two plant species (cinnamic or myristic acid), are alkyl based, and can significantly decrease surface energy. The morphology, wettability and the chemistry of surfaces were investigated using scanning electron microscopy, atomic force microscopy, X-Ray photoelectron spectroscopy, high-speed optical microscopy, micro-goniometry, and ellipsometry. Ideal coating process parameters are developed for coating on smooth surfaces as well as micro- and nanostructured copper oxide surfaces. The work here presents two alternative, environmentally friendly, non-toxic, and inexpensive functional coatings to organosilane-based alkyl and perfluorinated synthetic chemicals.

3.2. Experimental Methods

To fabricate hydrophobic surfaces, silicon wafers (2 inch, p type, boron-doped, [1 0 0] orientation, SSP, test grade) as well as commercially available Cu tabs (25 mm x 25 mm x 0.8 mm, 99.90% purity, polished) were first ultrasonically treated in acetone, followed by ethanol for 5 min each. After cleaning, the samples were dried in a clean N_2 stream. The specimens were then plasma cleaned in an air plasma at high power for 5 minutes, creating exposure of hydroxyl (OH) binding sites on the silicon and metal oxide surfaces.

To synthesize the microstructured surface, we used commercially available brushed finish oxygen-free Cu tabs (25 mm x 25 mm x 0.8 mm, 99.90% purity). Prior to functionalizing, each brushed Cu tab was cleaned in an ultrasonic bath with acetone for 10 min and rinsed with ethanol, isopropyl alcohol and deionized (DI) water. The substrates were then dipped into a 2.0 M hydrochloric acid solution for 5 min to remove the native oxide film on the surface, then rinsed with DI water, and

dried with a clean nitrogen stream. The specimens were then plasma cleaned in an air plasma at high power for 5 minutes, creating exposure of hydroxyl (-OH) binding sites on the microstructured metal oxide surfaces.

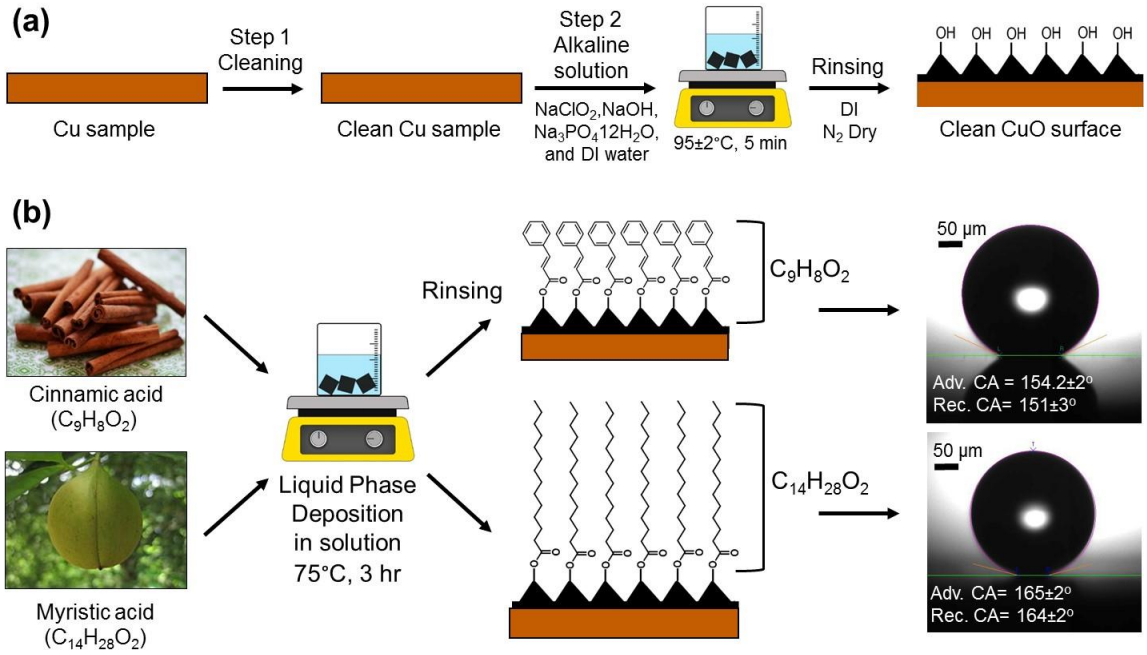

Figure 3-1 Schematic of the superhydrophobic coating process showing the (a) copper based nanostructure fabrication steps and (b) application method for natural hydrophobic chemicals on the surface in (a) with corresponding images of advancing contact angles.

To synthesize the nanostructured surface, we used commercially available oxygen-free Cu tabs (25 mm x 25 mm x 0.8 mm, 99.90% purity). Prior to nanostructuring, each Cu tab was cleaned in an ultrasonic bath with acetone for 10 min and rinsed with ethanol, isopropyl alcohol and deionized (DI) water. The substrates were then dipped into a 2.0 M hydrochloric acid solution for 5 min to remove the native oxide film on the surface, then rinsed with DI water, and dried with a clean nitrogen stream. Nanostructured copper oxide films were formed by immersing the cleaned

substrate into a hot (95 ± 2°C) alkaline solution composed of $NaClO_2$, NaOH, $Na_3PO_4{\cdot}12H_2O$, and DI water (3.75:5:10:100 wt. %). During the oxidation process, a thin and conformal Cu_2O layer is initially formed on the copper surface that then re-oxidizes to form sharp, spike-like CuO oxide structures (Fig. 3-1a).[101]

To functionalize the smooth and rough samples, the surfaces were subsequently immersed in an ethanol solution of cinnamic acid (Sigma Aldrich, CAS #140-10-3) or myristic acid (Sigma Aldrich, CAS #544-63-8) with varying weight percent to volume (100 ml) concentration (1-10 %wt./vol. and 0.25-4.0 %wt./vol. for cinnamic acid and myristic acid, respectively) at 75°C for 3 hours (Fig. 3-1b). To facilitate heating, a lid was placed on top to seal the solution container, followed by heating on a hot plate. This process allows for the development of a highly conformal coating as the hydrophobic acid molecules deposit on the samples in the liquid phase. In addition, 20 %wt. of N,N-dicyclohexylcarbodiimide (DCC, Sigma Aldrich, CAS #538-75-0) to the amount of acid was added to the solution as a dehydration reagent which can facilitate the formation of the covalent bond between carboxyl groups and hydroxyl groups without being adsorbed onto the surface[136]. After deposition, the silicon, microstructured copper, and nanostructured copper oxide substrates were removed from the solution, rinsed with ethanol and deionized water thoroughly, and then dried with clean N_2.

Low and high resolution field emission scanning electron microscopy (FESEM) images of each sample were obtained using an FEI Quanta 450 ESEM in high vacuum operation mode. The accelerating voltage was set to 5 kV, with a spot size of 2.0 nm, to prevent charging and sample damage by the electron beam. Micropillar shape and overall surface topology were characterized by positioning the sample perpendicular to the electron beam.

Topological characteristics of the nanostructured samples were investigated using an Asylum Research MFP-3D atomic force microscope in tapping mode. General tapping mode AFM tip with aluminum reflex coating (TAP300AL-G, BudgetSensors) was used for AFM scans. The AFM scan area was 10 µm by 10 µm. Each AFM scan profile was flattened to be leveled at the base. We used open-source software, Gwyddion, to process, analyze and visualize the AFM scan data[137].

Spatially resolved ellipsometry (J.A. Woollam VASE Ellipsometer) measurements were performed on the smooth Si samples for both cinnamic and myristic acid to gain a more quantitative understanding of surface coverage. The coated wafer was modeled as a three-layer system with the coating, silicon dioxide and silicon substrate. The refractive index for the coating was modeled as a function of wavelength (λ, 450-700 nm), $n = 1.5261 + 0.00743\lambda^{-2} + 0.00116\lambda^{-4}$ for cinnamic acid[138] and $n = 1.437 + 0.0072\lambda^{-2} + 0.00108\lambda^{-4}$ for myristic acid[139]. The middle Si oxide layer had a thickness of zero (0.0014 nm) with refractive index and extinction coefficient κ = 0.[140]. The silicon substrate had a refractive index n = 3.874 and κ = 0.01616.[141]

To determine the surface chemistry, XPS measurements were performed at grazing (15°) and normal takeoff angles using a Kratos Axis ULTRA instrument (Kratos Analytical, Ltd., UK). The functional group composition was calculated using high-resolution spectra with relative sensitivity factors for carbon and oxygen of 0.278 and 0.711, respectively. The XPS data were analyzed using CasaXPS software (Casa software, Ltd., UK).

Contact angle measurements of ≈100 nL droplets on all samples and were performed using a microgoniometer (MCA-3, Kyowa Interface Science). The advancing and receding contact angles were measured at five spots on each sample and the results averaged. Droplets were injected using a piezoelectric injector at the rate of 60-80 droplets/sec. All contact angle data analyzed using the

image processing software (FAMAS, interFAce Measurement & Analysis System) with the circle fitting method.

The durability of the liquid phase deposited cinnamic acid and myristic acid samples were tested both by mechanical abrasion and in different pH conditions. For the mechanical abrasion test[142], the superhydrophobic surface was placed facedown to 2/0 grid Emery polishing paper (3M). A 100 g weight was placed on top of the sample. The sample along with the weight was then moved 10 cm at a constant speed. This cycle was repeated five times for each sample. Contact angle measurements were taken after every cycle to see the effect of abrasion on the coated surface.

The samples were also tested for chemical degradation in different acidic and basic solutions. The fabricated samples were immersed in each standard pH solution (Fisher Chemical) of pH = 2, 4, and 10 for 5 mins. The samples were then removed and rinsed twice with ethanol and dried with nitrogen before measuring contact angles with the microgoniometer.

Jumping droplet condensation experiments were performed using a customized top-view optical light microscopy setup[88]. A high-speed camera (Phantom, V711, Vision Research) was attached to the upright microscope (Eclipse LV100, Nikon) for top view analysis, performing video recordings at variable frame rates up to 500,000 frames per second. Samples were horizontally mounted to a cold stage (TP104SC-mK2000A, Instec) and cooled to the test temperature of T_w = 2-5 ± 0.5°C, in a laboratory environment having air temperature, T_{air} = 23 ± 0.5°C, and relative humidity, Ø=30-50 ± 1% (Roscid Technologies, RO120). Illumination was supplied by an LED light source (SOLA SM II Light Engine, Lumencor). The LED light source was specifically chosen for its high-intensity, low power consumption (2.5W) and narrow spectral range (380-680 nm) in order to minimize heat generation at the surface due to light absorption. Furthermore, by manually reducing the condenser aperture diaphragm opening size and increasing the camera exposure time,

we were able to minimize the amount of light energy needed for illumination and hence minimize local heating effects during condensation experiments. Imaging was performed with a 20X (TU Plan Fluor EPI, Nikon), 50X (TU Plan Fluor EPI, Nikon), or 100X (TU Plan Fluor EPI, Nikon) objective. All experiments were conducted at supersaturations, S = 1.02 ± 0.035, below the critical supersaturation associated with surface flooding conditions for many micro and nanostructured superhydrophobic surfaces ($S = P_{\mathrm{v}}/P_{\mathrm{sat}}(T_{\mathrm{w}}) < S_{\mathrm{c}}$).[24, 38, 102, 143-145] This was done in order to remain in the droplet jumping regime to study the coalescence and departure dynamics.

3.3. Results and Discussion

3.3.1. Wettability and Morphology of the Superhydrophobic Surface

To identify the optimum deposition parameters for cinnamic and myristic acid, we varied the solution concentration during liquid phase deposition (LPD). The optimum concentration was defined as the solution concentration which resulted in the highest apparent advancing contact angle, with the lowest contact angle hysteresis, for that particular surface. When the maximum advancing contact angle and minimum hysteresis did not coincide at the same deposition concentration, the concentration resulting in the maximum advancing contact angle was defined as the optimum. The deposition time was also investigated, showing a little effect on the resulting contact angle after immersion times of 120 min. The solution temperature of 75°C was chosen due to the acid solubility in the solvent and the elevated rate of covalent bond formation on the substrate at higher temperatures. Liquid phase deposition was chosen as an ideal method to coat the samples due to simplicity, cost-effectiveness, speed of deposition, and most importantly, the ability to coat arbitrarily shaped substrates.

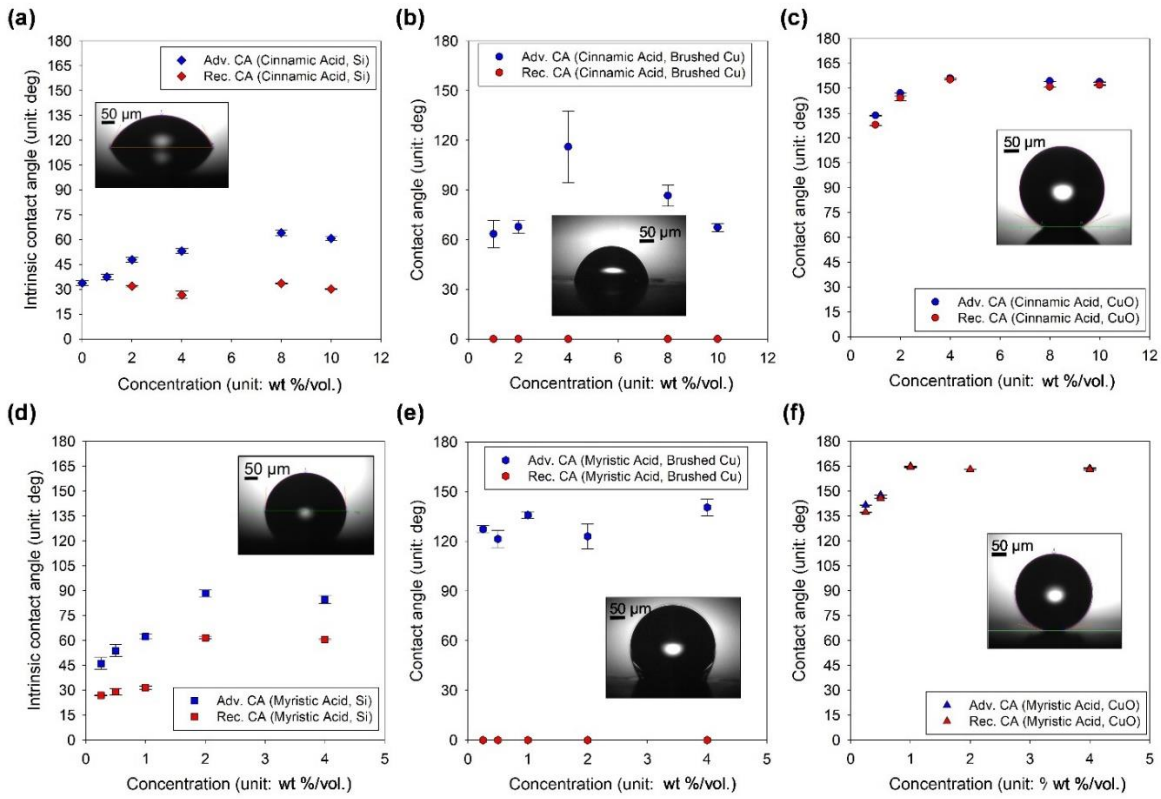

Figure 3-2 Advancing and receding contact angle measurements on the Si wafer, brushed Cu, and CuO, surfaces having depositions with different concentrations of (a, b, c) cinnamic acid and (d, e, f) myristic acid, respectively. Advancing contact angles measured on the cinnamic acid coating (a, e) at the optimum concentration of 8 %wt./vol. were 64.1 ± 5° and 154.2 ± 2° on the Si wafer and CuO, respectively, and receding contact angles were 33.6 ± 4° and 151 ± 3°, respectively. Advancing contact angles measured on the myristic acid coating (b, f) at the optimum concentration of 4 %wt./vol. were 88.4 ± 5° and 165 ± 2° on the Si wafer and CuO, respectively where receding contact angles were 61.6 ± 4° and 164 ± 2°, respectively. Insets: Images of the receding droplet shape on each surface coated with (a, c, e) cinnamic acid and (b, d, f) myristic acid. Note, droplets residing on the brushed Cu surface were in the Wenzel wetting state, resulting in a zero apparent receding angle due to pinning on the microstructures.

Figure 3-2 shows the resulting advancing and receding contact angle measurements on the smooth Si, microstructured Cu (brushed), and nanostructured CuO substrates as a function of cinnamic and myristic acid concentration. Contact angles on the smooth Si wafers (Fig. 3-2a,b) increased as a function of acid concentration and were observed to saturate at the intrinsic advancing contact angle for both cinnamic acid (≈ 60°) and myristic acid (≈ 85°). On the brushed Cu substrates (Fig. 3-2c,d), deposited droplets took on the Wenzel wetting morphology, forming hydrophobic states for both cinnamic acid (≈ 120°) and myristic acid (≈ 145°). The Wenzel droplet morphology on brushed Cu resulted in contact line pinning and low apparent receding angle (≈ 0°) for both chemistries. On the rough CuO surface (Fig. 3-2e,f), the contact angle showed asymptotic behavior towards superhydrophobic states ($\theta_a^{app} \rightarrow 180°$) with increasing acid concentration due to the increasing area coverage of the self-assembled monolayer. To check the conformality of the coatings, we performed SEM, AFM and ellipsometry analysis on the coated CuO samples. Figure 3-3 shows the knife-like CuO oxide structures with heights of $h \approx 1$ μm, solid fraction $\varphi \approx 0.023$, and roughness factor $r \approx 10$.[24] Indeed, AFM scans revealed that the surface roughness, defined as the total area normalized by the projected area was $r \approx 2.2$, with an RMS roughness of 240 nm. The discrepancy between previously estimated surface roughness values (≈ 10) and our AFM measurements was attributed to the inability of the AFM tip to penetrate complex (non-vertical) and small voids due to the finite size of the AFM tip. The microstructures look identical to in SEM and AFM scans prior to and after the LPD, indicating quasi-conformal deposition of the cinnamic and myristic acid on the surface. Spatially resolved ellipsometry results on smooth Si wafers showed a uniform coverage of the coating on each surface, with hydrophobic coating thickness of 2.43 ± 0.22 nm and 2.49 ± 0.61 nm for cinnamic and myristic aid, respectively. It is important to note, the reduced intrinsic contact angles on the smooth Si samples is not indicative of the intrinsic

contact angle of the SAM coatings on smooth CuO surfaces. Rather, the different concentration of binding hydroxyl sites on the surface, and different substrate materials resulted in reduced contact angle behavior on the smooth surface than expected. Previous studies have shown that the temperature history of an oxide surface can influence the degree of surface hydroxylation, which, in turn, affects the intrinsic receding contact angle[146-147]. Indeed, advancing and receding contact angle measurements at the optimum concentration of 0.1 M and 0.04 M for cinnamic and myristic acid, respectively, on polished copper samples, yielded intrinsic advancing and receding contact angles of θ_a/θ_r = 101.8 ± 4°/86.3 ± 3° and θ_a/θ_r = 119 ± 4°/105.7 ± 2° for cinnamic and myristic acid, respectively.

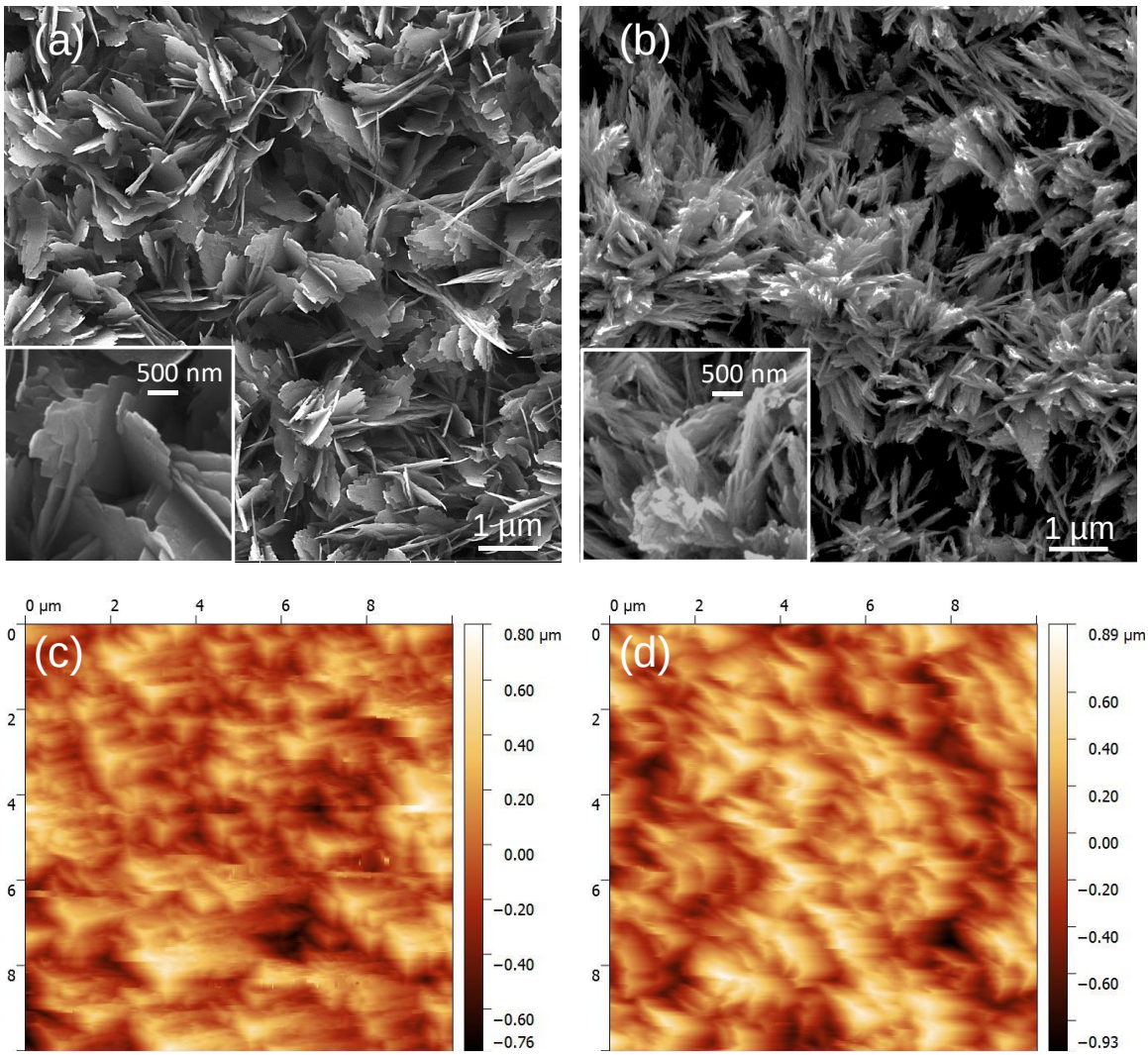

Figure 3-3 Scanning electron micrographs of the of the flake-like CuO microstructures coated with (a) cinnamic acid, and (b) myristic acid. Atomic force microscopy images of the CuO microstructures coated with (c) Cinnamic Acid (d) Myristic acid. Distinction between the structures prior to and after coating was not possible, indicating the deposition of an untra-thin (<5 nm) SAM layer.

3.3.2. XPS Results

In order to understand the surface chemistry after LPD, two separate superhydrophobic CuO samples were functionalized with cinnamic and myristic acid at optimum concentrations (0.1 M and 0.04 M for cinnamic and myristic acid, respectively) and immediately afterward (<5 min) analyzed via XPS. Broadband energy scans (Fig. 4a,b) revealed the presence Cu, O, and C on the sample surface. High-resolution C 1s and O 1s spectra of the samples revealed the presence of C-O, C-C, and Cu = O bonds on both samples in accordance to the predicted molecular structure of the acid molecules (Fig. 3-1b). Note, the C-C bond signal was larger for myristic acid due to the longer carbon chain compared to cinnamic acid. Binding energies for the functional groups used in high-resolution XPS spectra curve fitting were selected based on several references[48].

Table 3-1 XPS curve fitting results from high-resolution spectral scan for CuO surface coated with cinnamic acid and myristic acid.

Chemical		Name	Position	FWHM	%At
Cinnamic acid ($C_9H_8O_2$)	C1s	C=C (Aromatic)	284.2	1.39	56.27
		O-C=O	287.7	1.25	4.65
	O1s	Cu=O	529.1	1.33	24.84
		C-O	530.6	1.54	14.24
Myristic acid ($C_{14}H_{28}O_2$)	C1s	C-C (Aliphatic)	285.4	1.19	64.59
		O-C=O	288.9	1.2	3.85
	O1s	Cu=O	530.3	1.01	13.03
		C-O	531.7	2.02	18.53

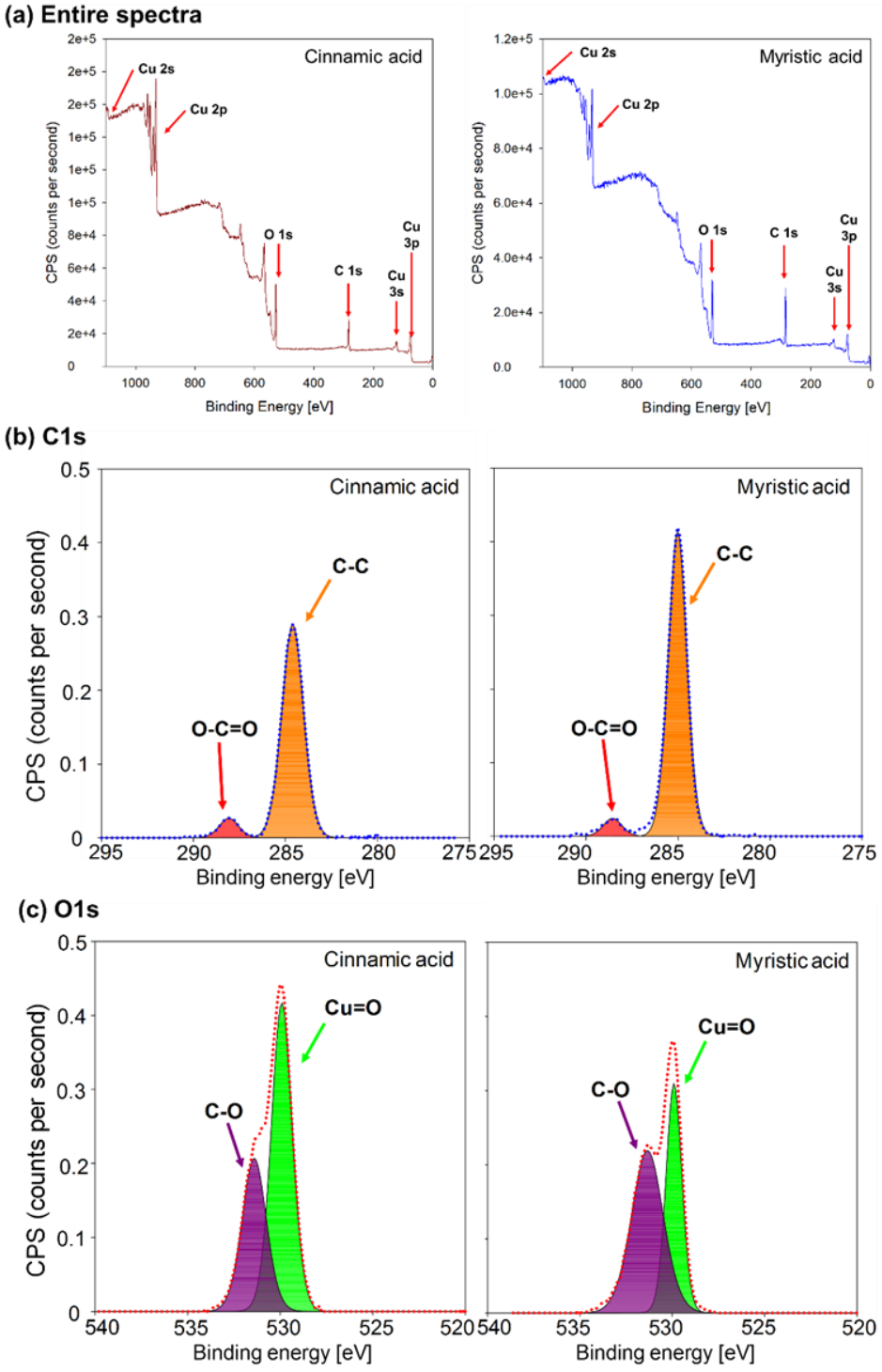

Figure 3-4 XPS spectra of the CuO surface coated with cinnamic and myristic acid showing (a) broadband scan results, (b) high-resolution spectra for C1s, and (c) high-resolution spectra for O1s.

Curve fitting of high-resolution O1s and C1s data was performed using the information in Table 3-1. The atomic percentage of each chemical bonding in Table 3-1 was calculated based on curve fitting of high-resolution spectra for each bonding and atomic concentration of each element obtained from entire spectral survey. The ratio of carbon (C-C) to carboxylic group (O-C=O) bonding was calculated for each sample because the carboxylic functional group would indicate the surface modification of the acids with the CuO surface. The bonding ratios were 12.1 and 16.7 for cinnamic and myristic acid, respectively, where the ratio for myristic acid was ≈1.4 times higher than the one for cinnamic acid. This proved the presence of each acid on the CuO surface and its functionalization. Theoretically, the bonding ratio for MA should be as high as the carbon atomic ratio of each acid (9:14). Carbon and oxygen atomic percentage from XPS spectra often show discrepancy from the theoretical atomic percentage since a surface absorbs carbon and oxygen from the aerial environment.

3.3.3. Durability

The nanostructured CuO samples fabricated from optimum concentrations of cinnamic acid (8% wt./vol.) and myristic acid (2% wt./vol.) were chosen for durability testing. Figure 3-5a,b show the apparent advancing contact angle behaviors of the CuO surfaces when immersed in varying pH solutions. Cinnamic acid had a higher sensitivity to the pH of the solution, showing rapid degradation within minutes due to the removal of the functional coating as well as the CuO nanostructures. Nanostructure degradation was observed via the brightening of the normally black CuO nanostructured substrate. Acidic conditions in particular were detrimental to coating longevity due to possibility of reduction of the nanostructured CuO oxide layer and removal of the

structure completely. Myristic acid on the other hand showed greater resiliency to low pH levels, likely due to the higher conformality of the coating, and better barrier properties.

Mechanical abrasion tests (Fig. 3-5c,d) revealed similar trends as the pH tests, showing myristic acid to be more resilient to mechanical wear than cinnamic acid over multiple abrasion cycles. Interestingly, the myristic acid coated CuO surface showed negligible degradation over multiple abrasion cycles up to five cycles. This was attributed to both the high conformality and binding energy of the coating, as well as the ability of abraded oxide blades to remain on the surface after being removed and continue to act as roughness to deposited droplets. Cinnamic acid, however, did not show the same resiliency, degrading after only two abrasion cycles.

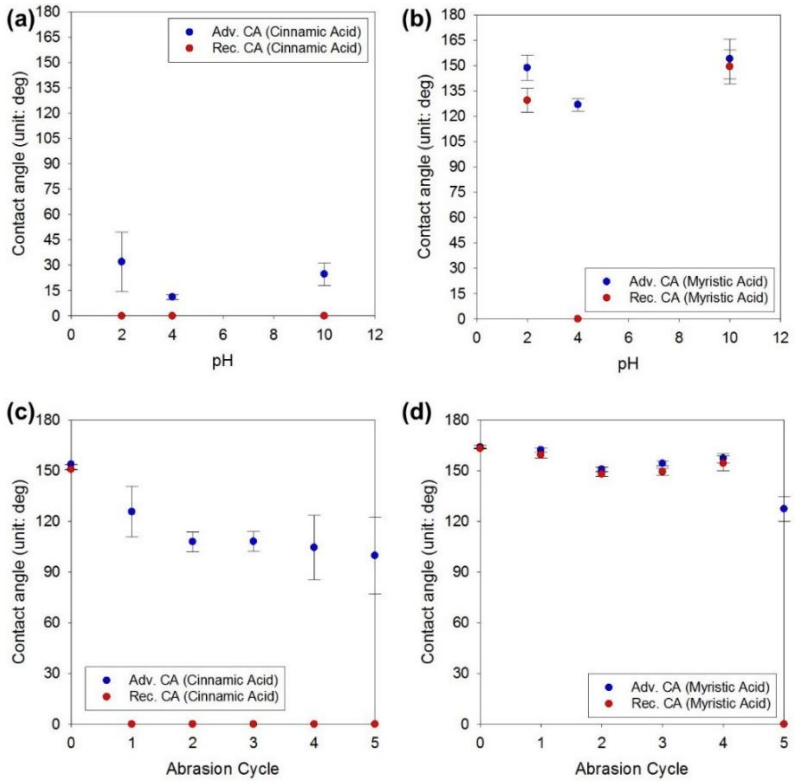

Figure 3-5 Apparent advancing and receding contact angles for the CuO surface during pH degradation tests on (a) cinnamic and (b) myristic acid, and mechanical abrasion degradation tests on (c) cinnamic and (d) myristic acid. For both degradation conditions, myristic acid showed higher durability than cinnamic acid.

3.3.4. Jumping Droplet Condensation

Droplet jumping is a process governed by the conversion of excess surface energy into kinetic energy when two or more droplets coalesce and involves a symmetry-breaking surface. For the simplest case of two, equally sized inviscid spherical droplets coalescing on a surface with no adhesion, an energy-balance gives a characteristic jumping speed that follows an inertial-capillary scaling.[33, 148] Droplet growth on the superhydrophobic CuO surfaces was characterized using optical microscopy in ambient conditions. Condensed droplets with diameters as small as 2 ± 0.4 μm demonstrated large apparent contact angles similar to the macroscopically measured value (Fig. 3-6). A conservative estimate of the droplet radius-dependent advancing angle indicated that all measured droplet jumping events were in a constant contact angle growth mode[101, 149-151]. Since the characteristic roughness spacing length scales of the surfaces (pitch ≈ 1 μm), were significantly smaller than the smallest droplet jumping diameter measured (≈ 10 μm), we were able access a droplet growth regime well above the flooding limit with droplets growing in a constant apparent contact angle mode[27-28].

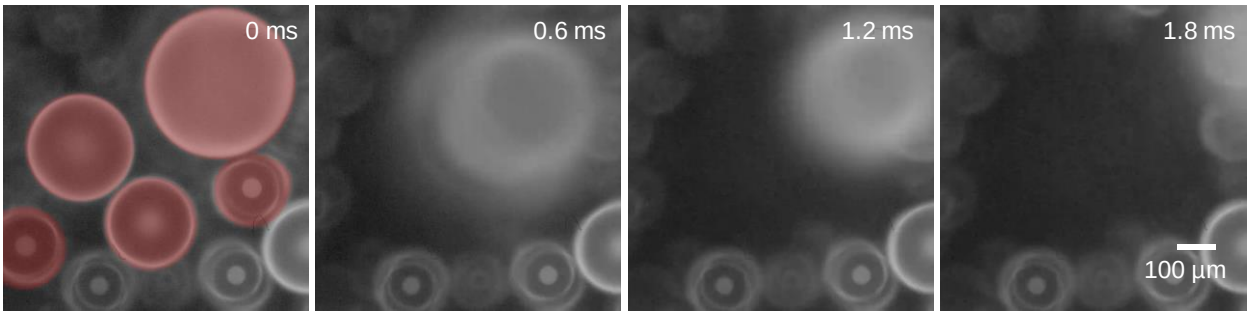

Figure 3-6 Top-view optical microscopy time-lapse images of water vapor condensation on a myristic acid superhydrophobic CuO surface. The video was taken at 5000 fps. Although the roll-off angle was low, droplet jumping was not observed on the cinnamic acid coated CuO surface due to the lower advancing contat angle and higher contact angle hysteresis.

Figure 3-6 shows top-view time-lapse images of condensation on the wing. Partially wetting droplets nucleated within a unit cell (area between pillars), and while growing beyond the confines of the unit cell, their apparent contact angle increased and they spread across the tops of the pillars in the shape of a balloon with a liquid bridge at the base of the pillars. Before coalescence with neighboring droplets, an increasing proportion of the droplet contact area was in the Cassie-Baxter state as observed in the deposited droplets during micro-goniometry. Upon coalescence, droplet jumped away from the CuO surface functionalized with myristic acid. However, droplet jumping was not observed on the CuO sample functionalized with cinnamic acid due to the larger contact angle hysteresis. Although the apparent advancing contact angle for the cinnamic acid coated CuO surface was above the zero-adhesion jumping limit (> 150°)[27], the finite contact angle hysteresis along with microscale structure length scale increased the droplet-surface adhesion[144], and prevented jumping.

Internal viscous dissipation plays a limited role in the jumping process for the experimentally accessible low Oh number regime studied here ($Oh = \mu/(\rho R\gamma)^{1/2} < 0.1$, where μ, ρ, R, and γ are the liquid droplet dynamic viscosity, density, radius, and surface tension). Instead, finite droplet-surface adhesion dominates the jumping process. Due to the ultra-low contact angle hysteresis (< 15°) and homogeneous topology and wetting of the myristic acid coated sample, we observed vigorous droplet jumping on all areas. This is in accordance with the longer molecular structure of the myristic acid, and hence, higher non-polarity and hydrophobicity when compared to the cinnamic acid.

3.4. Discussion

The environmentally friendly hydrophobic coatings developed here are not the first acids to be utilized as hydrophobic coatings. Table 3-2 shows a summary of previous environmentally friendly acids and their wetting performance. The results shown here show some of the highest levels of superhydrophobicity (characterized via the advancing contact angle), especially for myristic acid, which was shown to have stable droplet jumping. Furthermore, in addition to non-wetting, cinnamic and myristic acid have recently been shown to be anti-bacterial in nature[111, 152-154]. This gives significant promise to the superhydrophobic coatings developed here for not only non-wetting applications such as enhanced heat transfer, but for non-thermally related applications where bacterial growth may be a significant issue. Interestingly, the results of Table 3-2 show little correlation between the maximum advancing contact angle and the number of carbon atoms in the functional molecule. Although counter intuitive, this may be due to the deposition technique used by each respective study, which may not be liquid phase deposition, and may not have optimized deposition parameters such as acid concentration as studied here (Fig. 3-3).

Table 3-2 Summary of the wettability of green chemicals for achieving hydrophobicity**.**

Chemical	Number of carbon atoms	Advancing Contact angle	Reference
Cinnamic acid ($C_9H_8O_2$)	9	154° ± 2°	This study
Myristic acid ($C_{14}H_{28}O_2$)	14	165° ± 2°	This study
Carnauba Wax	26 – 30	162°	[155]
Beeswax	15 - 30	155°	[155]
Stearic acid ($C_{18}H_{36}O_2$)	18	154°	[136]
Octadecylphosphonic acid ($C_{18}H_{39}O_3P$)	18	150°	[156]
Decylphosphonic acid ($C_{10}H_{23}O_3P$)	10	120°	[156]
Octylphosphonic acid ($C_8H_{19}O_3P$)	8	78°	[156]

In the future, it would be interesting to study bioaccumulation dynamics of cinnamic and myristic acid in order to better define their environmental impact after use. Furthermore, future work should investigate the durability of cinnamic and myristic acid coatings after depositions. Although no visible degradation was observed in the studies conducted here, the time scales of the experiments was much too short (weeks) to have concussive evidence regarding durability. Lastly, the anti-microbial function of these coatings needs further investigation as evidenced by the high potential of natural lipid molecules to interact with bacterial cell walls and kill bacteria in nature [111, 152-154].

3.5. Conclusions

In this study, we develop two methods to achieve hydrophobicity or superhydrophobicity using liquid phase deposition of naturally derived cinnamic or myristic acid. Through detailed studies of the deposition concentration, time, and temperature, we developed an optimum deposition method for smooth metal oxide and metal oxide micro/nanostructures. Superhydrophobic copper oxide nanostructured surfaces were shown to achieve apparent advancing contact angles as high as 154° and 165° for cinnamic and myristic acid, respectively with low contact angle hysteresis (< 15°). Comparison with previously used acid treatments reveals that the coatings developed here have the one of the highest degrees of hydrophobicity for non-organosilane and non-perfluorinated coatings. This study presents a novel avenue for safer and more environmentally friendly fabrication of superhydrophobic surfaces for energy and water applications.

CHAPTER 4: WETTABILITY OF RARE EARTH OXIDES: A TALE OF HYDROCARBON ADSORPTION*

4.1. Introduction

Scientific knowledge is built on debates and challenges formed by competing hypotheses. In this chapter, we study the wettability of rare earth oxides (REO), a topic of argument over the last decade by numerous researchers. Interestingly, similar debates have been had regarding the wettability of noble metals, questioning whether they are intrinsically hydrophilic[157-158] or hydrophobic[159].

During the early twentieth century, for approximately fifty years, scientists had reported controversial results indicating that the wettability of gold is either intrinsically hydrophobic[159] or hydrophilic[157-158]. After all experimental and theoretical studies, researchers could measure in-situ contact angles under UHV conditions after the gold layer was deposited on a substrate. The wettability measurements and surface chemistry analyses concluded the noble metals such as gold or platinum are inherently hydrophilic but exhibit acquired hydrophobicity due to contaminants from the air. Contaminants from the atmosphere generally consist of organic materials; what we call volatile organic compounds (VOC). Clean metallic surfaces with high surface energy (~ 10^3 mN/m) show a high affinity to VOC's which have very low surface energy (~ $2\text{-}3\times10^2$ mN/m), adsorbing them on the surface to lower their overall surface free energy.

* This study is currently in preparation for the publication as of the date of the deposition of this dissertation. Junho Oh conducted the experiments, analyzed the data and wrote the manuscript under the advisement of Dr. Nenad Miljkovic. Junho Oh is the first author of the research paper being prepared.

Rare earth oxides are an oxide of the rare earth elements (REE), which mainly refer to lanthanides. Lanthanides (atomic number from 57 to 71) are metallic elements in economically-limited availability on the earth. Due to their scarcity, lanthanides are commonly called rare earth elements, which include scandium (Sc) and yttrium (Y). Rare earth elements have been widely utilized for the manufacture of catalysts[160-163], magnets[161, 164], and electronics[161, 165].

The intrinsic non-wetting nature of rare earth oxides was first reported in 2013. Azimi et al. reported their hypothesis and observations on intrinsic hydrophobicity of REO[166]. The study suggested REO's are intrinsically hydrophobic due to REO's electron configurations having octet outer shell in 5s2p6 orbitals, resulting in the non-polarity of surfaces led to intrinsic hydrophobicity. They measured the contact angle and polarity of pelletized REO surfaces to prove the hypothesis. The study also reported the mechanical and thermal durability of hydrophobicity against abrasion and higher temperature condition up to 1000°C. On the other hand, Preston et al. suggested opposite hypothesis REO's are intrinsically hydrophilic but exhibiting hydrophobicity due to airborne hydrocarbon adsorption on the surface analogous to gold[167]. The study showed over-time contact angle measurements, and X-ray photoelectron spectroscopy (XPS) on holmium oxide (Ho_2O_3) and cerium oxide (CeO_2) exposed to laboratory air. The study reported a contact angle increase over time paralleled to surface atomic carbon content increase as the surfaces adsorb hydrocarbons from the air. Khan et al. then attempted to strengthen Azimi et al.'s hypothesis of intrinsic hydrophobicity from study insisting carbon contents on oxide surfaces were irrelevant to wettability[168]. The researchers showed an increase in contact angle on cerium oxide surface as O/Ce ratio decreased but surface carbon contents remained the same in ultra-high vacuum (UHV) condition.

After these studies initiated interesting debates on the wettability of REO's, other studies had been conducted or followed up to figure out what makes rare earth oxide surfaces hydrophobic. Some studies attempted to find evidence from computational methods such as molecular dynamic (MD) simulations. Carchini et al. performed simulation based on density functional theory (DFT) method to explain intrinsic hydrophobicity of REO's (CeO_2 and Nd_2O_3) due to dissociation of interfacial ice layer compared to alumina[169]. The study also showed surface termination with hydroxyl group formed by lattice oxygen ($O_{lat}H$) can convert the surface from hydrophobic to hydrophilic. Fronzi et al. also utilized DFT method to show that oxygen terminated cerium oxide surface (1 0 0) is unstable. Thus the surface tends to be dominated by lower index configuration (1 1 1)[170]. The simulation results suggested the wettability of cerium oxide may vary from hydrophilic to hydrophobic by surface atomic orientations.

More recently, on the other hand, experimental studies are reported supporting VOC adsorption effects on hydrophobicity than oxidation state or unique electron configurations of REO. Külah et al. reported a contact angle increase of REO and RE-nitrides from VOC adsorption over periods of time[171]. The results suggested hydrophobicity of Gd2O3 and CeO_2 was caused by VOC adsorption from the air, especially promoted by thick tetracene layer (~2 nm). The researchers also reported the dissolution of REO film and fluorine adsorbed on the surface in water and adsorption of nitrogen in the air forming REO-nitride. Lundy et al. conducted experiments at controlled adsorption condition with nonane (C_9H_{20}), showing the transition of wettability does not affected by the different oxidation state of cerium oxide (Ce(III) and Ce(IV)) but affected by the adsorption of the hydrocarbon from surface analysis[172]. The researchers also reported thermal annealing with the nonane adsorbed sample in Ar atmosphere at 900°C to dehydroxylate and achieve better

conformality in surface chemistry. After thermal annealing, advancing contact angles of REO surfaces were slightly decreased as receding contact angles were increased.

Aside from the debate on the truth of REO's hydrophobicity during the last decade, many researchers have endeavored to utilize the hydrophobicity of REO's developing novel and durable coating methods. Oh et al. utilized atomic layer deposition (ALD) to deposit thin film (~ 50 nm) of Er_2O_3, Dy_2O_3, La_2O_3, CeO_2 and Y_2O_3 on Si (1 0 0) wafer and Si nanowires[173]. The study focused on the fabrication of thin film of REO's and thermally stable thin REO coatings based on the assumption of intrinsic hydrophobicity. A recent study reported the development of superhydrophobic coating using solution precursor plasma spray (SPPS) method with Ytterbium oxide (Yb_2O_3). The authors initially reported the coating was thermally-stable due to intrinsic hydrophobicity[174]. However, in their follow-up study, the authors examined the chemical composition of SPPS coatings in detail showing deposition of hydrocarbon in plasma flame, which brought hydrophobicity of the surface[175-176].

In this study, we investigated wettability of rare earth oxides and other metallic oxides for comparison, to fundamentally prove the hydrophobicity of REO is governed by hydrocarbon adsorption from airborne volatile organic compounds (VOC) analogously with the hydrophobicity of gold and other metals. To provide the evidence, we designed and performed sets of experiments and surface analyses showing that the chemisorption of hydrocarbon occurs on the surface, which further promotes physisorption as well. We then correlated the surface chemistry analysis results in the transition of wettability from hydrophilic to hydrophobic.

4.2. Experimental Methods

4.2.1. Surface Preparation and Cleaning

We used 1 in diameter sputter targets as sample acquired from K.J. Lesker (See Appendix for detailed specification of sputter targets used.). We decided to use sputter targets to use more conformal and bulk material with known purity. Contact angle measurements and surface analyses were conducted upon the breakage of the original Ar sealing and solvent cleaning. We also sputtered cerium oxide (CeO_2), erbium oxide (Er_2O_3) and ytterbium oxide (Yb_2O_3) as rare earth oxide, and niobium oxide (Nb_2O_5) as a transition metal oxide on Si wafers with 10 nm thickness, to get rid of random surface roughness and porosity of sputter targets. The sputter targets have random roughness and porosity from the manufacturing process by sintering. We used AJA ORION 3 sputtering system (AJA International Inc., United States) and ST20 ORION magnetron gun, with RF plasma maximum powered at 40-60 W ramped up and down at the rate of 20 W/min to prevent excessive thermal stress for the sputtering targets. The deposition rate was 0.05-0.07 Å/min.

We utilized a plasma cleaner (PDC-001, Harrick Plasma, USA) and air as a process gas for plasma cleaning. We conducted solvent cleaning by sonicating the surface in a bath of acetone for 10 minutes and washing the surface with isopropyl alcohol (IPA) and DI water, followed by another IPA wash and N_2 dry.

4.2.2. Contact Angle Measurements

Contact angle on the sample surface was measured using a microgoniometer (MCA-3, Kyowa Interface Science, Japan, equipped at the University of Illinois). Both advancing and receding contact angles were measured on a surface. We measured advancing contact angle while droplets

were depositing from piezoelectric microdroplet injector at a rate of 50-90 droplets/sec and measured receding contact angle while the deposited droplet evaporating without incoming volume. The contact angle measurements were analyzed by image processing using a software (FAMAS, interFAce Measurement & Analysis System) provided by the instrument manufacturer.

4.2.3. X-ray Photoelectron Spectroscopy (XPS)

X-ray Photoelectron Spectroscopy (XPS) was performed to determine the chemistry of surfaces. Kratos Axis ULTRA instrument (Kratos Analytical, Ltd., UK, commissioned at the University of Illinois at Urbana-Champaign, IL, USA) was used at grazing (15°) and normal takeoff angles, and ULVAC (commissioned at Kyushu University, Fukuoka, Japan). We analyzed XPS spectra using CasaXPS software (Casa Software, UK).

4.2.4. Time-of-Flight Secondary Ion Mass Spectroscopy (ToF-SIMS)

Time-of-Flight Secondary Ion Mass Spectroscopy (ToF-SIMS) were performed to analyze the chemical species adsorbed on the surface in detail using PHI Trift III (PHI, Japan). We conducted surface analysis and depth profiling to examine how surface chemistry is different on the surface. We used Au primary liquid metal ion gun (LMIG) for both positive and negative secondary ions detection at bunched mode for surface analysis. Cs+ ion gun was used for depth profiling for negative ions considering the ions we would like to detect such as REE, oxygen, and carbons. The suppressor voltage and emission currents were 10 kV and 10 nA, respectively. The scanning area was 100 μm × 100 μm for surface analysis and 800 μm × 800 μm for surface analysis. The data were analyzed using WinCadence.

4.2.5. Thermogravimetric Analysis (TGA)

To study adsorption dynamics and measure the amount of hydrocarbon adsorbed on the surface over time, we conducted thermogravimetric analysis (TGA) with rare earth oxide powders. We obtained samples from Sigma-Aldrich. We conducted measurements using TGA 50 (TA Instruments) up to 500°C at 10°C/min of a heating rate.

4.2.6. Atomic Force Microscopy (AFM)

We investigated the change in surface energy on the sample surfaces by hydrocarbon adsorption using atomic force microscopy (AFM). We obtained the force curve data and force mapping on fresh and hydrocarbon adsorbed rare earth oxides using Asylum Research MFP-3D (Asylum Research, United States) atomic force microscope in contact mode. We utilized diamond-like-carbon (DLC) coated contact mode AFM tip (ContDLC, BudgetSensors) and colloidal tips (), and the mapping area was approximately 25 μm × 25 μm. In addition, we also conducted tapping mode AFM over-time topology measurements to examine possible topological variation due to gas phase adsorption. We used a tapping mode AFM tip (AL300-G, BudgetSensors), and scan area was 10 μm × 10 μm. The AFM data were analyzed using IgorPro (Asylum Research, United States) and open-source software called Gwyddion[87].

4.3. Results

4.3.1. Wettability Transition: Hydrophilic to Hydrophobic

We established the experimental sequences for a surface to adsorb hydrocarbon from the air and to conduct wettability and chemical analysis. First, we measured the contact angle of the sputtering target upon breakage of the Ar seal to minimize possible contamination and adsorption. We left the surfaces exposed to the laboratory air and contact angle was measured at each time of

measurement up to 600 hours in Urbana, Illinois, United States (40°06′N, 88°13′W). We tested the air quality with VOC meter resulted in approximately 20 ppm.

Figure 4-1a shows the advancing contact angle measured on the sputter targets after breakage of seal and solvent cleaning. We chose CeO_2, Er_2O_3 and Yb_2O_3 as REO and Nb_2O_5, Cu and SiO_2 as a comparison group. We measured the contact angle at the breakage of Ar sealing. Upon exposure to the indoor air after the breakage of the seal, advancing contact angles increased over time, more rapidly in the initial 24 hours and gradually stabilized at a certain angle after 100 hours. Unlike other samples, contact angle on Er_2O_3 surface was unmeasurable (0°) because a small volume of droplets was completely soaked due to the original porosity of the sample. After 600 hours of exposures, we cleaned the surface with solvents and DI water to clean the surface. After the solvent cleaning, the contact angle on the surfaces was slightly decreased. Figure 4-1b shows the advancing contact angle measured after solvent cleaning, where we found out that solvent cleaning could not effectively clean the contaminants. After further exposure to the air after the cleaning, like initial exposure to the air, as shown in Fig. 4-1a, the advancing contact angle of copper increased to $\theta^{a}_{adv,Cu}$=115.8 ± 22°, followed by cerium oxide ($\theta^{a}_{adv,CeO2}$=104.8 ± 6.9°) and ytterbium oxide ($\theta^{a}_{adv,Yb2O3}$=83.3 ± 2.5°). We then cleaned the surface with plasma at high power (45 W) for 1 minute, and all the surfaces became superhydrophilic (θ^{a}_{adv}=0°). The surfaces were left exposed to the air for another 600 hours. After the exposure, the advancing contact angle was not recovered fully, but it recovered approximately 70-80% and was in an increasing trend.

To find out what caused the wettability transition on the surfaces, we conducted XPS analyses on the surface. Figure 4-1c and 4-1d show the entire XPS spectra of CeO_2 and Cu after plasma cleaning and 100 hours of exposure in the air. On both surfaces, atomic contents of carbon approximately 3 to 10 times increased compared to the surface before the exposure to the air. Note,

even though we attempted to minimize the time between cleaning and XPS measurements, detection of carbon peaks was inevitable from the cleaned surfaces considering the gas adsorption to the surface is a spontaneous process. Rare earth oxides are known to be reduced in ambient conditions[177]; however, we saw the spectra of CeO_2 (875-925 eV) did not change indicating the oxidation state of the surface remains the same as Ce(IV)[178]. Correlating the contact angle measurements and surface chemistry analyses using XPS, we could verify the wettability transition of REO derived by hydrocarbon adsorption, rather the surface polarity given by the oxidation states as reported in the previous study[146]. However, we needed to acquire stronger evidence of the relations between hydrocarbon adsorption and surface wettability.

For example, as discussed earlier on Er_2O_3 surface, the contact angle was not measurable because the sputter target has random roughness and porosity derived from the manufacturing process by sintering. To rule out the effects on roughness and porosity of a surface on contact angle measured, we deposited rare earth oxides with a very slow deposition rate (<0.05 Å/min) up to 10 nm on a silicon wafer (test grade, [1 0 0], University Wafer, United States) to fabricate conformal film on a flat surface.

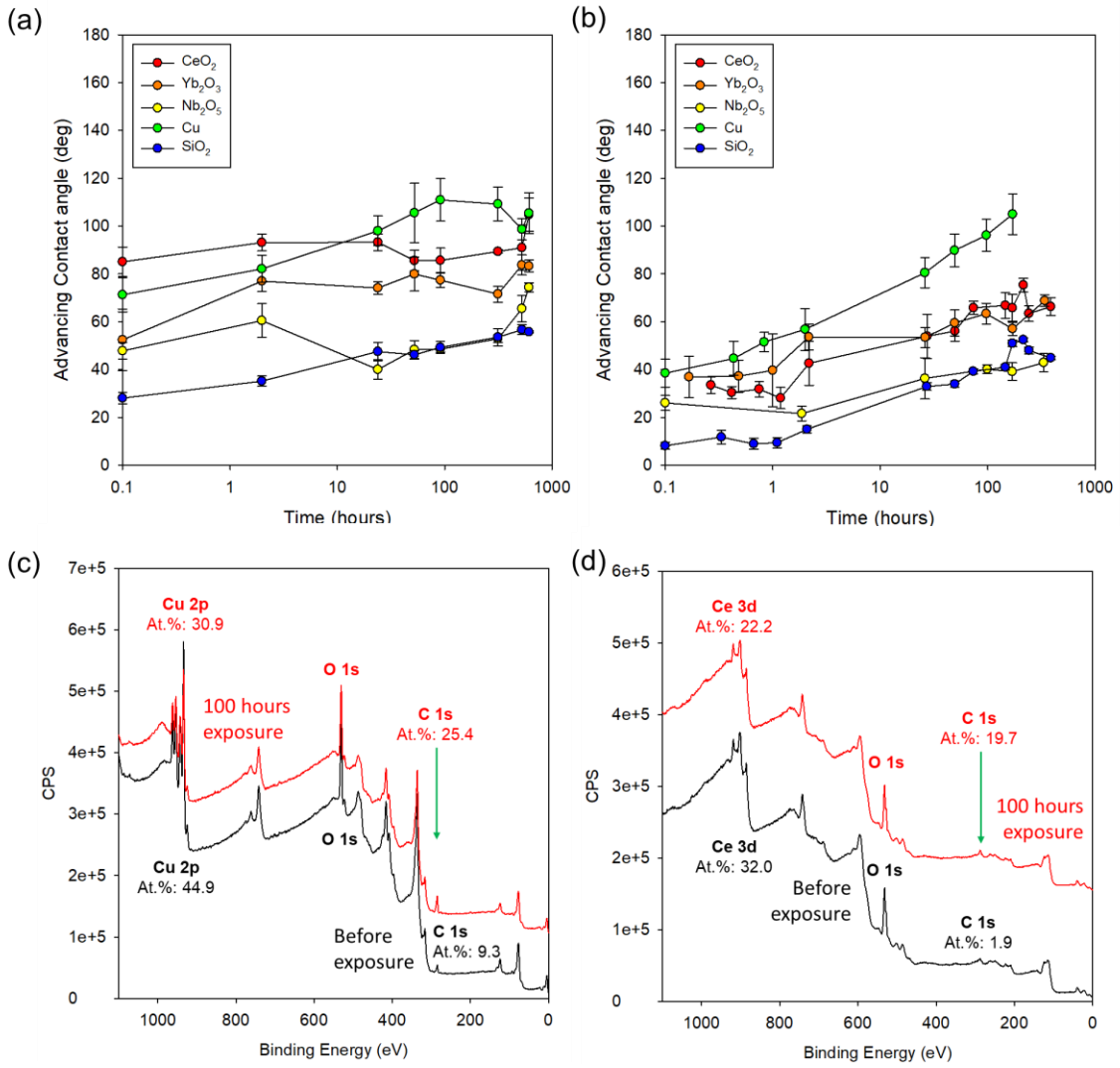

Figure 4-1 Advancing contact angle on rare earth oxide (REO) and other metallic surfaces measured over time (a) exposed to air up to 600 hours after breakage of seal and solvent cleaning and (b) exposed to air up to 600 hours after plasma cleaning in Urbana, IL, USA. Entire X-ray photoelectron spectroscopy (XPS) spectra of (c) CeO2 and (d) Cu before exposure and after 100 hours of exposures.

Figure 4-2 describes the advancing and receding contact angle measurements on the sputtered sample exposed to the air up to 1000 hours, and XPS analyses for entire spectra and high-resolution narrow-band spectra for C 1s, O 1s, and Ce 3d. Increases in contact angle upon exposure were in a similar trend with the sputtered target. Advancing contact angle increases on REO (CeO_2, Er_2O_3 and Yb_2O_3) surfaces were noticeably similar over time and became saturated approximately at 95° after 250 hours. Receding contact angle was also increased over time, but it fluctuated more randomly and delayed compared to the steady increase of advancing contact angle. Entire and detailed XPS spectra in Fig. 4-2c clearly illustrates the increase of hydrocarbon coverage on the surface. Table 4-1 summarizes the atomic percentage of elements from entire spectra showing carbon content was increasing while Ce 3d:O 1s ratio was in a reasonable range as approximately 2. As the exposure time increased, Ce 3d and C 1s detailed peak did not change while O-C=O to Ce-O peak high ratio noticeably increased from 0.25 to 0.55. This result proves the increased coverage of hydrocarbon on the surface.

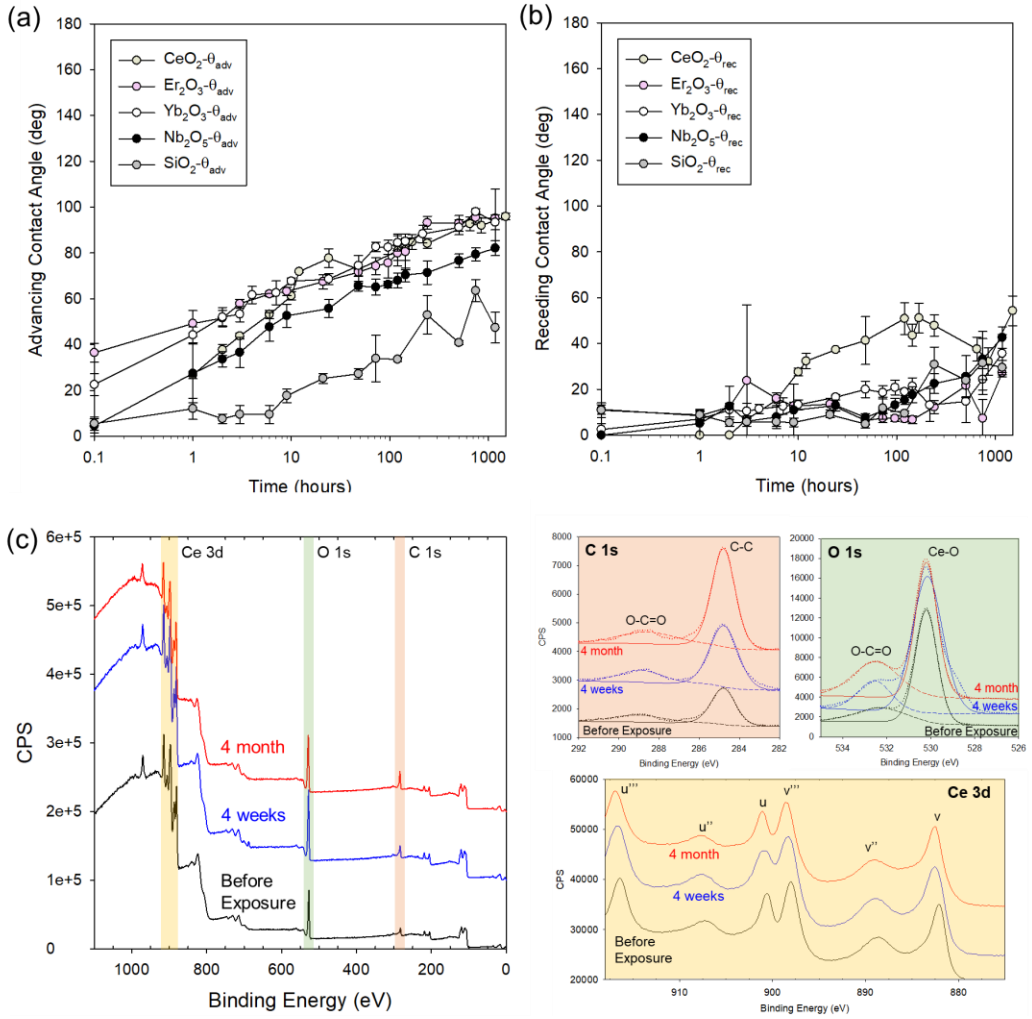

Figure 4-2 (a) Advancing and (b) receding contact angle on CeO_2, Er_2O_3, Yb_2O_3, Nb_2O_5 thin film surfaces deposited on the silicon wafer and Si wafer as the controlled sample. The surfaces left exposed to the indoor air up to 1000 hours for contact angle measurements. (c) X-ray photoelectron spectroscopy (XPS) entire spectra and C 1s, O 1s, and Ce 3d narrow-band high-resolution spectra showing that oxidation state of Ce did not change and carbon contents on the surface increased over time.

Table 4-1 Atomic percentage of Ce, C, and O and detailed spectral analyses of Ce 3d, C 1s and O 1s from X-ray photoelectron spectroscopy (XPS) on CeO_2 surfaces before and after exposure.

Condition	Before exposure			4 weeks of exposure			4 months of exposure		
Elements	Ce 3d	C 1s	O 1s	Ce 3d	C 1s	O 1s	Ce 3d	C 1s	O 1s
At. %	27.56	21.02	51.41	20.54	26.94	52.52	20.17	38.21	41.62
Detailed Peak analyses	C 1s	C-C 70.99	O-C=O 29.01	C 1s	C-C 76.55	O-C=O 23.45	C 1s	C-C 70.99	O-C=O 29.01
	O 1s	Ce-O 79.1	O-C=O 20.9	O 1s	Ce-O 80.66	O-C=O 19.34	O 1s	Ce-O 64.49	O-C=O 35.51

Atmospheric adsorption experiments and surface analyses could tell us the hydrocarbon adsorption indeed affects the wettability of rare earth oxide. However, the results cannot strongly support and reveal whether the hydrocarbon was physically or chemically adsorbed on the surface. To understand the phenomena more precisely, we conducted additional experiments using light hydrocarbons such as alkanes (from hexane (C_6H_{12}) to decane ($C_{10}H_{22}$)) which is similar with volatile organic compounds (VOC) in the indoor and outdoor air. We placed the CeO_2 sputtered and pristine Si wafer in an enclosure with saturated hydrocarbon atmosphere at room temperature and repeated the same experimental protocols for contact angle measurements and surface analyses.

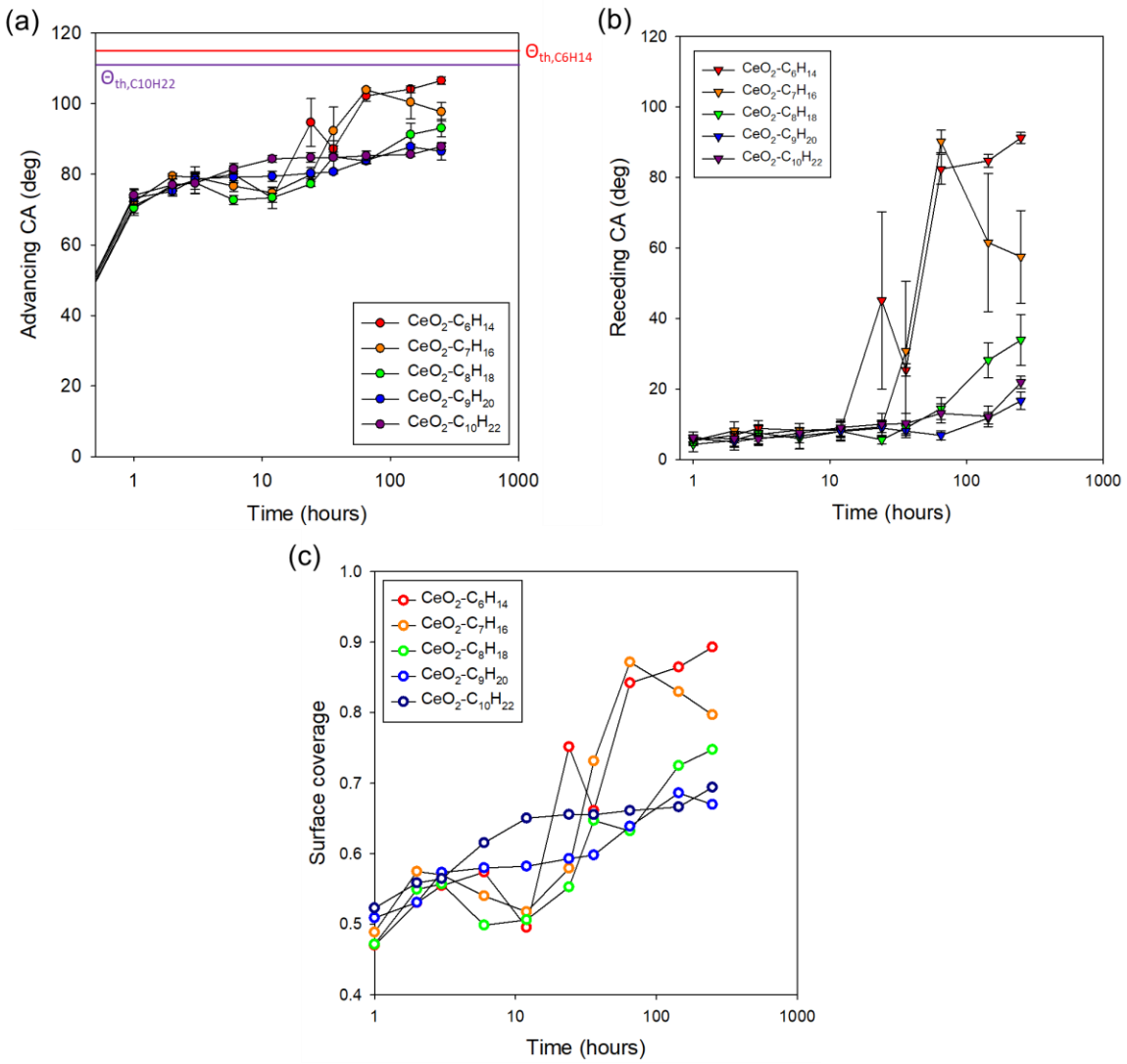

Figure 4-3 (a) Advancing and (b) receding contact angle on CeO_2 surfaces left exposed in a saturated hydrocarbon (C_6H_{14} to $C_{10}H_{22}$) atmosphere. The line on (a) indicates calculated maximum contact angle on a flat surface with homogeneous alkane chemistry. (c) Surface coverage calculated using the maximum contact angle.

Figure 4-3 shows the advancing and receding contact angle on CeO_2 surfaces adsorbed the alkanes over 1000 hours. After the film deposition of Si wafer, the fresh CeO_2 surface was superhydrophilic ($\theta^{a}_{\mathrm{adv}}$=30° and $\theta^{a}_{\mathrm{rec}}$=0°). From the advancing contact angle, we calculated the surface coverage to examine how the surface adsorbed hydrocarbons conformally characterized by the wettability. We first calculated the theoretical maximum contact angle on hydrocarbons by assuming the solid surface were entirely covered with hydrocarbons and calculated contact angle using the Young-Dupre equation as follows in Eq. 4-1. The interfacial surface energy of hydrocarbons with water and the air were summarized in Table 4-2.

$$\cos\theta = \frac{\gamma_{sl}-\gamma_{sv}}{\gamma_{lv}} \quad \text{(Eq. 4-1)}$$

$$\varphi_{t=t1} = \left(\frac{cos\theta_{t=t1}}{cos\theta_{t=0}}\right) / \left(\frac{cos\theta_{th}}{cos\theta_{t=0}}\right) \quad \text{(Eq. 4-2)}$$

The surface coverage was then calculated from the theoretical maximum contact angle and advancing contact angle measured. Figure 4-3c shows the surface coverage φ of CeO_2 surfaces calculated from Eq. 4-2 using advancing contact angles. During the exposure, surface coverage tends to increase over time but after a certain period of time, the increase became gradual as saturated. Interestingly, at an early stage, surface coverage in heavier hydrocarbons such as nonane (C_9H_{20}) or decane ($C_{10}H_{22}$) was higher than the ones in lighter hydrocarbon atmosphere, which was against our assumption.

We assumed that surfaces with lighter hydrocarbons would display higher surface coverage because of their lower surface energy and higher vapor pressure. However, this trend lasted only for approximately the initial 24 hours when the contact angle of surfaces with lighter hydrocarbons rapidly increased. More interestingly, the receding contact angle in Fig. 4-3a started to rapidly

increase at the same time when the trend turned around. This seems to be driven by the difference in the adsorption dynamics of hydrocarbons. Previous studies regarding the sticking coefficient of alkanes on Au or Pt surfaces have shown that the sticking coefficient of alkanes lighter than octane (C_8H_{18}) are nearly zero[179]. These results illustrate physisorption is dominating surface adsorption behavior at the very early stage. However, after 24 hours, it seemed to be believed that the adsorption dynamics changed from a rapid increase in surface coverage and contact angle for surfaces adsorbed lighter hydrocarbons. The question regarding the adsorption mechanism will be further discussed in detail the following section.

T**able 4-2.** Surface tension of n-alkanes with air and interfacial tension of n-alkanes and water at 22°C. *Calculated maximum* water contact angle *on* alkane adsorbed surfaces was calculated based on Eq. 4-1.

Parameters	C_6H_{14}	C_7H_{16}	C_8H_{18}	C_9H_{20}	$C_{10}H_{22}$
$\gamma_{CxHy-air}$ [mN/m]	18.3	20.05	21.55	22.7	23.7
$\gamma_{CxHy-water}$ [mN/m]	51.4	51.9	52.5	52.4	53.2
$\theta_{th-CxHy}$ [mN/m]	117.0	115.9	115.2	114.1	113.9
$P_{sat@25°C}$ [kPa]	17	4.6	1.33	0.59	0.17

In the previous study, Kulah et al reported the topological change in nanoscale height when the surface was covered with several nanometers of cyclic hydrocarbon (tetracene, $C_{18}H_{12}$)[171] []. We conducted AFM measurements to understand topological and surface adhesion change upon hydrocarbon adsorption. We conducted tapping mode AFM measurements for topology measurements and contact mode for surface adhesion force mapping. Figure 4 shows the AFM topological microscopic image of 5 µm by 5 µm area and the spatial resolution of the scan was ~10 nm, similar to tip radius (8-10 nm). To ensure the original surface topology and chemistry similar, we fabricated a sample surface with a numbered marker using photolithography to scan the same area every time or very close vicinity of the scanned area. The scanned results in Fig. 4-4a and 4b showed that the change in the topological roughness due to hydrocarbon adsorption is not significant. The RMS roughness value over the scanned area was 1.83 nm for a sample before exposure and 1.48 nm for 2 weeks aged samples in C_6H_{14} environments.

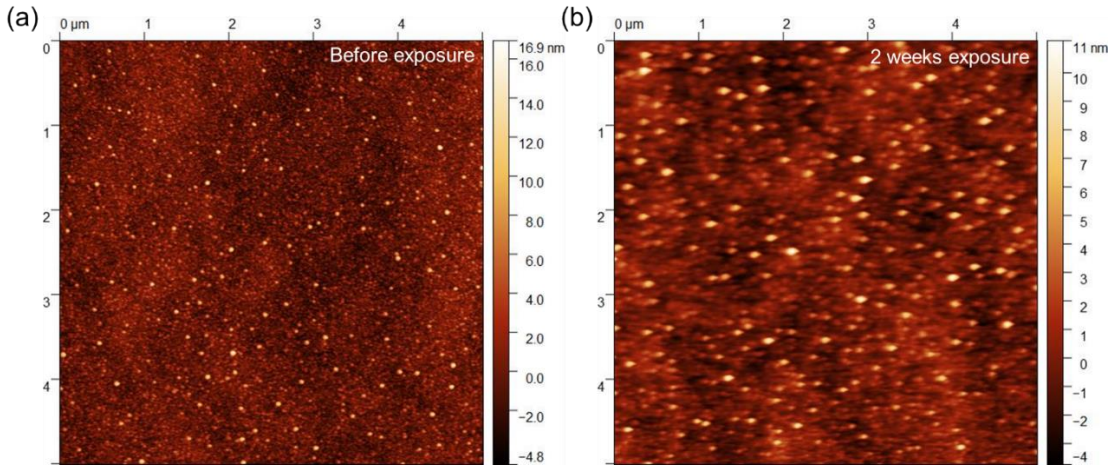

Figure 4-4 Atomic force microscope (AFM) image of CeO2 thin film deposited on Si wafer (a) before exposure and (b) after 2 weeks of exposure in a hexane saturated atmosphere. The scan area was 5 µm × 5 µm.

4.3.2. Hydrocarbon Adsorption: Chemisorption vs. Physisorption

From our experimental results, we could correlate hydrocarbon adsorption on the surface and wettability transition from hydrophilic to hydrophobic. However, we need stronger evidence on surface chemistry to completely reveal what governs the wettability transition of REO. To fully understand the hydrocarbon adsorption behavior, we conducted rigorous surface chemistry analyses on the same CeO_2 surface adsorbed known alkanes that we used in the earlier experiments. We compared the surface with a freshly deposited CeO_2 surface and plasma cleaned surface.

Figure 4-5 and Table 4-3 describe the surface chemistry of CeO_2 surface obtained from XPS and ToF-SIMS. Figure 4-5a and 4-5b,c shows the entire and narrow-band XPS spectra for a newly deposited or plasma cleaned CeO_2 sample with lesser hydrocarbon adsorbed and for CeO_2 surfaces adsorbed hydrocarbon in the controlled alkane atmosphere. According to Ce 3d spectra in Fig. 4-5b and the composition provided in Table 3, we can confirm the oxidation state of ceria remained as Ce(IV) during the exposure and plasma cleaning. While maintaining the oxidation state, the surfaces exposed to the saturated alkane atmosphere adsorbed hydrocarbon, increasing atomic carbon contents. Note, newly fabricated CeO_2 surface and plasma cleaned surface also adsorbed VOC from the air before loaded in a high vacuum chamber displaying the presence of carbon on the surface. We can confirm this from C 1s XPS spectra of the surfaces for C-C (284.8 eV) and C-O (288.6 eV) peaks. For alkane adsorbed surfaces, C-C (284.8 eV) bonding contributed 90% of carbon contents on the surface because the majority of adsorbed gas molecules only has carbon and hydrogen. This trend proves the hydrocarbon adsorption from atmosphere governs the surface chemistry. Even though XPS results indicate the presence of hydrocarbons and chemical bonding

between elements, they cannot provide clear evidence regarding what kind of molecules are on the surface and how they are adsorbed on the surface.

ToF-SIMS results further support the adsorption of organic compounds and suggest more detailed explanations for chemical species on the surface. According to Fig 5c,d and Table 3, the surface adsorbed lighter hydrocarbons (C_6H_{14}) showed higher counts of CxHy secondary ions compared to the C_9H_{20} adsorbed surface. The higher contact angles and surface coverage of lighter hydrocarbon adsorbed surfaces have shown throughout this study. This is because lighter alkanes have a 10-20 % lower surface tension and higher vapor pressure caused higher surface coverage. Negative ions showed a similar trend showing the ratio between O- and OH- ions were in decreasing trend as contact angle and surface coverage decreases.

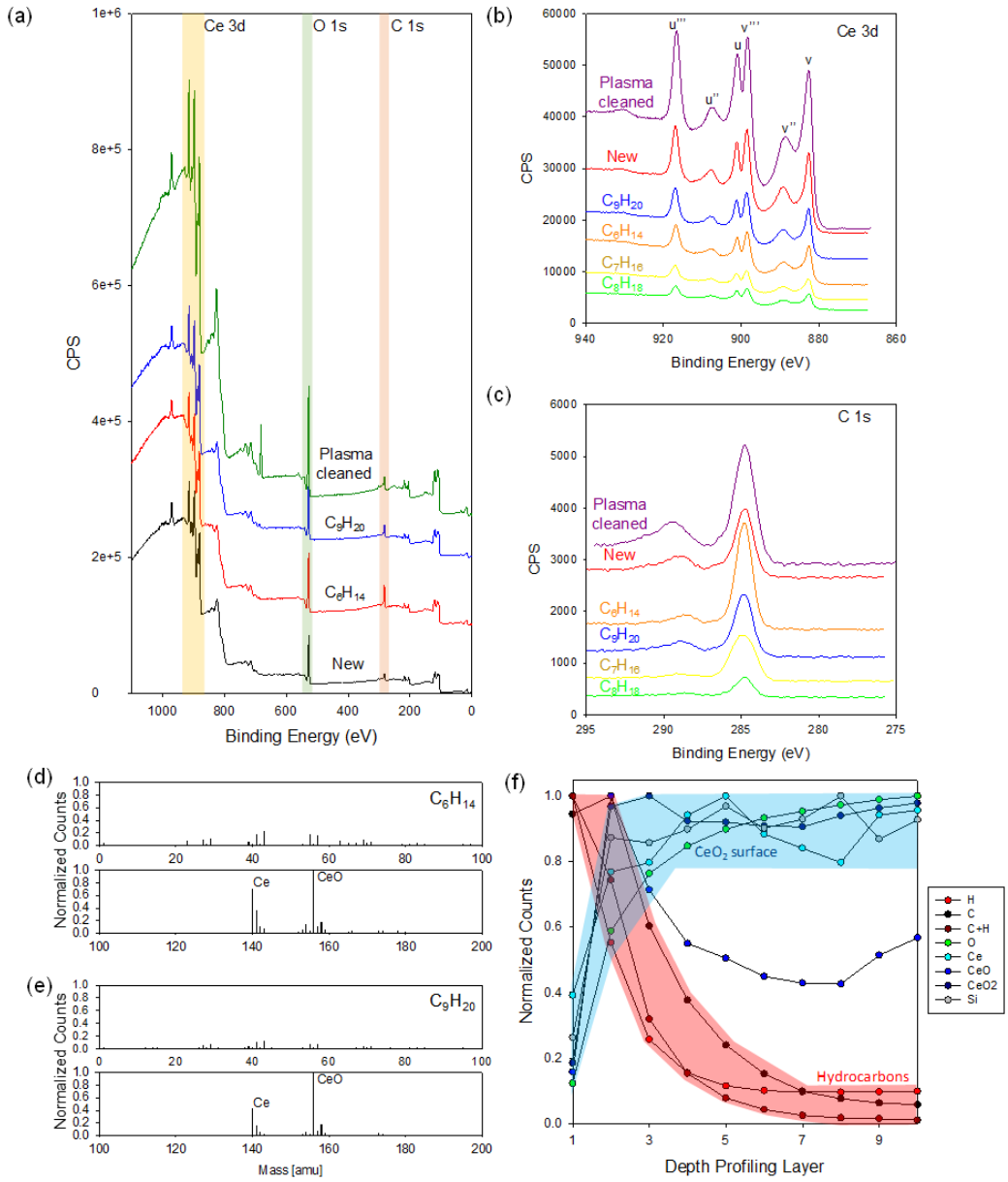

Figure 4-5 The surface chemistry analyses using X-ray photoelectron spectroscopy (XPS) and Time-of-Flight secondary ion mass spectroscopy (ToF-SIMS) on CeO_2 surfaces. (a) Entire XPS spectra of newly deposited CeO2 thin film surface, hexane and nonane adsorbed CeO2 surfaces and plasma cleaned surface after the hydrocarbon adsorption. XPS narrow-band high-resolution spectra were also obtained for (b) Ce 3d and (c) C 1s to verify the oxidation state and hydrocarbon adsorption of CeO_2 upon hydrocarbon exposure. ToF-SIMS results of (d) hexane (C_6H_{14}) and (e) nonane (C_9H_{20}) adsorbed surface, normalized by CeO (156 amu) ion count, and (f) depth profile of the secondary ions detected from hydrocarbon and CeO2 surface.

We also conducted the depth profile on a CeO_2 surface adsorbed hexane (C_6H_{14}), presented in Fig. 4-5f. We sputtered the surface with Cs^+ ion for a second, collected and analyzed the data for 52 sec. The depth profile of secondary ions clearly represented the adsorbed hydrocarbon layer was superficial as the C, H and C+H ion counts decreased significantly after several initial layers. On the other hand, ions from the constituent of cerium oxide surfaces such as Ce, O, CeO and CeO_2 were increasing as hydrocarbon layers were sputtered out from the surface by the primary Cs^+ ion. From the contact angle measurements and surface analyses, we have proved the hydrocarbons adsorbed on the surface govern the surface wettability. However, a question remains unanswered regarding how the hydrocarbon adsorbs to the surface, either physical adsorption by intermolecular attraction or chemical adsorption by forming a chemical bond with the surfaces. To better understand the adsorption phenomena and address the question, we designed and conducted experiments to isolate physisorbed hydrocarbon from the surface. We first cleaned the surface which was at the saturated adsorption state with different methods and intensity. We then repeated the same hydrocarbon adsorption experiments in a controlled alkane environment and measured contact angles to examine there was different adsorption behavior.

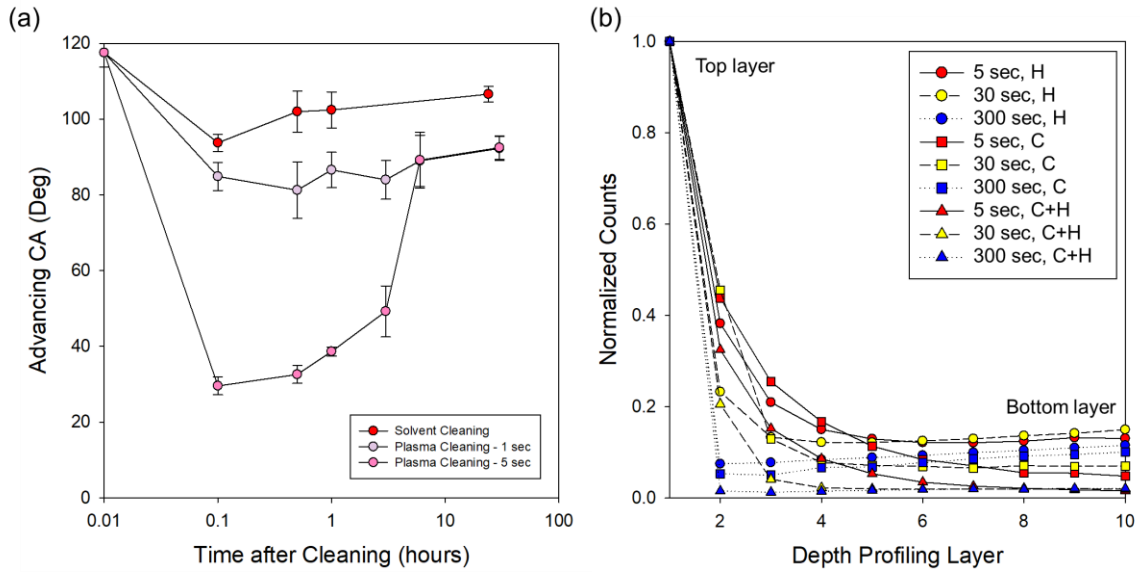

Figure 4-6 (a) Advancing contact angle measured on CeO_2 surface after solvent and plasma cleaning with a different dose. For detailed cleaning methods, please refer to the experimental section. The advancing contact angle was recovered in a short time frame compared to pristine CeO_2 surface. (b) Normalized secondary ion counts for hydrogen (H), carbon (C) and hydrogen-carbon (C+H) ion obtained from Time-of-Flight Secondary Ion Mass Spectroscopy (ToF-SIMS) depth profiling on surfaces cleaned with a different plasma dose.

We cleaned hexane saturated CeO_2 thin film (~10 nm) surface for 1, 5 and 30 seconds at the lowest power of plasma (15 W). Figure 4-6 shows the contact angle measured after 1, 5 and 30 seconds of plasma cleaning and the surface chemistry on the surface. As the plasma dose varied, the contact angle decreased as the adsorbed hydrocarbon being removed to a different extent from the surface. Even with the lower power of plasma (15 W) for 30 seconds, the contact angle of a cerium oxide surface was decreased from 117.5 ± 3.8° to 0° as complete wetting. The contact angle of surface cleaned for 1 and 5 seconds were 84.8 ± 3.7° and 29.6 ± 2.4°, respectively. ToF-SIMS depth profile in Fig. 4-5b support the effectivity of cleaning with different doses of plasma. Ion count of each depth profiling layer was normalized by the first layer ion counts considering the hydrocarbon concentration would be the maximum at the top surface layer. The cleaned surface then left exposed to the lab air to examine if there is any difference in hydrocarbon adsorption dynamics according to the difference in surface chemistry. We measured the contact angle increase over time after the surface being cleaned by different methods and intensity. From these results, we found out solvent cleaning with sonication could not effectively remove the hydrocarbons from the surface compared to plasma cleaning. Interestingly, we could observe very fast contact angle recovery after cleaning from Fig. 4-6a compared to the CeO_2 contact angle increase over time provided in Fig. 4-2a (airborne VOC) or 3a (C_6H_{14}) on a freshly prepared surface. The solvent cleaned surface then quickly recovered its contact angle during very short periods of time (~30 min). The wettability of surfaces cleaned with low-dose plasma recovered relatively slower (~3-6 hours) than solvent cleaned surfaces, but the recovery was remarkably fast compared to the pristine surface or the surface cleaned with very high dose.

The results suggest the adhesion of adsorbed hydrocarbon molecules are based on both chemisorption and physisorption not only on physisorption. This can be explained from the

analogy with self-assembled monolayer (SAM) coatings. One of the most frequently used superhydrophobic coatings is based on fluorosilanes using chemical vapor deposition (CVD)[180]. The organosilane form a chemical bonding with surfaces from its own silanol group and hydroxyl group on the surface during the CVD process. The silanol bonding can be decomposed from the surface during plasma cleaning[181] and the coated surface will lose its hydrophobicity. However, the silane coating is chemically durable against solvents like acetone and IPA[182].

Similarly, the hydrocarbon-free REO surface in the pristine condition are superhydrophilic. After adsorption of VOC's, the REO surface becomes hydrophobic due to the adsorbed hydrocarbons. Meanwhile, solvents can only dissolve physisorbed hydrocarbon molecules since chemisorbed molecules are strongly attached to the surface by chemical bonding. Thus, the solvent cleaning will leave the chemisorbed hydrocarbons on the surface. Subsequently, the surface terminated with chemisorbed hydrocarbons can further accelerate physisorption of organic compounds much faster than the hydrocarbon-free surface. Contact angle measurements approve this statement considering the solvent cleaned surface became 84.8 ± 3.7° and increased to 101.9 ± 4.7° in 30 minutes when plasma cleaned with high dose (5 min at 45 W) surface took in 30 days to fully recover the wettability before cleaning.

Considering we cleaned the surfaces with acetone IPA and DI water with sonication, just before (~10 min) they are loaded in high vacuum condition of ToF-SIMS chamber, majority of physisorbed hydrocarbon molecules should be dissolved away. Therefore, if most of hydrogen molecules are physisorbed, CxHy ions should not follow a similar trend with the surface coverage. In addition, as the difference in the contact angle of plasma and solvent cleaned surface suggested, the chemisorbed hydrocarbons remain on the surface by bonding with oxygen vacancies and free radicals. This led to an increase in $CxHy^+$ ions and OH^- ions to be detected from ToF-SIMS results.

4.4. Discussion

From the extensive surface chemistry analyses and contact angle measurements conducted in this study, we conclude that rare earth oxides are intrinsically hydrophilic and hydrocarbon adsorption governs the wettability transition of REO surface from hydrophilic to hydrophobic. We explored further to answer which adsorption mechanism would dominate or how the adsorption of volatile organic compounds or hydrocarbons in the air to the surface. Our observation tells us the adsorption mechanism will be based on both chemisorption and physisorption, neither only of one of them exclusively work. Especially, differences in the wettability recovery after plasma and solvent cleaning strongly supports the claim. Cerium oxide and some rare earth oxide materials have used as an oxidizing catalyst due to its reducing nature. REO works as dehydrogenation in oxygen-lean and hydrocarbon richer conditions at an elevated temperature[160, 183]. However, the mechanism of dehydrogenation of rare earth oxide at room temperature such in our experimental conditions is unknown. Previous studies have also shown that pre-physisorbed molecules are energetically more favorable for chemisorption rather than gas phase molecule colliding with the surface. However, since the adsorption of hydrocarbon is spontaneous and less controllable, we could not isolate them to study the exact mechanisms or adsorption dynamics. Further experimental studies or molecular dynamic (MD) simulations can solve this problem of how hydrocarbon adsorbs on the rare earth oxide surface.

4.5. Conclusion

In this study, we investigated the intrinsic wettability of rare earth oxides (REO) to address decade-long debates. The contact angle measurements resulted in increased over time from upon the exposure of the surface to air and hydrocarbon saturated atmosphere. REO surfaces were intrinsically hydrophilic, became hydrophobic as they adsorbed hydrocarbons. The adsorption of hydrocarbon from airborne VOC and the controlled hydrocarbon vapor was verified by multiple surface chemistry analysis methods. This study also suggested the adsorption of hydrocarbon are both chemisorption and physisorption. The chemisorbed hydrocarbon promotes further physisorption due to the higher affinity between the same or similar hydrocarbon molecules. This study offers a better understanding of intrinsic wettability of REO's and provides better design guidelines for REO based hydrophobic coatings and related catalytic activities.

CHAPTER 5: THIN-FILM CONDENSATION ON NANOSTRUCTURED SURFACES*

5.1. Introduction

Fundamental understanding and enhancing the efficiency of, condensation phase change is important to applications ranging from large scale systems such as heat exchangers in industrial power plants[4-7, 184-186] to in macro-, micro- or nanoscale systems such as compact heat sinks[77-78, 80, 187-188]. In addition to anthropomorphic applications, nature utilizes highly efficient condensation phase change for water harvesting[9-11] and self-cleaning[38-40]. When water vapor condenses on a high surface energy hydrophilic substrate, it forms a liquid film which accumulates and grows in thickness along the gravitational direction, termed filmwise condensation (Figure 5-1a). The liquid film can grow up to 100 μm thick, significantly decreasing the heat transfer between the surface and water vapor due to the low thermal conductivity of liquid water (≈0.6 W/m·K).[22] The key to enhancing condensation heat transfer is efficiently removing the liquid film when it is as thin as possible[7]. To enhance condensate removal, researchers more than 80 years ago demonstrated that by coating the condensing surface with a low-surface energy (hydrophobic) promoter, such as a thin polymer layer or self-assembled monolayer (SAM), water can condense into discrete droplets ranging in size from nanometers to millimeters[23]. Termed dropwise condensation (Figure 5-1b), these droplets grow via direct condensation and coalescence, result in rapid shedding (depicted with red arrows in Figure 1b) via gravitational body forces, and clear other droplets off the surface. The subsequent

* This chapter was reprinted (adapted) with permission from *Adv. Funct. Mater.* 2018, 28, 1707000 Copyright © 2017 Wiley-WCH. Junho Oh conducted the experiments, analyzed the data and wrote the manuscript under the advisement from Dr. Nenad Miljkovic.

clearing of the surface and re-nucleation makes dropwise condensation 10 times more efficient than filmwise condensation[7]. Furthermore, the recent combination of surface micro/nanostructures with conformal hydrophobic promoters has enabled ever smaller length scales (≈10 μm) of droplet shedding[24-33] providing significantly increasing heat transfer rates[24].

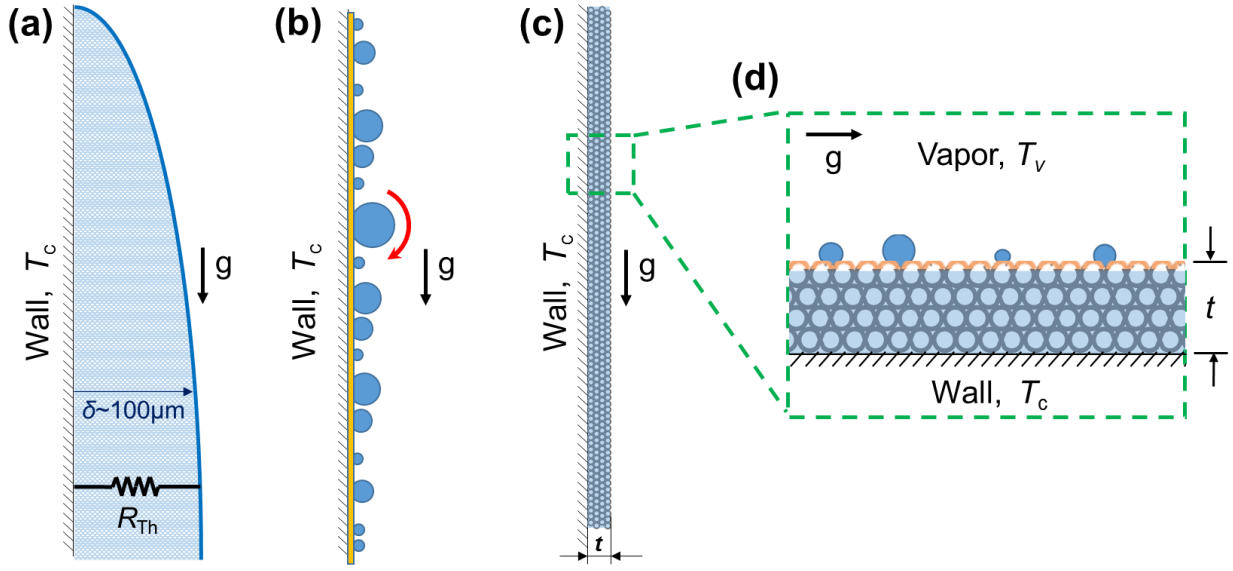

Figure 5-1 Side view cross-section schematics of (a) filmwise condensation, (b) dropwise condensation (red arrow represents roll-off and shedding) and (c) thin-film condensation on inverse opal structures having thickness, t, with (d) detailed view of confined water film inside the superhydrophilic porous structure. Orange color represents the hydrophobic 'promoter' coating present on the (b) dropwise and (c, d) thin film condensing surfaces. All modes of condensation are depicted on a cooled vertical wall at a uniform temperature T_c and vapor temperature, T_v.

Promoting lasting dropwise condensation is still an unsolved problem despite considerable effort spanning the 20th century. At a fundamental level, the durability of current promoter coatings provides stable dropwise condensation for days or weeks[34], not the year or decade timescales required by real life systems. The low durability is a direct result of the need for low thermal

resistance, and thus ultra-thin dropwise condensation promoter layers (< 1 μm). Thicker promoter coatings (~10 μm) can indeed last much longer (~1 year), however, the added thermal resistance of the coating outweighs the benefit seen from more rapid droplet shedding[35]. Hence, the vast majority of current condensation applications are relegated to utilizing the innate surface chemistry of high surface energy metal oxides that are hydrophilic to ensure long lasting filmwise condensation.

To address the issue of durability while utilizing the long-term stability of filmwise condensation, we demonstrate thin-film condensation on thin (<10 μm) and porous superhydrophilic surfaces coated with a layer of hydrophobic promoter as a nucleation deterrent and energy barrier for the condensed film to propagate above the surface (flooding, Figure 1c, d). By utilizing highly durable and temperature stable (≈ 500 °C) nickel inverse-opal (NIO) nanostructures coated with a simple chemical vapor deposition of decomposed hydrophobic polyimide (Kapton tape, DuPont), we prevent thin film growth by confining the condensate in the thickness dimension using Laplace pressure energy barriers[189], reducing thermal resistance, and therefore maximizing the condensation heat transfer. Using optical microscopy, we show preferential and stable nucleation inside the superhydrophilic nanostructures underneath the hydrophobic surface. We also observed a droplet-coalescence-driven wicking phenomenon into the underlying superhydrophilic structure, which ensures higher structure stability at elevated supersaturations. To quantify the heat transfer enhancement, and demonstrate the hydrodynamic stability of the condensate propagation in the lateral pore direction as opposed to through the hydrophobic top (flooding), we developed analytical models to show that heat transfer coefficients greater than 50 $kW/m^2 \cdot K$ can easily be achieved with inverse opal films having thickness ranging from ≈ 1-10 μm with pore neck radii of ≈ 0.1-1 μm. The outcomes of this

work not only develop a method to achieve ultra-high condensation heat fluxes using thin film condensation, but also establish a powerful surface engineering technique capable of potentially greatly enhancing the durability of functional condenser coatings to achieve hydrophobic-like performance on a more stable hydrophilic surface.

5.2. Experimental Methods

5.2.1. Fabrication of Biphilic Inverse Opals

The NIO was fabricated by the growth of Ni through sacrificial polystyrene (PS) opal templates by electrodeposition and the dissolution of PS afterwards. Three-dimensional (3D) face-centered cubic opals were made by self-assembly of 500 nm diameter polystyrene (PS) colloids (ThermoFisher Scientific Inc.) via evaporation. A mass of 0.6 g of colloids were first well dispersed in 45 mL of Millipore water by sonication. The Au coated Si substrates are cleaned by piranha solution (3:1 mixture of H_2SO_4 and H_2O_2) placed near vertical within vials containing the colloidal dispersion, ultimately resulting in opal formation. The resulting opal template was then sintered at 96°C for 2 hours to strengthen the opal and increase the contact area of the spheres (which will become the connection between the voids in the templated metal foam). The contact area of spheres will determine the neck radius of opal structure, which accounts for Laplace and viscous pressure drop. NIO was electrodeposited through the opal at a constant current density of 2 mA/cm^2 in a Technic RTU Mechanical Agitation commercial solution. After the Ni deposition was complete, the samples were immersed in THF overnight to dissolve the PS template.

To create the hydrophobic coating on top of the NIO structure (Figure 1c), the sample was placed adjacent to Kapton tape made of polyimide film (DuPont, $[C_{22}H_{10}N_2O_5]_n$) and heated using a rapid thermal processing machine (Bench Top RTP, Rocky Mountain Vacuum Tech, CO, USA) for 5

minutes at 500°C, 0.01-0.02 Pa, and heating rate of 50°C/sec. Polyimide based Kapton tape was chosen due to its higher temperature stability (< 400°C) when compared to other polymers (< 250°C), well characterized intrinsic advancing contact angle ($\theta_a \approx$ 70-90°), and common use in laboratory settings. Coating thickness measurements using ellipsometry on a Si coated wafer resulted in a decomposed polymer deposition thickness of ≈ 228 nm. The variation of the coating thickness was 0.3 nm over the Si wafer, which demonstrates the conformality of the coating. Note, the coating thickness on the NIO surface was measured to be ≈ 20 nm, thinner than the smooth Si wafer (≈ 228 nm) due to the much higher surface area and roughness of the sample.

5.2.2. Contact Angle Measurements

Contact angle measurements of ≈100 nL on the NIO structures were conducted using a microgoniometer (MCA-3, Kyowa Interface Science). The contact angle data were processed (FAMAS, Interface Measurements & Analysis System, Kyowa) using the half-angle method.

5.2.3. Scanning Electron Microscopy

Field emission scanning electron microscopy (FESEM) imaging were performed using FEI Quanta ESEM at high vacuum condition. The accelerating voltage was 5.0 kV, and spot size was 2.0 nm.

5.2.4. Ellipsometry

Ellipsometry was conducted using Gaertner L116C to measure the polymer coating thickness on a flat Si wafer. The coated wafer was modeled as a three-layered system with a top decomposed polyimide coating, a middle silicon dioxide layer and the silicon substrate. The optical constants used for the polymer coating were n = 1.68 and k = 0.[190] The middle oxide layer had a thickness

of 2.1 nm with refractive index n = 1.4761 and extinction coefficient k = 0.[191] The silicon substrate had a refractive index n = 3.874 and k = 0.01616.[192]

5.2.5. ToF-SIMS

ToF-SIMS analysis was performed on an uncoated NIO surface as a control and a hydrophobic coated NIO surface using a PHI Trift III (Physical Electronics, USA). The spectral data obtained was analyzed using WinCadence software (ULVAC-PHI, Japan).

5.2.6. Observation of Condensation Phenomena

We observed condensation behavior on the NIO surface using a customized top-view setup consisted of an upright optical microscope (Eclipse LV100, Nikon) and a high-speed camera (Phantom, V711, Vision Research) for top-view analysis. An LED light source (SOLA SM II Light Engine, Lumencor) was utilized for the illumination. The LED light source was specifically chosen for its high-intensity at lower power consumption (2.5 W) and narrow spectral range (380−680 nm) in order to prevent condensates evaporating at the surface due to light absorption. Samples were mounted horizontally on a cold stage (TP104SC-mk2000A, Instec). Samples were cooled to T_c = 2-5 ± 0.5°C to condense water vapor in laboratory ambient air with temperature and relative humidity T_{air} = 23 ± 0.5°C and $\varnothing$ = 30-50 ± 1% (Roscid Technologies, RO120), respectively. The condensation conditions represented a range of supersaturations ($S = P_v / [P_{sat}(T_c)]$, 0.97 ± 0.05 < S < 2.05 ± 0.1, where P_v and $P_{sat}(T_c)$ represent the vapor pressure of the laboratory air and saturation pressure at the sample temperature (T_c), respectively).

5.3. Results and Discussion

5.3.1. Biphilic Inverse Opal Structure

To create the superhydrophilic porous surface, we used NIO (see Section 5.2.1 for detailed fabrication methods). The NIO structure was intrinsically hydrophilic (Fig. 5-2a). The pore radius of the NIO structure used in this study was ≈ 250 nm and the porosity of the structure was ≈ 0.8.[193] Figure 2c demonstrates the superhydrophilicity of the NIO surface, where the advancing contact angle was measured to be 23.2° ± 1.5° and receding contact angle was ≈ 0°. Subsequent air plasma cleaning of the NIO structures resulted in spontaneous wicking even in the advancing state and an immeasurable (≈ 0°) contact angle.

Figure 2b shows the coated NIO structure with a polymer coating decomposed from polyimide on the top of the structure[194], demonstrating a very thin (≈ 10-20 nm) and conformal hydrophobic layer (for detailed ToF-SIMS analysis, see section C.1. of Appendix C.). The decomposition mechanism of the polyimide tape was dictated by end chain-scission (unzipping), resulting in the production and re-deposition of free radicals (monomer units or smaller substituents) on the NIO surface[194]. The measured apparent advancing and receding contact angles after coating the NIO surface with the decomposed polyimide (Fig. 5-2d) were θ_a^{app} = 150° ± 4.7° and θ_r^{app} = 145° ± 3.9°, respectively. We also measured the contact angles of the structure underneath to prove its biphilicity. After removing top layers by scratching with PTFE tweezer three times, the advancing contact angle became θ_a^{app} = 77.3° ± 8.1° and the receding contact angle was θ_r^{app} = 0°. Due to the nanoscale porosity of the NIO structure, diffusional resistance to volatile polyimide radicals resulted in deposition on the NIO top surface only, resulting in a superhydrophilic sublayer and superhydrophobic top layer.

It is important to note, the selection criteria for the hydrophobic top layer material is significantly relaxed when compared to classical hydrophobic or superhydrophobic surfaces. The lack of gravitational droplet shedding during thin film condensation necessitates that contact angle hysteresis of the hydrophobic coating need not be minimized. Rather, only the intrinsic advancing contact angle needs to be high (≈ 90°) to maximize the condensate confinement energy barrier. Furthermore, because the hydrophobic coating is not used as the condensing surface, the need for thicker and more durable films is not required.

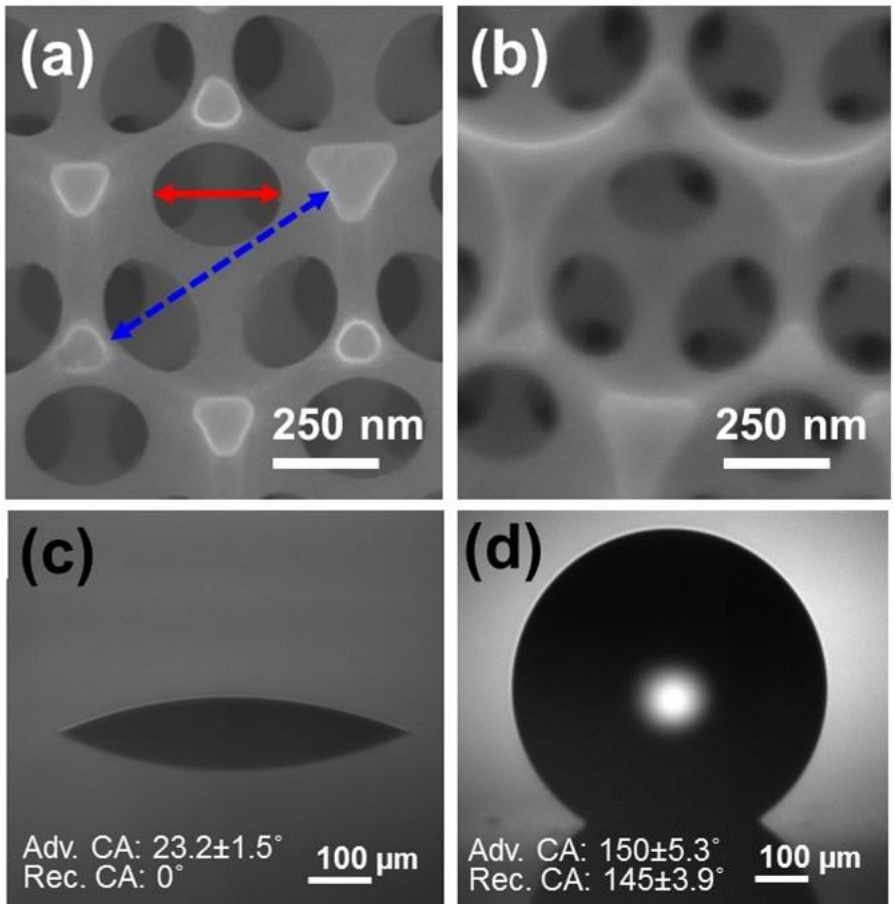

Figure 5-2 Top view scanning electron microscopy (SEM) images of the (a) virgin superhydrophilic NIO surface (opal diameter and neck diameter represented as the dotted blue and solid red arrow, respectively), and (b) hydrophobic NIO surface after decomposed polyimide deposition. Side view optical images of water droplets in the advancing state on the (c) virgin superhydrophilic NIO surface (shown in a) and (d) hydrophobic NIO surface (shown in b).

5.3.2. Hydrodynamics of Thin Film Condensation on Biphilic Inverse Opal Structures

We observed condensation phenomena on the biphilic inverse opal structure that we fabricated. At lower supersaturations ($S < 1.01 \pm 0.05$) water vapor nucleated inside the superhydrophilic structure as characterized by the darkening of the time-lapse optical image (Fig. 5-3). Nucleation on the internal hydrophilic surface was preferential compared to the external hydrophobic polymer layer due to the lower energy barrier for nuclei formation on high surface energy substrates as dictated by classical nucleation theory (CNT)[195]. To test the stability of the preferential condensation, we performed condensation experiments at elevated supersaturations, noting the initiation of droplet nucleation on the top polymer layer at $S > 1.1 \pm 0.05$. Although CNT predicts that the critical supersaturation for nucleation on the hydrophobic layer ($S_{c,hydrophobic} \approx 4$) is much greater than the hydrophilic internal NIO surface ($S_{c,hydrophobic} \approx 1.01$), the presence of high surface energy adsorbed volatile organic compounds and agglomerates on the decomposed polyimide layer[196], or exposed high surface energy defects during polymer deposition[102, 197-200], enable nucleation at lower supersaturations.

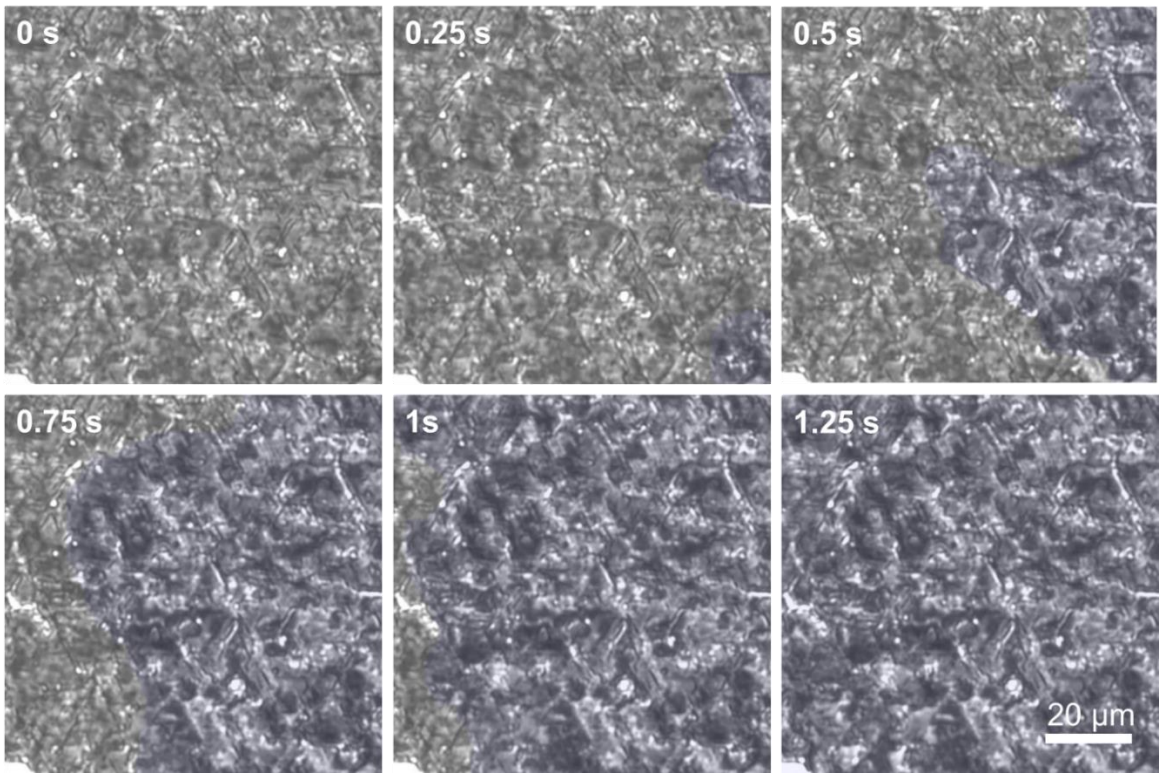

Figure 5-3 False-colored top-view time-lapse image of water vapor nucleation and propagation of condensate inside the superhydrophilic NIO structures. The images were false-colored blue with very low opacity (5 %) to help identify the condensate inside the structure for clarity.

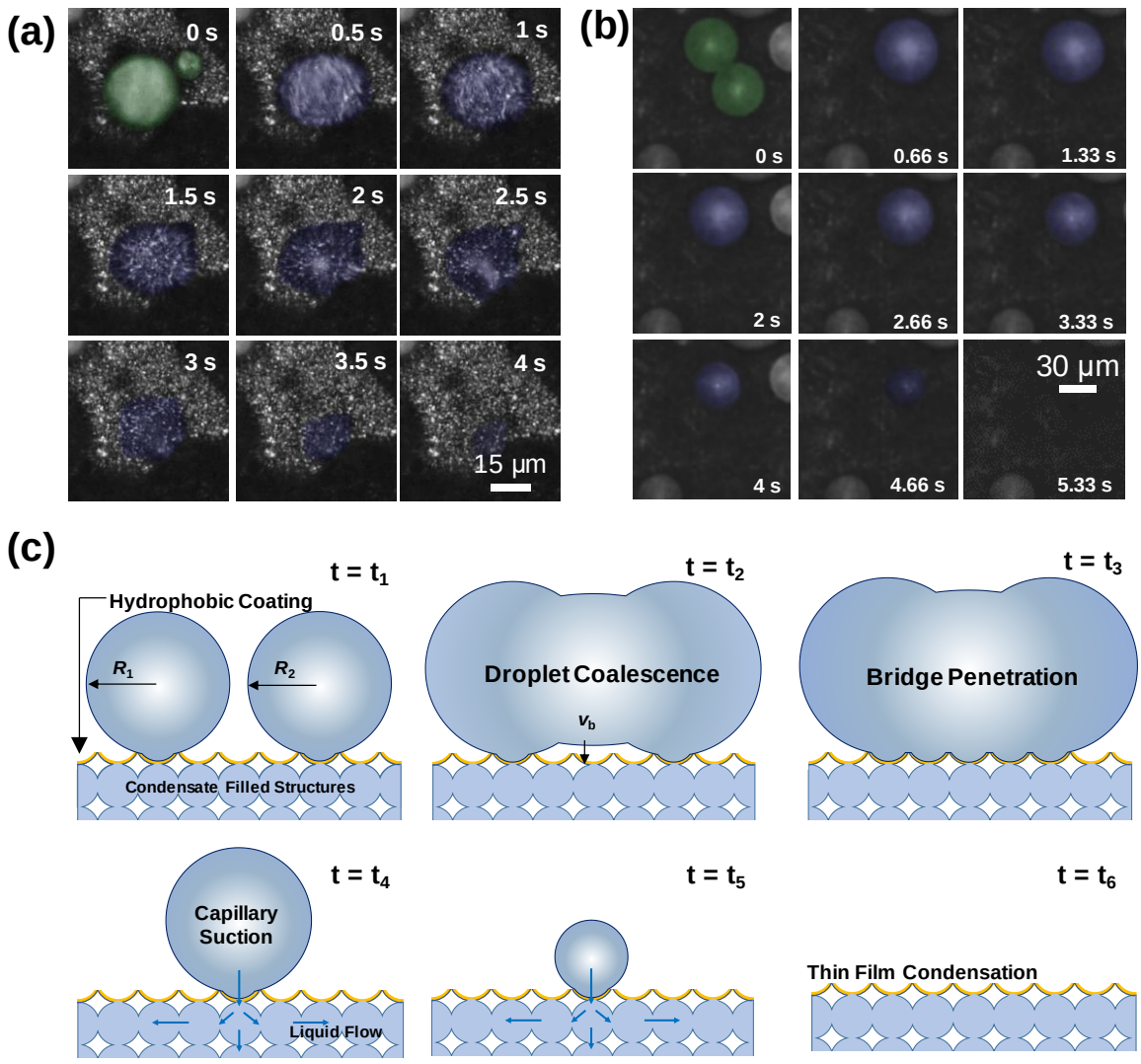

Figure 5-4 (a, b) False colored, time-lapse, top view optical microscopy images showing the capillary suction phenomenon on the hydrophobic NIO surface (Figure 5-1b, d) (c) Schematic of the droplet suction mechanism on the hydrophobic NIO surface. The orange layer represents the hydrophobic coating on top of the NIO structures. Droplet coalescence acts to generate a liquid-vapor interface impingement into the structure (t_3), thereby connecting the Cassie state droplets residing on top of the hydrophobic coating with the filled superhydrophilic sublayer, and initiate suction (t_4 -t_6).

Interestingly, droplets growing on the top hydrophobic surface at elevated supersaturations were not stable. As adjacent droplets grew and began to coalesce, we observed capillary suction of the coalesced droplet into the superhydrophilic NIO sublayer (Fig. 5-4a, b). The timescale of the

capillary suction was slow (~ 1 s), indicating an elevated pressure drop inside the structure needing to be overcome by the droplet-curvature-dependent Laplace pressure. The capillary suction mechanism is similar to periodic rejuvenation previously observed on amphiphilic nanostructures where after undergoing coalescence, droplets transition to Wenzel states and became fluidically linked via the wetted sublayer[201]. However, in our experiments the droplets growing on the hydrophobic top layer were in the Cassie state and disconnected from the wetted sublayer. Observation of the condensation process over periods of one hour yielded no Laplace pressure driven coalescence between adjacent droplets indicating stable formation isolated Cassie droplets. Laplace pressure driven coalescence between adjacent droplets with different radii of curvature was not observed due to the lack of fluidic linkage between droplets. Only after coalescence and impingement of the radial liquid bridge on the NIO structure could the Laplace energy barrier be overcome, resulting in droplet transition to the Wenzel state and wicking into the wetted sublayer (Fig. 5-4c). The impinging velocity of the coalescing liquid bridge (v_b) impacting the NIO structure is $v_b \approx 2{D_0}^2(\gamma/\rho R)^{1/2}$, where γ and ρ are the water surface tension and density, R is the initial radius of coalescing droplets, and D_0 is a constant ranging from 1.39 to 1.62[202-205]. Water hammer pressure of the impinging interface scales as $P_{wh} \sim \rho {v_b}^2$. If the water hammer pressure overcomes the capillary pressure barrier ($2\gamma/r_p$, where γ is the condensate liquid-vapor surface tension and r_p is the neck radius or the size of opening between pores, $r_p \approx 150$ nm), the liquid bridge can fluidically connect with the underlying liquid in the superhydrophilic sublayer (for detailed derivation, see section C.2. of Appendix C.). Scaling of the water hammer and capillary pressure barriers results in stable capillary suction for coalescing droplet radii having $R < 2{D_0}^4 r_p$

≈ 1.9 to 3.4 μm, in good agreement with or smaller than the radii observed in our experiments. The slight discrepancy between theory and experiments was most likely due to the presence of crack-based defects in the NIO structure resulting in larger effective r_p [206]. The elimination of the connection between the wetted NIO superhydrophilic layer and droplets residing on top of the hydrophobic surface is beneficial from a durability point of view. The capability of Cassie droplets to be absorbed by the wetted sublayer ensures the ability to: 1) maintain stable thin film condensation and tight control of the thin film thickness and heat transfer performance, and 2) minimize condensation induced degradation of the hydrophobic functional coating, which is strictly utilized as a Laplace energy barrier to prevent condensate propagation above the structures from the wetter sublayer.

On the basis of the understanding developed during capillary suction and sublayer condensation dynamics, we investigated the hydrodynamic criteria required to ensure stable thin film condensation. As a condensate film grows inside the wetting sublayer, it is confined to the thickness of the layer by the Laplace energy barrier of the hydrophobic coating. In order to ensure that the liquid propagates laterally through the superhydrophilic layer as opposed to bursting through the top pores (flooding)[24], the structure length scale should be tailored such that the Laplace pressure drop through the hydrophobic top pores is larger than the viscous pressure drop encountered by condensate propagation laterally through the pore to the sample edges. The viscous pressure drop through the superhydrophilic structures scales as:

$$\Delta P_v \sim \frac{hL^2 \Delta T \mu}{h_{fg} \kappa \rho t} \qquad \text{(Eq. 5-1)}$$

where h is the condensation heat transfer coefficient, L and t are the lateral sample size and structure height (Figure 5-1c,d), ΔT is the vapor-to-surface temperature difference, μ, ρ, h_{fg} are the

condensate dynamic viscosity, density, and latent heat of phase change, respectively, and κ is the pore geometry and length scale dependent permeability (for a detailed derivation, see section C.3. of Appendix C.). The viscous pressure drop scales linearly with condensation heat flux ($h\Delta T$) due to the dependence on condensate flow rate in the superhydrophilic layer and its accumulation rate in the structures. Note, the aforementioned scaling assumes one dimensional Darcy flow through a permeable layer and does not take into account the gradual mass addition along the propagation length (see section C.4. of Appendix C.). In reality, condensate addition would occur over the whole sample surface area, making the viscous pressure drop scaling developed above (Eq. 5-1) a conservative estimate. Furthermore, the scaling assumes that i) the entirety of the superhydrophilic structure is filled with condensate and devoid of liquid-vapor menisci due to spontaneous wetting and wicking, and ii) the free surfaces at the lateral extents of the sample have infinite radii of curvature.

The Laplace pressure barrier confining the condensate to the structure height can be estimated assuming a hemispherical liquid-vapor interface shape protruding through the hydrophobic pores as:

$$\Delta P_c \sim \frac{2\gamma}{r_p} \qquad \text{(Eq. 5-2)}$$

For the NIO inverse opal structures studied here (Fig. 5-2a), $r_p \approx 150$ nm. Due to the re-entrant nature of the NIO structures, the intrinsic advancing contact angle of the hydrophobic coating is not present in Eq 5-2. Contact line pinning at the corners of the top surface due to the Gibbs' criterion, result in Laplace pressure barrier maximization[97, 103, 207]. The permeability of NIO structure was assumed to be $\kappa = 10^{-0.458}(r_p)^{2.18}$ which was obtained from experimental

measurements of porous sintered copper wicks[208-209] and copper inverse opal structures[210-211]. The correlation is in good agreement with the generalized permeability of porous structures, which are dependent on the square of the characteristic length of the pore structure[210-211].

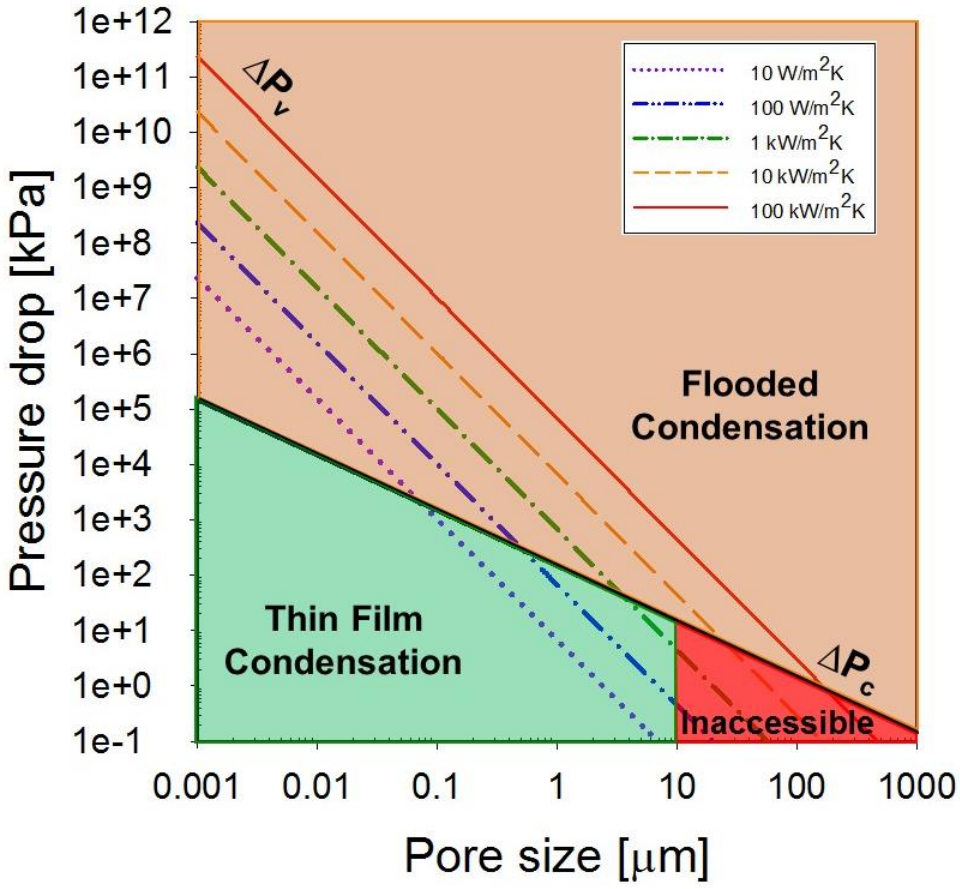

Figure 5-5 Hydrophobic barrier pressure drop (ΔP_c, black solid line) and viscous pressure drop (ΔP_v, colored dotted lines) as a function of neck radius (r_p) for different condensation transfer coefficients and film thickness, t = 10 μm. To prevent flooding and ensure stable thin film condensation, the viscous pressure drop from the sample center to the edge must be lower than the barrier pressure drop ($\Delta P_v < \Delta P_c$, green shaded area). If the viscous pressure drop exceeds the barrier pressure drop ($\Delta P_v > \Delta P_c$, orange shaded area), liquid will propagate through the top structures and flood the surface. The red shaded area labeled inaccessible represents the length scale at which the neck radius is greater than the film thickness ($r_p > t$). All calculations done with ΔT = 5 K.

Figure 5-5 shows the viscous (colored lines) and Laplace pressure drops (ΔP_{pore}, black line) as a function of inverse opal neck radius for a range of condensation heat transfer coefficients ($10 < h < 1000$ kW/m^2·K). As the neck radius decreases, the maximum allowable condensation heat flux decreased due to the balance between the increasing Laplace pressure barrier ($\sim 1/r_p$) and viscous pressure drop ($\sim r_p^{-2.18}$). Indeed, scaling of Eq. 5-1 and 5-2 reveals that the maximum critical heat transfer coefficient ($h_{\max}$) attainable while maintaining the confined condensate film from bursting is:

$$h_{\max} \sim \frac{2\gamma r_p^{1.18} h_{fg} \rho t}{L^2 \Delta T \mu} \qquad \text{(Eq. 5-3)}$$

By examining the intersection points of the viscous and Laplace pressure drops at each individual condensation heat transfer coefficient, we could determine the critical maximum neck size for droplet suction. Under typical dropwise condensation conditions ($20 < h < 150$ kW/m^2·K), the critical neck radius was determined to be 5 μm $< r_p <$ 50 μm.

The scaling analysis and critical neck size results are in excellent agreement with the observed capillary suction on our NIO surfaces. Due to the presence of non-condensable gases[212], the condensation rates in our experiments ranged from 0.01 to 0.1 W/m^2, corresponding to $0.002 < h < 0.02$ W/m^2·K. After coalescence and capillary bridging, the Laplace pressure due to droplet curvature ($r_1 \approx 20$ μm, $\Delta P_{Laplace} \cong 2\gamma / r_1 \approx 7$ kPa, Fig. 5-4a) was large enough to overcome the viscous pressure drop inside the wetted superhydrophilic sublayer ($\Delta P_v < 1$ kPa, $L = 1$cm, $r_p \approx$ 150 nm) due to the low condensation rate and spontaneously wick inside the structure.

Due to the more rapid increase in viscous pressure drop compared to the Laplace pressure increase as the structure length scale decreases, Fig. 5-5 and Eq. 5-3 suggest that in order to maximize thin

film condensation heat transfer: 1) inverse opal structures having larger pore and neck radii (r_p > 1 μm) should be pursued, or 2) the viscous and Laplace pressure drops should be decoupled through the use of hierarchical or multi-scale inverse opal structures, such as those typically used in thin film evaporation[213-217]. By reducing the hydrophobic layer structure length scale, while maximizing the superhydrophilic sublayer pore and neck size, vias for condensate drainage and propagation are formed with simultaneous thin film condensation confinement from the nanoscale top structures.

5.3.3. Heat Transfer Enhancement of Thin Film Condensation

To quantify the thin film condensation heat transfer, we developed an analytical thermal resistance based model to compare performance with state-of-the-art (SOA) filmwise and dropwise condensation (for a detailed derivation, see section C.5. of Appendix C.). Figure 5-6a shows the average condensation heat transfer coefficient ($\bar{h}$) on a flat vertical plate as a function of plate height for dropwise condensation, filmwise condensation, and thin film condensation. As expected, the thick liquid film on hydrophilic filmwise condensing surfaces acts to diminish heat transfer as plate height increases. Plate heights of 1 cm can achieve $\bar{h}_{filmwise} \approx 20$ kW/m^2·K, poorer performance than dropwise or thin film condensation. Dropwise condensation has been shown to be independent of plate height and to have a wide range of values depending on non-condensable gas concentration ($50 < \bar{h}_{dropwise} < 300$ kW/m^2·K).[5, 63] The predicted thin film condensation heat transfer coefficient on the NIO surface tested here was $\bar{h}_{thinfilm} \approx 50$ kW/m^2·K, significantly higher than classical filmwise condensation, approaching that of dropwise condensation.

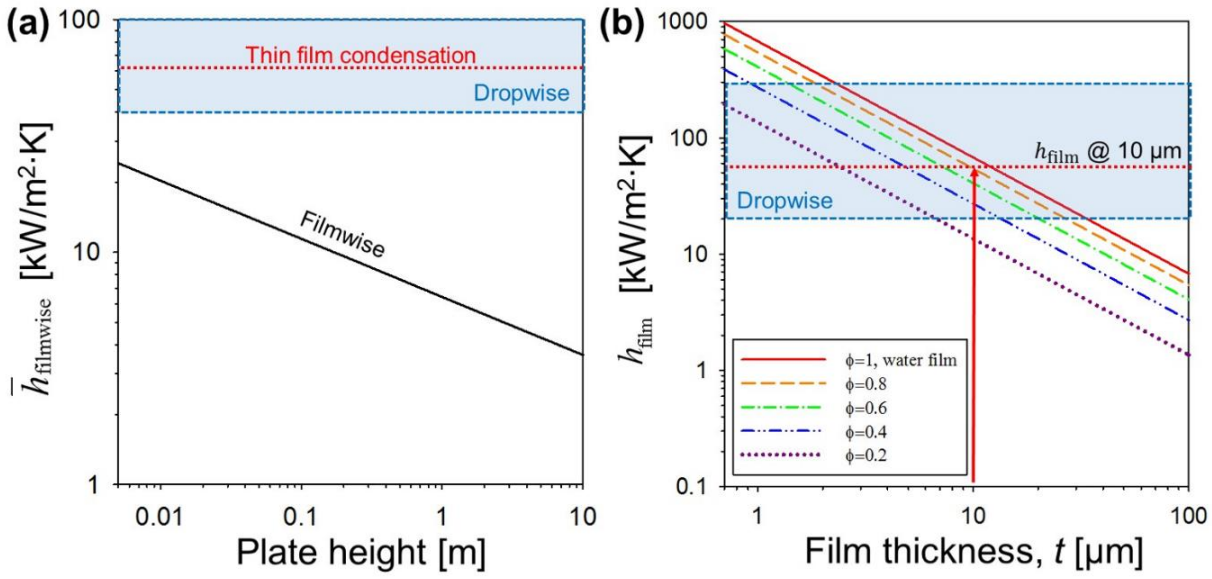

Figure 5-6 (a) Average condensation heat transfer coefficient ($\bar{h}$) for water vapor as a function of condensing surface height (vertical orientation, gravity pointing downwards, Figure 1a, b, c) for filmwise, dropwise, and thin film condensation. The thin film condensation structure thickness was t = 10 μm. (b) Thin film condensation heat transfer coefficient versus film thickness (t) for varying structure solid fraction (φ). As the film thickness increases, the thermal resistance increases, thereby diminishing heat transfer performance. Higher solid fractions result in less exposed area for condensation to occur, resulting in a concurrent decrease in heat transfer performance.

We computed the thin film condensation heat transfer coefficient to elucidate the fundamental parameters affecting thin film condensation, and to better couple the hydrodynamic and thermal analyses. The heat transfer coefficient was derived as a function of structure thickness (t) and solid fraction (φ) defined as the exposed solid structure area normalized by the total projected area (Fig. 5-4b). The results show that careful consideration of the structure film thickness is required. Although ultra-thin liquid films can achieve ultra-high condensation heat transfer coefficients (> 100 kW/m^2·K), they concurrently act to increase the viscous pressure drop (Eq. 5-1) and hence flooding (Fig. 5-5). Furthermore, the results show that although the creation of Laplace pressure energy barriers can indeed confine the liquid film, they also act to reduce the total area for condensation (through increase in φ), hence minimization of the solid fraction is favorable.

The thermal analysis presented in Fig. 5-6 provides a necessary design tool for the hydrodynamic aspects of the surface structure (Fig. 5-5). Once the structure thickness, neck size, and solid fraction are specified, the condensation heat transfer can be computed (Fig. 5-6b) and be utilized in Fig. 5-5 to elucidate hydrodynamic regimes of operation. It is very important to note, the heat transfer calculations (Fig. 5-6) use the thermal conductivity of pure water (0.6 W/m·K), resulting in a highly conservative condensation heat transfer estimation. In real life, the composite NIO/water layer thermal conductivity will be higher, estimated as ≈ 10 W/m·K using effective medium theory (see section C.6. of Appendix C.). The higher effective thermal conductivity impacts the allowable structure height, enabling thicker NIO structures, while substantially lowering the viscous pressure drop of lateral liquid propagation.

The coupled hydrodynamic-thermal analysis suggests that higher performance is possible via the decoupling of viscous pressure loss dictated by the internal superhydrophilic pores from the Laplace energy barrier dictated by the hydrophobic pores on top of the structure[218-221]. If a bi-

porous wick structure were used with a nanoporous (r_p = 100 nm) barrier layer and a thin (t = 10 μm) microporous (r_p = 1 μm) superhydrophilic wetting sublayer, the potential heat transfer coefficient could reach $h_{filmwise} \approx 200$ kW/m^2·K (for a detailed calculation, see section C.7. of Appendix C.).

In the future, it would be interesting to experimentally test thin film condensation performance on both mono-porous and bi-porous inverse opal wick structures to verify the predicted condensation heat transfer experimentally. Although the simplified and coupled hydrodynamic and thermal analyses developed here elucidate important information about the design and performance of thin film condensers, avenues for improvement exist. Future models should include the effects of two-or-three-dimensionality and gravitational potential (for vertical surfaces) in the Darcy flow model, the effects of meniscus curvature at the hydrophobic pores and their effect on saturation pressure of the water vapor as well as enhanced condensation surface area[215], a more detailed analysis of the temperature distribution throughout the filled porous network, and lastly, the coupling between the hydrophobic coating intrinsic wettability and the surface structure geometry on the Laplace pressure barrier (Eq. 5-2). Furthermore, future work should focus on quantifying the enhanced durability of thin film condensation when compared to dropwise condensation. Although nucleation on the top surface can be suppressed and elimination of the hydrophobic surface as the condensing surface will be beneficial for longevity, the presence of high surface energy random defect sites in the hydrophobic coating, alternative deposition methods of coating and their nucleation behavior needs to be investigated further. Lastly, future studies should place significant importance on the edge design of the condensing surfaces where the thin film condensate needs to drain away from the sample.

The NIO experiments conducted in this study present an ideal platform for the development of further tailored thin film condensation surfaces. However, careful attention must be paid to surface size defects. Due to the need for hydrophobic barriers on the structure top, pore or neck size mismatch due to defects can potentially lead to flooding of the surface via short circuiting the fluid flow path and drastically reducing the confinement pressure drop. Interestingly, the platform developed here is analogous to thin film evaporation, where the use of bi-porous wicks[222-223], minimization of viscous pressure loss[217, 224-226], and vapor diffusion venting[227-229] have all be studied in detail. The analogous physics and knowledge gained from thin film evaporation stands to significantly accelerate the development of thin film condensation. The results presented here provide guidelines for the fabrication of high performance micro/nanostructured surfaces for high condensation heat flux applications. Furthermore, the results underscore the importance of the surface design and operating conditions for condensation heat and mass transfer on micro/nanostructured superhydrophobic surfaces and also provide insights into the surface design requirements for high heat flux applications.

5.4. Conclusions

In summary, we have demonstrated thin film condensation on a superhydrophilic structured NIO inverse opal surface coated with a hydrophobic polymer top player as a platform for achieving ultra-high condensation heat flux ($\approx$ 200 kW/m^2·K) while decoupling the hydrophobic surface from the thermal aspects of the condensation process and hence enhancing durability when compared to classical dropwise condensation. Droplet condensation on top of the hydrophobic structure was shown to be unfavorable due to a capillary wicking mechanism dictated by coalescing droplets being wicked into the wetting superhydrophilic sublayer. Hydrodynamic

analysis revealed that the structure length scale (pore and neck size, solid fraction, and structure thickness), are key parameters that need to be considered to overcome viscous pressure drop due to condensate accumulation inside the thin confined film. Thermal analysis suggests that decoupling of the hydrophobic top pores from the superhydrophilic sublayer micropores via the use of bi-porous structures is suggested to achieve even higher heat fluxes (> 200 $kW/m^2 \cdot K$). These results provide guidelines for the fabrication of potentially durable and high-performance micro and nanostructured surfaces for high condensation heat flux applications.

CHAPTER 6: JUMPING-DROPLET ELECTRONICS HOT SPOT COOLING*

6.1. Introduction

Recent advances in electronic materials and circuit architectures have catalyzed an increase in power density (power-to-volume ratio) and the specific power (power-to-weight ratio) of both stationary and mobile systems.[230-231] The trend of replacing bulky pneumatic and mechanical systems with smaller electrical systems in more-electric and fully-electric vehicles ranging from automobiles to aircrafts has created a demand for lighter and more compact power electronics. Yet, the ability to remove heat from internal hot spots constrains the design of converters and inverters.[232] Phase change heat transfer offers a platform to efficiently remove heat from electronic devices and transfer it via the generated vapor phase (evaporation in heat pipes and vapor chambers) to the outside environment.[233] However, recent advances utilizing wide bandgap semiconductors have shown that the majority of heat can be generated locally near spatially distributed hot spots.[232, 234] Traditional cooling schemes can also be stymied by the temporal variation in hot spot locations concurrent with electro-thermal optimization and novel circuit architectures.[235]

In this work, we experimentally demonstrated jumping droplet-based active cooling of electronics hot spots with nanoengineered superhydrophobic surfaces. Recent studies have shown that when small water droplets (≈1-100 μm in diameter) merge on superhydrophobic nanostructured

*This chapter was reprinted (adapted) with permission from *Appl. Phys. Lett. 110, 123107* Copyright © 2017 American Institute of Physics Publishing. Junho Oh is the main author of the publication. Junho Oh fabricated the samples, conducted the experiments, analyzed the data and wrote the manuscript with the other co-authors.

surfaces, droplets can spontaneously eject via the release of excess surface energy irrespective of gravity.[28, 236-237] A number of works have since fabricated superhydrophobic nanostructured surfaces to achieve spontaneous droplet removal for a variety of applications including self-cleaning,[238-239] condensation heat transfer enhancement,[20, 240-243] thermal diodes,[244] vapor chambers,[245] electrical energy harvesting,[246] and anti-icing.[247] Furthermore, we recently discovered that these jumping droplets are positively charged (≈10–100 fC), due to electric-double-layer charge separation at the hydrophobic coating/condensate interface,[248] and can be manipulated with electric fields.[25, 248-249] Here, we take advantage of this unique droplet-charging phenomenon to demonstrate electric-field-enhanced (EFE) jumping-droplet hot spot cooling, where the charged droplets jump between superhydrophobic copper oxide (CuO) condensers and either single or multiple high power gallium nitride (GaN) transistors acting as local hot spots to remove heat via droplet evaporation. We experimentally demonstrated spatially and temporally-controllable jumping-droplet based cooling of ≈1 W/cm^2 and describe near term approaches to increase heat fluxes to 120 W/cm^2.

6.2. Experimental Methods and Results

The utilization of droplet-jumping and active electric fields to locally cool mobile hot spots builds on state-of-the-art vapor chamber designs with several significant advantages as follows: (i) The electronics act directly as the evaporator and minimize thermal resistance as typically observed through the utilization of thermal-interface-materials and channel walls.[250] If integrated into a jumping-droplet vapor chamber geometry due to electrical isolation concerns, the mass flow rate of the liquid inside the jumping-droplet vapor chamber is not dictated by the height of the wick structure, but by the jumping frequency since the condenser liquid is returned through the vapor space.[245] (ii) Spatial and temporal control of the jumping droplet motion is possible with electrostatic fields such that mobile hot spots can be sensed and cooled as needed.[25] (iii) The low Bond number of the jumping droplets ($Bo \sim 10^{-3}$) allows operation independent of gravitational orientation. (iv) The out-of-plane jumping return is scalable and particularly suitable for planar systems, unlike conventional vapor chambers with capillary return along wicked walls, where longer liquid return paths are expected for devices of larger areas.[245, 23]

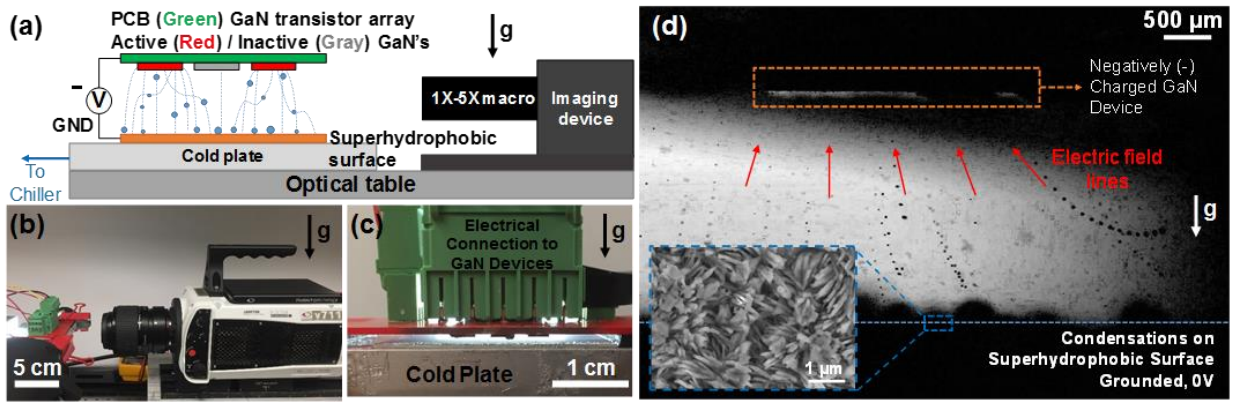

Figure 6-1 (a) Side view schematic and (b) photograph of the experimental setup for characterizing jumping droplet cooling of GaN transistors. (c) Side view image of the experimental setup showing the GaN electrical contact (green), the PCB with GaN devices (red), and superhydrophobic surface resting on the cold plate. (d) Composite image of several successive frames from a high speed video of electric-field-enhanced jumping-droplet condensation toward a GaN transistor. Electric field lines are depicted by red arrows. The droplet trajectories clearly follow (are influenced by) the electric field lines, which are depicted by red arrows. Inset: top-view scanning electron micrograph of a C_4F_8 functionalized (≈50 nm) superhydrophobic CuO surface used in these experiments.

To investigate jumping-droplet electronics cooling, a printed circuit board (PCB) with a single active integrated GaN field effect transistor (FET, EPC2034)[251] was positioned above the nanostructured superhydrophobic CuO surface. The circuit board was placed on top in order to test the worst-case scenario of droplet jumping against gravity (Figure 6-1a-c)). The CuO nanostructures (Fig. 6-1d, inset) were grown on commercially purchased 800 μm thick Cu tabs with overall dimensions of 50 x 50 mm. Each tab was cleaned in an ultrasonic bath with acetone for 10 min and rinsed with ethanol, isopropyl alcohol, and deionized (DI) water. The tabs were then dipped into a 2.0M hydrochloric acid solution for 10 min to remove the native oxide film on the surface, then triple rinsed with DI water and dried with clean nitrogen gas. Nanostructured CuO films were formed by immersing one of the cleaned tabs into a hot (≈ 98°C) alkaline solution composed of $NaClO_2$, NaOH, $Na_3PO_4 \cdot 12H_2O$, and DI water (3.75: 5: 10: 100 wt. %).[252] During the oxidation process, a thin (≈300 nm) Cu_2O layer was formed that then re-oxidized to form sharp, knife-like CuO oxide structures with heights of $h \approx 1$ μm, a solid fraction $\varphi \approx 0.02$ and a roughness factor $r \approx 10$. To render the CuO tabs superhydrophobic, a C_4F_8 hydrophobic coating was applied with chemical vapor deposition. This process allowed for the development of a highly conformal (≈50 nm thick) polymer layer on the CuO surface. Goniometric measurements (MCA-3, Kyowa Interface Science) of ≈ 300 nL droplets on a smooth C_4F_8-coated silicon wafer surface showed advancing and receding contact angles of θ_a = 121 ± 5.1° and θ_r = 105 ± 9°, respectively. Meanwhile, the advancing and receding contact angles on the superhydrophobic CuO surface were measured to be θ_a^{app} = 166 ± 6° and θ_r^{app} = 156 ± 7°, respectively.

To initiate jumping-droplet hot spot cooling, the temperature of the CuO tab was reduced to ≈ 5°C via a cooling water flow (Fig. 6-1a,c) until jumping-droplet-condensation occurred. To visualize the behavior, a gap between the parallel devices was observed with a high speed camera. Due to

electric-double-layer charge separation at the liquid-hydrophobic coating interface,[248] the jumping droplets departed the surface with a droplet radius dependent electrostatic charge (~10 fC). The jumping droplets travelled from the CuO surface to the circuit board, resulting in evaporative cooling of the hot GaN FET. In order to quantify cooling, EFE jumping droplet condensation for a single GaN device for cases with and without an external electric field of -100 V for the guard ring or the source pin potential of the GaN FET was studied.

Using rear lighting and long exposure time imaging, images and videos of jumping droplet phenomena in the gap were obtained. In the no-field condition, droplets jumping with insufficient inertia fall back to the superhydrophobic surface. In contrast, an external electric provides sufficient force to guide droplet's with insufficient inertia along electric field lines to the GaN device as depicted in Fig. 6-1d. The unique parabolic path in the right hand side of Figure 6-1d also reveals how the droplet accelerate toward the power devices due to the presence of an electric field. Accelerations between 3 and 6 m/s^2 for the droplets attracted by the electric fields were observed from measurements when a -100 V potential was applied across a 3 mm spacing between the cold plate and the GaN transistor, thus, enhancing the cooling capability by improving the rate and the number of droplets that reach the GaN FET. The applied fields (200 – 300 V/cm) are similar to the critical fields needed to overcome gravitational and drag forces as shown in previous studies.[249]

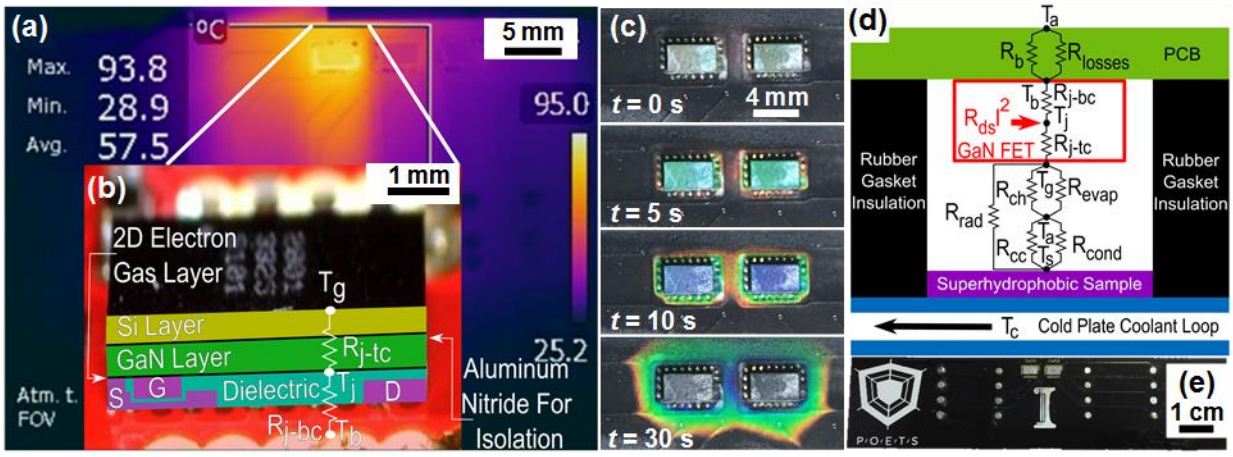

Figure 6-2 (a) Thermal infrared image of GaN FET with (b) detailed device structure. (c) Top view time-lapse liquid crystal thermographic images of the two GaN device during startup. Thermal steady-state was reached at 30 seconds. Red corresponds to 70°C and violet corresponds to 90°C. For infrared and liquid crystal thermography experimental details, please see Supplementary Material, section S2. (d) Thermal resistance network of experimental setup. For a detailed model description, please see Supplementary Material, section S1. (e) Top view photograph of the two-GaN PCB.

Steady-state infrared imaging (Fig. 6-2a) of the active GaN FET (Fig. 6-2b) as well as transient time-lapse liquid crystal thermography (Fig. 6-2c) were able to provide qualitative information about the GaN device temperature and its high temperature localization (hot spots) and to highlight how heat spread in the PCB (see Appendix D., section D.X.). Yet, the inability to view the device while integrated with the superhydrophobic surface required the use of thermocouples. By attaching thermocouples to the transistor and the cold plate, quantification of the GaN FET steady-state temperature for various spacings (2 – 4 mm) between the circuit and cold superhydrophobic sample was studied. Figure 6-2(d) shows the thermal circuit corresponding to the experimental setup. The GaN device was assumed to have a uniform temperature, T_G due to the low Biot number (Bi ~ 10^{-2}) for the cooling conditions and geometry studied here. Joule heating of 1.57 W was generated inside the GaN transistor at a rate of RI^2 where R = 7 mΩ is the internal electrical resistance of the GaN FET, and I = 15 A is the DC current flowing through the device. The heat

is dissipated either to the backside (through the board, then to ambient air, T_{amb} = 23 ± 0.5°C), or to the front side (towards the superhydrophobic sample, T_s = 5 ± 0.5°C). Miscellaneous losses to ambient air have been lumped into a thermal resistance, R_{losses}, which was determined through calibration during the no-jumping condition (see Appendix D, section D.1.). Using the cross-sectional area of the GaN FET (A_{GaN} = 0.12 cm^2),[251] a total heat flux of 13.2 W/cm^2 was dissipated. The cooling benefit can be separated into its contributing factors of radiation, convection, conduction through the back of the PCB, and heat removed via jumping droplet condensation and subsequent evaporation from the GaN device. The thermal resistance network of Fig. 6-2d was solved by inputting the relevant experimentally measured temperatures and solving for all of the relevant heat transfer pathways during circuit operation for the no-jumping, no-field jumping, and EFE jumping cases (see Appendix D, section D.1.). Table 6-1 summarizes the measured and calculated performance, showing that although only modest GaN FET temperature decreases (~ 2°C) were obtained by jumping droplet cooling, EFE condensation enhances the heat transfer from the hot spot by ≈ 200% and 20% when compared to cooling without jumping and non-EFE jumping, respectively. The relatively low heat fluxes dissipated by our device was mainly due to the presence of non-condensable gases (NCGs) in the vapor environment. The condensation of water vapor leaves behind NCGs (air) that blanket the superhydrophobic surface and act as a diffusion barrier for water vapor.[253-254] The counter diffusion of water vapor to the surface, coupled with the diffusion of NCGs away from the surface, significantly deteriorate the condensation heat transfer process, and hence decrease the effective surface-to-vapor temperature difference.

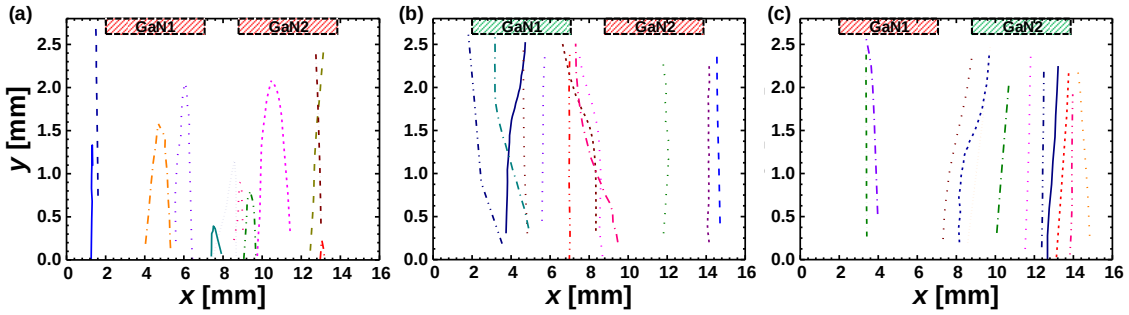

Figure 6-3 Droplet trajectories (a) without electric field (shaded red), (b) electric field applied to the left GaN transistor (shaded green), and (c) electric field applied to the right GaN transistor (shaded green). Gap spacing, voltage, and electric field strength were: 2.5 mm, -100 V, and -40 V/mm. E-Field is pointing toward the GaN devices as described in Figure 2. In addition to directing jumping droplets to the active transistor, the electric f field also prevented droplet return due to gravitational forces as well as vapor flow entrainment back to the condensing surface

To investigate the possibility of using jumping-droplet EFE condensation to achieve dynamic spatial-temporal control of cooling for mobile hot spots, we repeated the experiments with a modified two transistor circuit having two GaN devices spaced 3 mm apart in the horizontal direction (Fig 6-2e). By observing droplet trajectories through high speed imaging, we were able to plot the trajectories of droplets from the superhydrophobic surface to the GaN devices with no-field, EFE condensation with the electric field biased towards only one GaN FET (GaN1) or the electric field biased towards the other GaN FET (GaN2) (Fig. 6-3). In contrast to Fig. 6-3a where no external electric fields are employed, Fig. 6-3b and 6-3c underscore how an external electric field dramatically increases the average number of droplet trajectories directed toward a specific GaN transistor and demonstrates spatially controllable cooling. The droplet trajectories in Fig. 6-3c, which appear to stop before reaching the GaN FET, are a good example of droplets leaving the plane of focus for the high-resolution video camera. In this case, the droplets will reach the GaN device due to the external electric field. The droplet's initial velocity, as measured from the videos, did not show a significant deviation from the inertial-capillary scaled velocity, consistent with

previous works[25, 28, 248] that that have shown that the separation of charge on the superhydrophobic surface happens as a result of jumping, leading to electrostatic interaction contributions only after the jump. However, we expect that over longer operational time periods, the field-mediated reduced droplet return to the surface will result in the indirect maintenance of a large density of small droplets, causing an increased jumping frequency when compared to a no-field surface. Electrically floating the source pin was found experimentally to direct the droplets closer to the GaN transistor than the external guard ring. Since the source pin approach involves electrically floating pins underneath approximately half of the total device surface as shown in Fig. 6-2b, the electric field lines attract all of the droplets directly toward the GaN FET. In contrast, some of the droplets attracted by the external guard ring would have to wick from the guard ring toward the package of the GaN device.

To provide insight into the experimental results and to project the maximum potential of jumping-droplet cooling, we estimated the maximum possible thermal concentration of droplets that could reach a GaN FET using the image processing techniques coupled to previous condensation heat transfer measurements in pure vapor environments.[255] Assuming that all of the departing droplets leave the superhydrophobic surface and reach the GaN device, the maximum jumping-droplet cooling heat flux can be calculated as $q'' = q_c''A_C/A_{GaN}$, where q_c'' is the critical flooding heat flux for CuO superhydrophobic surfaces having conformal hydrophobic polymer coatings (≈ 13 W/cm^2 from h=10000 W/m^2·K & ΔT = 10°C), and A_C is the effective condenser area which is able to provide jumping droplets that move laterally from their jumping location to the GaN device ($A_c = L^2$, where L is the maximum horizontal distance from which jumping droplets will travel to the device). Using more than 10 time lapse images analogous to Figure 6-1d to estimate L during EFE condensation ($A_C \approx 9A_{GaN}$), our analysis suggests that heat fluxes of $q'' \approx 120$W/cm^2 should

be attainable in pure vapor environments for gap spacings of 3 mm and the GaN FET geometries studied here. Our analysis suggests that increasing in the charge per droplet is the most important parameter to obtain enhanced heat flux since the effect of the electric field attrition force and area ratio can be increased ($A_C \sim L^2$). A secondary and more practical approach to increase the hot spot heat flux is to optimize the condenser-to-FET spacing or applied EFE voltage in order to attract more droplets. The experiments conducted here were limited to -100 V due to safety considerations; however, higher applied voltages are possible in closed systems.[243]

The EFE jumping droplet cooling method demonstrated here is similar to but fundamentally different from the jumping-droplet vapor chamber.[245] In the jumping droplet vapor chamber, spatial and temporal control of droplet motion is not possible, whereas in our device, active sensing of hot spots can be used as a feedback to locally direct droplets using electric fields. Furthermore, active application of electric fields may not be necessary, as the EFE concept developed here has future possibility of exploiting the inherent electric fields generated by the high voltage switching action ($\mathrm{d}v/\mathrm{d}t$) from power semiconductor devices to tailor the electric field to provide localized, directed cooling for the power devices. In addition to improved cooling, this effect may also realize a method to better equalize temperatures, a key design challenge for power sharing among parallel-connected devices. In the future, it would be interesting to investigate the performance of the device in pure vapor environments in vacuum due to: (i) the significant condensation thermal resistance added by NCGs, and (ii) the potential for droplet charge dissipation in the presence of NCGs. Indeed, a scaling analysis using previous EFE condensation visualization studies in pure vapor environments[25] indicates that the thermal concentration ratio (A_C/A_{GaN}) can be well over 100 for gap spacing of the same order of magnitude studied here (5 mm), inferring that $q" = q_c" A_C/A_{GaN} \approx 1\mathrm{kW/cm^2}$ can be achieved. Furthermore, future studies should also investigate the

durability of the superhydrophobic surfaces on internal sealed condenser devices, as any practical implementation will require a longevity of years if not decades.[10]

6.3. Conclusion

In summary, we demonstrated jumping-droplet hot spot cooling, whereby charged droplets jump between superhydrophobic copper oxide condensers and electrical circuits to cool local hot devices actively with evaporation. Through experiments and modeling, we demonstrated heat flux dissipations of 1 W/cm^2, which can be improved in the near-term to 120 W/cm^2. Future enclosed devices with pure vapor environments and optimized geometrical designs have the potential to achieve higher active cooling rates approaching 1 kW/cm^2. This work not only demonstrates EFE condensation-based electronics cooling, but also provides a framework for the development of active jumping droplet based vapor chambers and heat pipes capable of spatial and temporal thermal dissipation control.

CHAPTER 7: CONCLUSIONS

This dissertation investigated the enhancement of phase change heat transfer, especially condensation, promoted by the desirable wettability of surface. To better understand the desired wettability that promotes enhanced condensation and means by which it can be achieved, I focused my search to find the answer from nature considering nature itself has evolved over millions of years to optimize life suitable even for harsh and extreme conditions. However, still why and how they have evolved so, and how we can achieve the desired wettability and heat transfer performance have always been debatable. In the series of studies, I first studied the wettability of cicada wings, as to how they achieved durable hydrophobicity on their wings. Contact angle measurements, along with high speed imaging of water vapor condensation revealed the cicada wings have conformal (super)hydrophobicity regardless the location on a wing. The study concluded the wettability difference found from cicada species were affected by their taxonomy possibly related to their life history and complex evolutionary pressure, not simply by habitats and their living environments. In the subsequent study, I attempted to develop environment friendly superhydrophobic coating based on the naturally derived material, not chemically synthesized coatings. Most of the current hydrophobic coatings are based on fluorine-based polymers, which is environmentally toxic. In this study, I fabricated superhydrophobic surface with coating derived from natural extracts of myristica and cinnamon. In the third chapter of this dissertation, I conducted the study to answer to decade long debates in scientific community on wettability of rare earth oxides. I investigated the claims from the previous studies and performed the experiment to verify the intrinsic wettability of rare earth oxide to be hydrophilic. However, these materials are found to be hydrophobic *in-situ* due to hydrocarbon adsorption on the surface. Such rare earth

oxide materials have been utilized as catalysts and durable hydrophobic coatings without exactly knowing what drives hydrophobicity. I believe this study to be of paramount contribution to the scientific community not only by revealing the mechanism of wettability but also suggesting future fundamental studies on wettability of REO and their applications.

Based on the aforementioned fundamental studies on wettability of materials found in nature, I attempted to apply the lessons from them to redesign exixting state-of-the-art surfaces and methods to enhance phase change heat transfer and to implement them in more realistic and industrial engineering applications. In the fifth chapter of this dissertation, I developed the concept of thin film condensation to enhance filmwise condensation heat transfer, making it comparable to the heat transfer attained by dropwise condensation. Nanoporous confined biphilic inverse opal structure was fabricated to maintain the condensate film with a film thickness in the order of few microns. From heat transfer and fluid flow calculations, the thin film condensation was conceptually demonstrated enhancing condensation heat transfer on nanostructured surface. In the final chapter, I studied the active hot spot cooling of electronics using jumping droplet condensation. In ambient atmospheric condition, jumping droplet condensation enhanced the cooling performance of gallium nitride (GaN) transistor for power electronics applications. The study first demonstrated jumping droplets cooling as well as switchability of cooling targets to active hot spots using electric-field enhanced jumping droplets.

To summarize, in this doctoral dissertation, I have considered not only scientific novelty and importance to fundamentals, but also the technical and societal impact stimulating new idea of research and applications. As they say, “We will find a way, we always have”. I hope my study has significant ramification in scientific and technological advancement in paving the way and would help to write the next new chapter in history.

REFERENCES

1. Quante, M. In *The role of clouds in the climate system*, Journal de Physique IV (Proceedings), EDP sciences: 2004; pp 61-86.
2. Cho, H. J.; Preston, D. J.; Zhu, Y.; Wang, E. N., Nanoengineered materials for liquid–vapour phase-change heat transfer. *Nat. Rev. Mater.* **2016,** *2*, 16092.
3. Zalba, B.; Marın, J. M.; Cabeza, L. F.; Mehling, H., Review on thermal energy storage with phase change: materials, heat transfer analysis and applications. *Applied thermal engineering* **2003,** *23* (3), 251-283.
4. Enright, R.; Miljkovic, N.; Alvarado, J. L.; Kim, K.; Rose, J. W., Dropwise Condensation on Micro- and Nanostructured Surfaces. *Nanoscale Microscale Thermophys. Eng.* **2014,** *18* (3), 223-250.
5. Maulbetsch, J. S., Advanced Power Plant Cooling: Reducing water consumption. In *ASME International Mechanical Engineering Congress and Exposition 2012*, Houston, TX, USA, 2012.
6. Miljkovic, N.; Wang, E. N., Condensation heat transfer on superhydrophobic surfaces. *MRS Bull.* **2013,** *38* (5), 397-406.
7. Rose, J. W., Dropwise condensation theory and experiment: A review. *Proc. Inst. Mech. Eng. A J. Power Energy* **2002,** *216* (2), 115-128.
8. Sablowski, J.; Unz, S.; Beckmann, M., Dropwise Condensation on Advanced Functional Surfaces – Theory and Experimental Setup. *Chem. Eng. Technology* **2017,** *40* (11), 1966-1974.
9. Hou, Y.; Yu, M.; Chen, X.; Wang, Z.; Yao, S., Recurrent Filmwise and Dropwise Condensation on a Beetle Mimetic Surface. *ACS Nano* **2015,** *9* (1), 71-81.
10. Parker, A. R.; Lawrence, C. R., Water capture by a desert beetle. *Nature* **2001,** *414* (6859), 33-34.
11. Zhu, H.; Guo, Z., Hybrid engineered materials with high water-collecting efficiency inspired by Namib Desert beetles. *Chem. Commun.* **2016,** *52* (41), 6809-6812.
12. Humplik, T.; Lee, J.; O'Hern, S. C.; Fellman, B. A.; Baig, M. A.; Hassan, S. F.; Atieh, M. A.; Rahman, F.; Laoui, T.; Karnik, R.; Wang, E. N., Nanostructured materials for water desalination. *Nanotechnol.* **2011,** *22* (29), 292001.
13. Khawaji, A. D.; Kutubkhanah, I. K.; Wie, J.-M., Advances in seawater desalination technologies. *Desalination* **2008,** *221* (1), 47-69.
14. Shannon, M. A.; Bohn, P. W.; Elimelech, M.; Georgiadis, J. G.; Mariñas, B. J.; Mayes, A. M., Science and technology for water purification in the coming decades. *Nature* **2008,** *452*, 301.
15. Pérez-Lombard, L.; Ortiz, J.; Pout, C., A review on buildings energy consumption information. *Energy Buildings* **2008,** *40* (3), 394-398.
16. Agency, I. E., World Energy Outlook 2018. Organisation for Economic Co-operation and Development: Paris, 2018. ProQuest Ebook Central - Full text online http://www.library.illinois.edu/proxy/go.php?url=http://ebookcentral.proquest.com/lib/uiuc/detail.action?docID=615983.
17. Dhir, V. K., BOILING HEAT TRANSFER. *Annual Review of Fluid Mechanics* **1998,** *30* (1), 365-401.
18. Kim, D. E.; Yu, D. I.; Jerng, D. W.; Kim, M. H.; Ahn, H. S., Review of boiling heat transfer enhancement on micro/nanostructured surfaces. *Experimental Thermal and Fluid Science* **2015,** *66*, 173-196.

19. Kharangate, C. R.; Mudawar, I., Review of computational studies on boiling and condensation. *International Journal of Heat and Mass Transfer* **2017,** *108*, 1164-1196.
20. Attinger, D.; Frankiewicz, C.; Betz, A. R.; Schutzius, T. M.; Ganguly, R.; Das, A.; Kim, C.-J.; Megaridis, C. M., Surface engineering for phase change heat transfer: A review. *MRS Energy & Sustainability* **2014,** *1*.
21. Rose, J. W., Dropwise condensation theory and experiment: A review. *Proceedings of the Institution of Mechanical Engineers, Part A: Journal of Power and Energy* **2002,** *216* (2), 115-128.
22. Nusselt, W., The surface condensation of water vapor. *Z. Ver. Dtsch. Ing.* **1916,** *60*, 541-546.
23. Schmidt, E.; Schurig, W.; Sellschopp, W., Condensation of water vapour in film-and drop form. *Tech. Mech. Thermodyn.* **1930,** *1*, 53-63.
24. Miljkovic, N.; Enright, R.; Nam, Y.; Lopez, K.; Dou, N.; Sack, J.; Wang, E. N., Jumping-Droplet-Enhanced Condensation on Scalable Superhydrophobic Nanostructured Surfaces. *Nano Lett.* **2013,** *13* (1), 179-187.
25. Miljkovic, N.; Preston, D. J.; Enright, R.; Wang, E. N., Electric-Field-Enhanced Condensation on Superhydrophobic Nanostructured Surfaces. *ACS Nano* **2013,** *7* (12), 11043-11054.
26. Miljkovic, N.; Preston, D. J.; Enright, R.; Wang, E. N., Electrostatic charging of jumping droplets. *Nat. Commun.* **2013,** *4*, 2517.
27. Cha, H.; Xu, C.; Sotelo, J.; Chun, J. M.; Yokoyama, Y.; Enright, R.; Miljkovic, N., Coalescence-induced nanodroplet jumping. *Phys. Rev. Fluids* **2016,** *1* (6), 064102.
28. Enright, R.; Miljkovic, N.; Sprittles, J.; Nolan, K.; Mitchell, R.; Wang, E. N., How Coalescing Droplets Jump. *ACS Nano* **2014,** *8* (10), 10352-10362.
29. Kim, M.-K.; Cha, H.; Birbarah, P.; Chavan, S.; Zhong, C.; Xu, Y.; Miljkovic, N., Enhanced Jumping-Droplet Departure. *Langmuir* **2015,** *31* (49), 13452-13466.
30. Liu, F.; Ghigliotti, G.; Feng, J. J.; Chen, C.-H., Numerical simulations of self-propelled jumping upon drop coalescence on non-wetting surfaces. *J. Fluid Mech.* **2014,** *752*, 39-65.
31. Miljkovic, N.; Enright, R.; Wang, E. N., Growth Dynamics During Dropwise Condensation on Nanostructured Superhydrophobic Surfaces. In *ASME 2012 Third International Conference on Micro/Nanoscale Heat and Mass Transfer*, Atlanta, GA, 2012; pp 427-436.
32. Qu, X.; Boreyko, J. B.; Liu, F.; Agapov, R. L.; Lavrik, N. V.; Retterer, S. T.; Feng, J. J.; Collier, C. P.; Chen, C.-H., Self-propelled sweeping removal of dropwise condensate. *Appl. Phys. Lett.* **2015,** *106* (22), 221601.
33. Boreyko, J. B.; Chen, C.-H., Self-Propelled Dropwise Condensate on Superhydrophobic Surfaces. *Phys. Rev. Lett.* **2009,** *103* (18), 184501.
34. Paxson, A. T.; Yagüe, J. L.; Gleason, K. K.; Varanasi, K. K., Stable Dropwise Condensation for Enhancing Heat Transfer via the Initiated Chemical Vapor Deposition (iCVD) of Grafted Polymer Films. *Adv. Mater.* **2014,** *26* (3), 418-423.
35. Holden, K. M.; Wanniarachchi, A. S.; Marto, P. J.; Boone, D. H.; Rose, J. W., The Use of Organic Coatings to Promote Dropwise Condensation of Steam. *J. Heat Transfer* **1987,** *109* (3), 768-774.
36. Feng, L.; Li, S.; Li, Y.; Li, H.; Zhang, L.; Zhai, J.; Song, Y.; Liu, B.; Jiang, L.; Zhu, D., Super-hydrophobic surfaces: from natural to artificial. *Adv. Mater.* **2002,** *14* (24), 1857-1860.

37. Liu, M.; Wang, S.; Jiang, L., Nature-inspired superwettability systems. *Nat. Rev. Mater.* **2017,** *2*, 17036.
38. Mouterde, T.; Lehoucq, G.; Xavier, S.; Checco, A.; Black, C. T.; Rahman, A.; Midavaine, T.; Clanet, C.; Quere, D., Antifogging abilities of model nanotextures. *Nat. Mater.* **2017,** *16* (6), 658-663.
39. Oh, J.; Dana, C.; Hong, S.; Roman, J. K.; Jo, K. D.; Hong, J. W.; Nguyen, J.; Cropek, D. M.; Alleyne, M.; Miljkovic, N., Exploring the Role of Habitat on the Wettability of Cicada Wings. *ACS Appl. Mater. Interfaces* **2017**.
40. Wisdom, K. M.; Watson, J. A.; Qu, X.; Liu, F.; Watson, G. S.; Chen, C.-H., Self-cleaning of superhydrophobic surfaces by self-propelled jumping condensate. *PNAS* **2013,** *110* (20), 7992-7997.
41. Lai, Y.; Tang, Y.; Gong, J.; Gong, D.; Chi, L.; Lin, C.; Chen, Z., Transparent superhydrophobic/superhydrophilic TiO 2-based coatings for self-cleaning and anti-fogging. *J. Mater. Chem.* **2012,** *22* (15), 7420-7426.
42. Sun, Z.; Liao, T.; Liu, K.; Jiang, L.; Kim, J. H.; Dou, S. X., Fly-Eye Inspired Superhydrophobic Anti-Fogging Inorganic Nanostructures. *Small* **2014,** *10* (15), 3001-3006.
43. Tricoli, A.; Righettoni, M.; Pratsinis, S. E., Anti-fogging nanofibrous SiO2 and nanostructured SiO2− TiO2 films made by rapid flame deposition and in situ annealing. *Langmuir* **2009,** *25* (21), 12578-12584.
44. Barish, J. A.; Goddard, J. M., Anti-fouling surface modified stainless steel for food processing. *Food Bioprod. Process.* **2013,** *91* (4), 352-361.
45. Genzer, J.; Efimenko, K., Recent developments in superhydrophobic surfaces and their relevance to marine fouling: a review. *Biofouling* **2006,** *22* (5), 339-360.
46. Wang, N.; Xiong, D.; Deng, Y.; Shi, Y.; Wang, K., Mechanically robust superhydrophobic steel surface with anti-icing, UV-durability, and corrosion resistance properties. *ACS Appl. Mater. Interfaces* **2015,** *7* (11), 6260-6272.
47. Watson, G. S.; Green, D. W.; Schwarzkopf, L.; Li, X.; Cribb, B. W.; Myhra, S.; Watson, J. A., A gecko skin micro/nano structure–A low adhesion, superhydrophobic, anti-wetting, self-cleaning, biocompatible, antibacterial surface. *Acta Biomater.* **2015,** *21*, 109-122.
48. Wu, M.; Ma, B.; Pan, T.; Chen, S.; Sun, J., Silver-Nanoparticle-Colored Cotton Fabrics with Tunable Colors and Durable Antibacterial and Self-Healing Superhydrophobic Properties. *Adv. Funct. Mater.* **2016,** *26* (4), 569-576.
49. Ivanova, E. P.; Hasan, J.; Webb, H. K.; Truong, V. K.; Watson, G. S.; Watson, J. A.; Baulin, V. A.; Pogodin, S.; Wang, J. Y.; Tobin, M. J.; Lobbe, C.; Crawford, R. J., Natural Bactericidal Surfaces: Mechanical Rupture of Pseudomonas aeruginosa Cells by Cicada Wings. *Small* **2012,** *8* (16), 2489-2494.
50. Pogodin, S.; Hasan, J.; Baulin, Vladimir A.; Webb, Hayden K.; Truong, Vi K.; Phong Nguyen, The H.; Boshkovikj, V.; Fluke, Christopher J.; Watson, Gregory S.; Watson, Jolanta A.; Crawford, Russell J.; Ivanova, Elena P., Biophysical Model of Bacterial Cell Interactions with Nanopatterned Cicada Wing Surfaces. *Biophys J.* **2013,** *104* (4), 835-840.
51. Watson, G. S.; Myhra, S.; Cribb, B. W.; Watson, J. A., Putative functions and functional efficiency of ordered cuticular nanoarrays on insect wings. *Biophys J.* **2008,** *94* (8), 3352-3360.
52. Wisdom, K. M.; Watson, J. A.; Qu, X. P.; Liu, F. J.; Watson, G. S.; Chen, C. H., Self-cleaning of superhydrophobic surfaces by self-propelled jumping condensate. *PNAS* **2013,** *110* (20), 7992-7997.

53. Gao, X.; Yan, X.; Yao, X.; Xu, L.; Zhang, K.; Zhang, J.; Yang, B.; Jiang, L., The dry-style antifogging properties of mosquito compound eyes and artificial analogues prepared by soft lithography. *Adv. Mater.* **2007,** *19* (17), 2213-2217.
54. Kuo, W.-K.; Hsu, J.-J.; Nien, C.-K.; Yu, H. H., Moth-Eye-Inspired Biophotonic Surfaces with Antireflective and Hydrophobic Characteristics. *ACS Appl. Mater. Interfaces* **2016,** *8* (46), 32021-32030.
55. Koch, K.; Barthlott, W., Superhydrophobic and superhydrophilic plant surfaces: an inspiration for biomimetic materials. *Philos. Trans. R. Soc. London, A* **2009,** *367* (1893), 1487.
56. Bhushan, B.; Jung, Y. C.; Koch, K., Self-Cleaning Efficiency of Artificial Superhydrophobic Surfaces. *Langmuir* **2009,** *25* (5), 3240-3248.
57. Liu, K. S.; Jiang, L., Bio-Inspired Self-Cleaning Surfaces. *Annu Rev Mater Res* **2012,** *42*, 231-263.
58. Tan, Y.; Gu, J.; Zang, X.; Xu, W.; Shi, K.; Xu, L.; Zhang, D., Versatile Fabrication of Intact Three-Dimensional Metallic Butterfly Wing Scales with Hierarchical Sub-micrometer Structures. *Angewandte Chemie International Edition* **2011,** *50* (36), 8307-8311.
59. Bixler, G. D.; Bhushan, B., Bioinspired rice leaf and butterfly wing surface structures combining shark skin and lotus effects. *Soft matter* **2012,** *8* (44), 11271-11284.
60. Hong, S. H.; Hwang, J.; Lee, H., Replication of cicada wing's nano-patterns by hot embossing and UV nanoimprinting. *Nanotechnol.* **2009,** *20* (38).
61. Nishimoto, S.; Bhushan, B., Bioinspired self-cleaning surfaces with superhydrophobicity, superoleophobicity, and superhydrophilicity. *RSC Adv.* **2013,** *3* (3), 671-690.
62. Hasan, J.; Webb, H. K.; Truong, V. K.; Watson, G. S.; Watson, J. A.; Tobin, M. J.; Gervinskas, G.; Juodkazis, S.; Wang, J. Y.; Crawford, R. J.; Ivanova, E. P., Spatial Variations and Temporal Metastability of the Self-Cleaning and Superhydrophobic Properties of Damselfly Wings. *Langmuir* **2012,** *28* (50), 17404-17409.
63. Han, Z. W.; Mu, Z. Z.; Li, B.; Niu, S. C.; Zhang, J. Q.; Ren, L. Q., A High-Transmission, Multiple Antireflective Surface Inspired from Bilayer 3D Ultrafine Hierarchical Structures in Butterfly Wing Scales. *Small* **2016,** *12* (6), 713-720.
64. Sun, M. X.; Liang, A. P.; Zheng, Y. M.; Watson, G. S.; Watson, J. A., A study of the anti-reflection efficiency of natural nano-arrays of varying sizes. *Bioinspir Biomim* **2011,** *6* (2).
65. Watson, G. S.; Watson, J. A.; Hu, S.; Brown, C. L.; Cribb, B.; Myhra, S., Micro and nanostructures found on insect wings – designs for minimising adhesion and friction. *Int. J. Nanomanf.* **2010,** *5* (1-2), 112-128.
66. Hu, H. M.; Watson, J. A.; Cribb, B. W.; Watson, G. S., Fouling of nanostructured insect cuticle: adhesion of natural and artificial contaminants. *Biofouling* **2011,** *27* (10), 1125-1137.
67. Kelleher, S. M.; Habimana, O.; Lawler, J.; O'Reilly, B.; Daniels, S.; Casey, E.; Cowley, A., Cicada Wing Surface Topography: An Investigation into the Bactericidal Properties of Nanostructural Features. *ACS Appl. Mater. Interfaces* **2016,** *8* (24), 14966-14974.
68. Bandara, C. D.; Singh, S.; Afara, I. O.; Wolff, A.; Tesfamichael, T.; Ostrikov, K.; Oloyede, A., Bactericidal Effects of Natural Nanotopography of Dragonfly Wing on Escherichia coli. *ACS Appl. Mater. Interfaces* **2017,** *9* (8), 6746-6760.
69. Fang, Y.; Sun, G.; Wang, T. Q.; Cong, Q.; Ren, L. Q., Hydrophobicity mechanism of non-smooth pattern on surface of butterfly wing. *Chinese Sci Bull* **2007,** *52* (5), 711-716.
70. Byun, D.; Hong, J.; Saputra; Ko, J. H.; Lee, Y. J.; Park, H. C.; Byun, B. K.; Lukes, J. R., Wetting Characteristics of Insect Wing Surfaces. *J Bionic Eng* **2009,** *6* (1), 63-70.

71. Hamilton, W. J.; Seely, M. K., Fog Basking by Namib Desert Beetle, Onymacris-Unguicularis. *Nature* **1976,** *262* (5566), 284-285.
72. Park, K. C.; Kim, P.; Grinthal, A.; He, N.; Fox, D.; Weaver, J. C.; Aizenberg, J., Condensation on slippery asymmetric bumps. *Nature* **2016,** *531* (7592), 78-82.
73. Schmidt, E.; Schurig, W.; Sellschopp, W., Versuche über die Kondensation von Wasserdampf in Film- und Tropfenform (Condensation of Water Vapour in Film- and Drop Form). *Tech. Mech. Thermodyn.* **1930,** *1* (2), 53-63.
74. Rose, J. W., Dropwise condensation theory and experiment: A review. *Proc. Inst. Mech. Eng., Part A* **2002,** *216* (2), 115-128.
75. Fürstner, R.; Barthlott, W.; Neinhuis, C.; Walzel, P., Wetting and Self-Cleaning Properties of Artificial Superhydrophobic Surfaces. *Langmuir* **2005,** *21* (3), 956-961.
76. Nakajima, A.; Hashimoto, K.; Watanabe, T.; Takai, K.; Yamauchi, G.; Fujishima, A., Transparent Superhydrophobic Thin Films with Self-Cleaning Properties. *Langmuir* **2000,** *16* (17), 7044-7047.
77. Boreyko, J. B.; Zhao, Y.; Chen, C.-H., Planar jumping-drop thermal diodes. *Appl. Phys. Lett.* **2011,** *99* (23), 234105.
78. Boreyko, J. B.; Chen, C.-H., Vapor chambers with jumping-drop liquid return from superhydrophobic condensers. *Int. J. Heat Mass Transfer* **2013,** *61*, 409-418.
79. Miljkovic, N.; Preston, D. J.; Enright, R.; Wang, E. N., Jumping-droplet electrostatic energy harvesting. *Appl. Phys. Lett.* **2014,** *105* (1), 013111.
80. Oh, J.; Birbarah, P.; Foulkes, T.; Yin, S. L.; Rentauskas, M.; Neely, J.; Pilawa-Podgurski, R. C. N.; Miljkovic, N., Jumping-droplet electronics hot-spot cooling. *Appl. Phys. Lett.* **2017,** *110* (12), 123107.
81. Boreyko, J. B.; Chen, C. H., Self-propelled dropwise condensate on superhydrophobic surfaces. *Phys. Rev. Lett.* **2009,** *103* (18), 184501.
82. Say, T., *Descriptions of New Hemipterous Insects, Collected in the Expedition to the Rocky Mountains, Performed by Order of Mr. Calhoun, Secretary of War, Under Command of Major Long: Read 1824*. 1825.
83. Linnaeus, C., *Systema naturæ per regna tria naturæ, secundum classes, ordines, genera, species, cum characteribus, differentiis, synonymis, locis. Tomus I. Editio decima, reformata*. 10th ed.; Laurentius Salvius: Stockholm, 1758; p 824.
84. Sanborn, A.; Phillips, P., Biogeography of the Cicadas (Hemiptera: Cicadidae) of North America, North of Mexico. *Diversity* **2013,** *5* (2), 166.
85. Davis, W. T., Mississippi cicadas, with a key to the species of the southeastern United States. *J. N. Y. Entomol. Soc.* **1918,** *26* (3/4), 141-155.
86. Moulds, M. S., An appraisal of the higher classification of cicadas (Hemiptera : Cicadoidea) with special reference to the Australian fauna. *Rec Aust Mus* **2005,** *57* (3), 375-446.
87. Necas, D.; Klapetek, P., Gwyddion: an open-source software for SPM data analysis. *Cent Eur J Phys* **2012,** *10* (1), 181-188.
88. Cha, H.; Chun, J. M.; Sotelo, J.; Miljkovic, N., Focal Plane Shift Imaging for the Analysis of Dynamic Wetting Processes. *ACS Nano* **2016,** *10* (9), 8223-8232.
89. Schneider, C. A.; Rasband, W. S.; Eliceiri, K. W., NIH Image to ImageJ: 25 years of image analysis. *Nat Methods* **2012,** *9* (7), 671-675.

90. Santos, S.; Barcons, V.; Christenson, H. K.; Font, J.; Thomson, N. H., The Intrinsic Resolution Limit in the Atomic Force Microscope: Implications for Heights of Nano-Scale Features. *PLoS One* **2011,** *6* (8), e23821.
91. Watson, G. S.; Myhra, S.; Cribb, B. W.; Watson, J. A., Imaging and investigation of function(s) and efficiency of ordered cuticular nanostructures. In *Nanoscale Structure and Properties of Microbial Cell Surfaces*, Ivanova, E. P., Ed. New York Nova Science Publishers, 2006; pp 175–198.
92. Sun, M.; Watson, G. S.; Zheng, Y.; Watson, J. A.; Liang, A., Wetting properties on nanostructured surfaces of cicada wings. *J. Exp. Biol.* **2009,** *212* (19), 3148-3155.
93. Zheng, Y.; Gao, X.; Jiang, L., Directional adhesion of superhydrophobic butterfly wings. *Soft Matter* **2007,** *3* (2), 178-182.
94. Barthlott, W.; Neinhuis, C., Purity of the sacred lotus, or escape from contamination in biological surfaces. *Planta* **1997,** *202* (1), 1-8.
95. Koch, K.; Ensikat, H.-J., The hydrophobic coatings of plant surfaces: Epicuticular wax crystals and their morphologies, crystallinity and molecular self-assembly. *Micron* **2008,** *39* (7), 759-772.
96. Nguyen, S. H. T.; Webb, H. K.; Hasan, J.; Tobin, M. J.; Crawford, R. J.; Ivanova, E. P., Dual role of outer epicuticular lipids in determining the wettability of dragonfly wings. *Colloids Surf., B* **2013,** *106*, 126-134.
97. Tuteja, A.; Choi, W. J.; McKinley, G. H.; Cohen, R. E.; Rubner, M. F., Design parameters for superhydrophobicity and superoleophobicity. *MRS Bull.* **2008,** *33* (8), 752-758.
98. Frankiewicz, C.; Attinger, D., Texture and wettability of metallic lotus leaves. *Nanoscale* **2016,** *8* (7), 3982-3990.
99. Gao, X.; Jiang, L., Biophysics: Water-repellent legs of water striders. *Nature* **2004,** *432* (7013), 36-36.
100. Tong, J.; Sun, J.; Chen, D.; Zhang, S., Geometrical features and wettability of dung beetles and potential biomimetic engineering applications in tillage implements. *Soil Tillage Res.* **2005,** *80* (1–2), 1-12.
101. Enright, R.; Miljkovic, N.; Dou, N.; Nam, Y.; Wang, E. N., Condensation on Superhydrophobic Copper Oxide Nanostructures. *J. Heat Transfer* **2013,** *135* (9), 091304-091304-12.
102. Enright, R.; Miljkovic, N.; Al-Obeidi, A.; Thompson, C. V.; Wang, E. N., Condensation on superhydrophobic surfaces: The role of local energy barriers and structure length scale. *Langmuir* **2012,** *28* (40), 14424-14432.
103. Miljkovic, N.; Enright, R.; Wang, E. N., Effect of droplet morphology on growth dynamics and heat transfer during condensation on superhydrophobic nanostructured surfaces. *ACS Nano* **2012,** *6* (2), 1776-1785.
104. Miljkovic, N.; Enright, R.; Wang, E. N. In *Growth dynamics during dropwise condensation on nanostructured superhydrophobic surfaces*, ASME 2012 Third International Conference on Micro/Nanoscale Heat and Mass Transfer, American Society of Mechanical Engineers: 2012; pp 427-436.
105. Williams, K. S.; Simon, C., The Ecology, Behavior, and Evolution of Periodical Cicadas. *Annu Rev Entomol* **1995,** *40*, 269-295.

106. Sun, M.; Liang, A.; Watson, G. S.; Watson, J. A.; Zheng, Y.; Ju, J.; Jiang, L., Influence of cuticle nanostructuring on the wetting behaviour/states on cicada wings. *PLoS One* **2012,** *7* (4), e35056.
107. Patek, S. N., Biomimetics and evolution. *Science* **2014,** *345* (6203), 1448-1449.
108. Lei, H.; Xiao, J.; Zheng, L.; Xiong, M.; Zhu, Y.; Qian, J.; Zhuang, Q.; Han, Z., Superhydrophobic coatings based on colloid silica and fluorocopolymer. *Polymer* **2016,** *86*, 22-31.
109. Zhou, S.; Liu, P.; Wang, M.; Zhao, H.; Yang, J.; Xu, F., Sustainable, Reusable, and Superhydrophobic Aerogels from Microfibrillated Cellulose for Highly Effective Oil/Water Separation. *ACS Sustainable Chem. Eng.* **2016,** *4* (12), 6409-6416.
110. Huang, S.; Zhang, Y.; Shi, J.; Huang, W., Superhydrophobic particles derived from nature-inspired polyphenol chemistry for liquid marble formation and oil spills treatment. *ACS Sustainable Chem. Eng.* **2016,** *4* (3), 676-681.
111. Sova, M., Antioxidant and Antimicrobial Activities of Cinnamic Acid Derivatives. *Mini-Rev. Med. Chem.* **2012,** *12* (8), 749-767.
112. Isimjan, T. T.; Wang, T.; Rohani, S., A novel method to prepare superhydrophobic, UV resistance and anti-corrosion steel surface. *Chem. Eng. J.* **2012,** *210*, 182-187.
113. Zhang, F.; Zhao, L.; Chen, H.; Xu, S.; Evans, D. G.; Duan, X., Corrosion resistance of superhydrophobic layered double hydroxide films on aluminum. *Angew. Chem. Int. Ed.* **2008,** *47* (13), 2466-2469.
114. Wang, Z.; Su, Y.; Li, Q.; Liu, Y.; She, Z.; Chen, F.; Li, L.; Zhang, X.; Zhang, P., Researching a highly anti-corrosion superhydrophobic film fabricated on AZ91D magnesium alloy and its anti-bacteria adhesion effect. *Mater. Charact.* **2015,** *99*, 200-209.
115. Wang, Y.; Xue, J.; Wang, Q.; Chen, Q.; Ding, J., Verification of icephobic/anti-icing properties of a superhydrophobic surface. *ACS Appl. Mater. Interfaces* **2013,** *5* (8), 3370-3381.
116. Tang, Y.; Zhang, Q.; Zhan, X.; Chen, F., Superhydrophobic and anti-icing properties at overcooled temperature of a fluorinated hybrid surface prepared via a sol–gel process. *Soft Matter* **2015,** *11* (22), 4540-4550.
117. Yoon, D.; Lee, C.; Yun, J.; Jeon, W.; Cha, B. J.; Baik, S., Enhanced condensation, agglomeration, and rejection of water vapor by superhydrophobic aligned multiwalled carbon nanotube membranes. *ACS Nano* **2012,** *6* (7), 5980-5987.
118. Choi, D.; Lee, S.; Park, S. M.; Cho, H.; Hwang, W.; Kim, D. S., Energy harvesting model of moving water inside a tubular system and its application of a stick-type compact triboelectric nanogenerator. *Nano Res.* **2015,** *8* (8), 2481.
119. Lin, Z. H.; Cheng, G.; Lee, S.; Pradel, K. C.; Wang, Z. L., Harvesting Water Drop Energy by a Sequential Contact-Electrification and Electrostatic-Induction Process. *Adv. Mater.* **2014,** *26* (27), 4690-4696.
120. Daniello, R. J.; Waterhouse, N. E.; Rothstein, J. P., Drag reduction in turbulent flows over superhydrophobic surfaces. *Phys. Fluids* **2009,** *21* (8), 085103.
121. McHale, G.; Newton, M. I.; Shirtcliffe, N. J., Immersed superhydrophobic surfaces: Gas exchange, slip and drag reduction properties. *Soft Matter* **2010,** *6* (4), 714-719.
122. Shirtcliffe, N. J.; McHale, G.; Newton, M. I.; Zhang, Y., Superhydrophobic copper tubes with possible flow enhancement and drag reduction. *ACS Appl. Mater. Interfaces* **2009,** *1* (6), 1316-1323.

123. Chen, X.; Gong, Y.; Li, D.; Li, H., Robust and easy-repairable superhydrophobic surfaces with multiple length-scale topography constructed by thermal spray route. *Colloids and Surfaces A: Physicochemical and Engineering Aspects* **2016,** *492*, 19-25.
124. Lu, X.; Li, H.; Li, H.; Li, T., In situ preparation of recoverable superhydrophobic coatings for various environments. *Journal of Adhesion Science and Technology* **2016,** *30* (10), 1059-1071.
125. Bai, N.; Li, Q.; Dong, H.; Tan, C.; Cai, P.; Xu, L., A versatile approach for preparing self-recovering superhydrophobic coatings. *Chem. Eng. J.* **2016,** *293*, 75-81.
126. Li, Y.; Men, X.; Zhu, X.; Ge, B.; Chu, F.; Zhang, Z., One-step spraying to fabricate nonfluorinated superhydrophobic coatings with high transparency. *J. Mater. Sci.* **2016,** *51* (5), 2411-2419.
127. Xu, W.; Liu, H.; Lu, S.; Xi, J.; Wang, Y., Fabrication of superhydrophobic surfaces with hierarchical structure through a solution-immersion process on copper and galvanized iron substrates. *Langmuir* **2008,** *24* (19), 10895-10900.
128. Kim, D.; Hwang, W.; Park, H.; Lee, K.-H., Superhydrophobic nanostructures based on porous alumina. *Curr. Appl. Phys.* **2008,** *8* (6), 770-773.
129. Gonçalves, G.; Marques, P. A.; Trindade, T.; Neto, C. P.; Gandini, A., Superhydrophobic cellulose nanocomposites. *J. Colloid Interface Sci.* **2008,** *324* (1), 42-46.
130. Arkles, B., *Silane Coupling Agents: Connecting Across Boundaries*. 2014.
131. Lu, Y.; Song, J.; Liu, X.; Xu, W.; Xing, Y.; Wei, Z., Preparation of superoleophobic and superhydrophobic titanium surfaces via an environmentally friendly electrochemical etching method. *ACS Sustainable Chem. Eng.* **2012,** *1* (1), 102-109.
132. Li, Z.; Xing, Y.; Dai, J., Superhydrophobic surfaces prepared from water glass and non-fluorinated alkylsilane on cotton substrates. *Appl. Surf. Sci.* **2008,** *254* (7), 2131-2135.
133. Roe, B. G. Durable non-fluorine water-repellent fabric finishing: surface treatment using silica nanoparticulates and mixed silanes. North Carolina State University, 2009.
134. Lewandowski, G.; Meissner, E.; Milchert, E., Special applications of fluorinated organic compounds. *J. Hazard. Mater.* **2006,** *136* (3), 385-391.
135. Darmanin, T.; Guittard, F., Superoleophobic surfaces with short fluorinated chains? *Soft Matter* **2013,** *9* (25), 5982-5990.
136. Wang, Y.; Wang, W.; Zhong, L.; Wang, J.; Jiang, Q.; Guo, X., Super-hydrophobic surface on pure magnesium substrate by wet chemical method. *Appl. Surf. Sci.* **2010,** *256* (12), 3837-3840.
137. Nečas, D.; Klapetek, P., Gwyddion: an open-source software for SPM data analysis. *Open Physics* **2012,** *10* (1), 181-188.
138. Krauter, P.; Nothelfer, S.; Bodenschatz, N.; Simon, E.; Stocker, S.; Foschum, F.; Kienle, A., Optical phantoms with adjustable subdiffusive scattering parameters. *J. Biomed. Opt.* **2015,** *20* (10), 105008-105008.
139. Commission, E. P.; Medicines, E. D. f. t. Q. o.; Healthcare, *European pharmacopoeia*. 7th ed.; EDQM Council of Europe: Strasbourg, France, 2010; Vol. 1.
140. Gao, L.; Lemarchand, F.; Lequime, M., Refractive index determination of SiO2 layer in the UV/Vis/NIR range: spectrophotometric reverse engineering on single and bi-layer designs. *J. Europ. Opt. Soc. Rap. Public.* **2013,** *8*.
141. Green, M. A., Self-consistent optical parameters of intrinsic silicon at 300K including temperature coefficients. *Sol. Energy Mater. Sol. Cells* **2008,** *92* (11), 1305-1310.

142. Qing, Y.; Hu, C.; Yang, C.; An, K.; Tang, F.; Tan, J.; Liu, C., Rough Structure of Electrodeposition as a Template for an Ultrarobust Self-Cleaning Surface. *ACS Appl. Mater. Interfaces* **2017,** *9* (19), 16571-16580.
143. Ölçeroğlu, E.; McCarthy, M., Self-Organization of Microscale Condensate for Delayed Flooding of Nanostructured Superhydrophobic Surfaces. *ACS Appl. Mater. Interfaces* **2016,** *8* (8), 5729-5736.
144. Mulroe, M. D.; Srijanto, B. R.; Ahmadi, S. F.; Collier, C. P.; Boreyko, J. B., Tuning Superhydrophobic Nanostructures To Enhance Jumping-Droplet Condensation. *ACS Nano* **2017,** *11* (8), 8499-8510.
145. Wen, R.; Lan, Z.; Peng, B.; Xu, W.; Yang, R.; Ma, X., Wetting Transition of Condensed Droplets on Nanostructured Superhydrophobic Surfaces: Coordination of Surface Properties and Condensing Conditions. *ACS Appl. Mater. Interfaces* **2017,** *9* (15), 13770-13777.
146. Lundy, R.; Byrne, C.; Bogan, J.; Nolan, K.; Collins, M. N.; Dalton, E.; Enright, R., Exploring the Role of Adsorption and Surface State on the Hydrophobicity of Rare Earth Oxides. *ACS Appl. Mater. Interfaces* **2017,** *9* (15), 13751-13760.
147. Vigil, G.; Xu, Z.; Steinberg, S.; Israelachvili, J., Interactions of Silica Surfaces. *J. Colloid Interface Sci.* **1994,** *165* (2), 367-385.
148. Boreyko, J. B.; Chen, C.-H., Self-propelled jumping drops on superhydrophobic surfaces. *Phys. Fluids* **2010,** *22* (9), 091110.
149. Rykaczewski, K., Microdroplet Growth Mechanism during Water Condensation on Superhydrophobic Surfaces. *Langmuir* **2012,** *28* (20), 7720-7729.
150. Rykaczewski, K.; Osborn, W. A.; Chinn, J.; Walker, M. L.; Scott, J. H. J.; Jones, W.; Hao, C.; Yao, S.; Wang, Z., How nanorough is rough enough to make a surface superhydrophobic during water condensation? *Soft Matter* **2012,** *8* (33), 8786-8794.
151. Rykaczewski, K.; Scott, J. H. J., Methodology for Imaging Nano-to-Microscale Water Condensation Dynamics on Complex Nanostructures. *ACS Nano* **2011,** *5* (7), 5962-5968.
152. Agoramoorthy, G.; Chandrasekaran, M.; Venkatesalu, V.; Hsu, M. J., Antibacterial and antifungal activities of fatty acid methyl esters of the blind-your-eye mangrove from India. *Braz. J. Microbiol.* **2007,** *38*, 739-742.
153. Narasimhan, B.; Belsare, D.; Pharande, D.; Mourya, V.; Dhake, A., Esters, amides and substituted derivatives of cinnamic acid: synthesis, antimicrobial activity and QSAR investigations. *Eur. J. Med. Chem.* **2004,** *39* (10), 827-834.
154. Narasimhan, B.; Mourya, V.; Dhake, A., Design, synthesis, antibacterial, and QSAR studies of myristic acid derivatives. *Bioorg. Med. Chem. Lett.* **2006,** *16* (11), 3023-3029.
155. Wang, W.; Lockwood, K.; Boyd, L. M.; Davidson, M. D.; Movafaghi, S.; Vahabi, H.; Khetani, S. R.; Kota, A. K., Superhydrophobic Coatings with Edible Materials. *ACS Appl. Mater. Interfaces* **2016,** *8* (29), 18664-18668.
156. Hoque, E.; DeRose, J.; Bhushan, B.; Hipps, K., Low adhesion, non-wetting phosphonate self-assembled monolayer films formed on copper oxide surfaces. *Ultramicroscopy* **2009,** *109* (8), 1015-1022.
157. Smith, T., The hydrophilic nature of a clean gold surface. *Journal of Colloid and Interface Science* **1980,** *75* (1), 51-55.
158. Gardner, J. R.; Woods, R., The hydrophilic nature of gold and platinum. *Journal of Electroanalytical Chemistry and Interfacial Electrochemistry* **1977,** *81* (2), 285-290.
159. Erb, R. A., Dropwise condensation on gold. *Gold Bulletin* **1973,** *6* (1), 2-6.

160. Sattler, J. J. H. B.; Ruiz-Martinez, J.; Santillan-Jimenez, E.; Weckhuysen, B. M., Catalytic Dehydrogenation of Light Alkanes on Metals and Metal Oxides. *Chemical Reviews* **2014,** *114* (20), 10613-10653.
161. Goonan, T. G., *Rare earth elements: End use and recyclability*. US Department of the Interior, US Geological Survey Reston: 2011.
162. Hussein, G. A. M., Rare earth metal oxides: formation, characterization and catalytic activity Thermoanalytical and applied pyrolysis review. *Journal of Analytical and Applied Pyrolysis* **1996,** *37* (2), 111-149.
163. Trovarelli, A.; de Leitenburg, C.; Boaro, M.; Dolcetti, G., The utilization of ceria in industrial catalysis. *Catalysis Today* **1999,** *50* (2), 353-367.
164. Sugimoto, S., Current status and recent topics of rare-earth permanent magnets. *Journal of Physics D: Applied Physics* **2011,** *44* (6), 064001.
165. Kakushima, K.; Tsutsui, K.; Ohmi, S.-I.; Ahmet, P.; Rao, V. R.; Iwai, H., Rare Earth Oxides in Microelectronics. In *Rare Earth Oxide Thin Films*, Fanciulli, M.; Scarel, G., Eds. Springer Berlin Heidelberg: Berlin, Heidelberg, 2007; pp 345-365.
166. Azimi, G.; Dhiman, R.; Kwon, H.-M.; Paxson, A. T.; Varanasi, K. K., Hydrophobicity of rare-earth oxide ceramics. *Nature Materials* **2013,** *12*, 315.
167. Preston, D. J.; Miljkovic, N.; Sack, J.; Enright, R.; Queeney, J.; Wang, E. N., Effect of hydrocarbon adsorption on the wettability of rare earth oxide ceramics. *Applied Physics Letters* **2014,** *105* (1), 011601.
168. Khan, S.; Azimi, G.; Yildiz, B.; Varanasi, K. K., Role of surface oxygen-to-metal ratio on the wettability of rare-earth oxides. *Applied Physics Letters* **2015,** *106* (6), 061601.
169. Carchini, G.; García-Melchor, M.; Łodziana, Z.; López, N., Understanding and Tuning the Intrinsic Hydrophobicity of Rare-Earth Oxides: A DFT+U Study. *ACS Applied Materials & Interfaces* **2016,** *8* (1), 152-160.
170. Fronzi, M.; Assadi, M. H. N.; Hanaor, D. A. H., Theoretical insights into the hydrophobicity of low index CeO2 surfaces. *Applied Surface Science* **2019,** *478*, 68-74.
171. Külah, E.; Marot, L.; Steiner, R.; Romanyuk, A.; Jung, T. A.; Wäckerlin, A.; Meyer, E., Surface chemistry of rare-earth oxide surfaces at ambient conditions: reactions with water and hydrocarbons. *Scientific Reports* **2017,** *7*, 43369.
172. Lundy, R.; Byrne, C.; Bogan, J.; Nolan, K.; Collins, M. N.; Dalton, E.; Enright, R., Exploring the Role of Adsorption and Surface State on the Hydrophobicity of Rare Earth Oxides. *ACS Applied Materials & Interfaces* **2017,** *9* (15), 13751-13760.
173. Oh, I.-K.; Kim, K.; Lee, Z.; Ko, K. Y.; Lee, C.-W.; Lee, S. J.; Myung, J. M.; Lansalot-Matras, C.; Noh, W.; Dussarrat, C.; Kim, H.; Lee, H.-B.-R., Hydrophobicity of Rare Earth Oxides Grown by Atomic Layer Deposition. *Chemistry of Materials* **2015,** *27* (1), 148-156.
174. Xu, P.; Coyle, T. W.; Pershin, L.; Mostaghimi, J., Superhydrophobic ceramic coating: Fabrication by solution precursor plasma spray and investigation of wetting behavior. *Journal of Colloid and Interface Science* **2018,** *523*, 35-44.
175. Xu, P.; Pershin, L.; Mostaghimi, J.; Coyle, T. W., Efficient one-step fabrication of ceramic superhydrophobic coatings by solution precursor plasma spray. *Materials Letters* **2018,** *211*, 24-27.
176. Xu, P.; Coyle, T. W.; Pershin, L.; Mostaghimi, J., Fabrication of micro-/nano-structured superhydrophobic ceramic coating with reversible wettability via a novel solution precursor vacuum plasma spray process. *Materials & Design* **2018,** *160*, 974-984.

177. Mullins, D. R., The surface chemistry of cerium oxide. *Surface Science Reports* **2015,** *70* (1), 42-85.
178. Paparazzo, E., Use and mis-use of x-ray photoemission spectroscopy Ce3d spectra of Ce2O3 and CeO2. *Journal of Physics: Condensed Matter* **2018,** *30* (34), 343003.
179. Wetterer, S. M., Helium atom reflectivity study of physisorption and chemisorption on single crystal metal surfaces. **1998**.
180. Paxson, A. T.; Yagüe, J. L.; Gleason, K. K.; Varanasi, K. K., Stable Dropwise Condensation for Enhancing Heat Transfer via the Initiated Chemical Vapor Deposition (iCVD) of Grafted Polymer Films. *Advanced Materials* **2014,** *26* (3), 418-423.
181. Wang, H.; Xue, Y.; Ding, J.; Feng, L.; Wang, X.; Lin, T., Durable, Self-Healing Superhydrophobic and Superoleophobic Surfaces from Fluorinated-Decyl Polyhedral Oligomeric Silsesquioxane and Hydrolyzed Fluorinated Alkyl Silane. *Angewandte Chemie International Edition* **2011,** *50* (48), 11433-11436.
182. Montemor, M. F., Functional and smart coatings for corrosion protection: A review of recent advances. *Surface and Coatings Technology* **2014,** *258*, 17-37.
183. Zhou, Q.; Zhou, D.; Wu, Y.; Wu, T., Oxidative dehydrogenation of ethane over RE-NiO (RE=La, Nd, Sm, Gd) catalysts. *Journal of Rare Earths* **2013,** *31* (7), 669-673.
184. Sablowski, J.; Unz, S.; Beckmann, M., Dropwise Condensation on Advanced Functional Surfaces – Theory and Experimental Set-Up. *Chem. Eng. Tech.* **2017,** *40* (11), 1966–1974.
185. Cho, H. J.; Preston, D. J.; Zhu, Y.; Wang, E. N., Nanoengineered materials for liquid–vapour phase-change heat transfer. **2016,** *2*, 16092.
186. Attinger, D.; Frankiewicz, C.; Betz, A. R.; Schutzius, T. M.; Ganguly, R.; Das, A.; Kim, C.-J.; Megaridis, C. M., *Surface engineering for phase change heat transfer: A review*. 11/20 ed.; Cambridge University Press: 2014; Vol. 1.
187. Foulkes, T.; Oh, J.; Birbarah, P.; Neely, J.; Miljkovic, N.; Pilawa-Podgurski, R. C. N. In *Active hot spot cooling of GaN transistors with electric field enhanced jumping droplet condensation*, IEEE Applied Power Electronics Conference and Exposition (APEC), Tampa, FL, 26-30 March 2017; Tampa, FL, 2017; pp 912-918.
188. Wiedenheft, K. F.; Guo, H. A.; Qu, X.; Boreyko, J. B.; Liu, F.; Zhang, K.; Eid, F.; Choudhury, A.; Li, Z.; Chen, C.-H., Hotspot cooling with jumping-drop vapor chambers. *Appl. Phys. Lett.* **2017,** *110* (14), 141601.
189. Ölçeroğlu, E.; Hsieh, C.-Y.; Lau, K. K. S.; McCarthy, M., Thin Film Condensation Supported on Ambiphilic Microstructures. *J. Heat Transfer* **2017,** *139* (2), 020910-020910-1.
190. Kawka, P. A.; Buckius, R. O., Optical Properties of Polyimide Films in the Infrared. *Int. J. Thermophys.* **2001,** *22* (2), 517-534.
191. Gao, L.; Lemarchand, F.; Lequime, M., Refractive index determination of SiO2 layer in the UV/Vis/NIR range: spectrophotometric reverse engineering on single and bi-layer designs. *J. Eur. Opt. Soc. Rapid Pub.* **2013,** *8*.
192. Green, M. A., Self-consistent optical parameters of intrinsic silicon at 300K including temperature coefficients. *Solar Energy Mater. Solar Cells* **2008,** *92* (11), 1305-1310.
193. Zhang, H.; Yu, X.; Braun, P. V., Three-dimensional bicontinuous ultrafast-charge and -discharge bulk battery electrodes. *Nat. Nanotechnol.* **2011,** *6* (5), 277-281.
194. Hurley, M. J.; Gottuk, D. T.; Hall Jr, J. R.; Harada, K.; Kuligowski, E. D.; Puchovsky, M.; Watts Jr, J. M.; Wieczorek, C. J., *SFPE Handbook of fire protection engineering*. Springer: New York, NY, 2015.

195. Kashchiev, D., *Nucleation: Basic Theory With Applications*. Butterworth-Heinemann: Oxford, UK, 2000.
196. Cha, H.; Wu, A.; Kim, M.-K.; Saigusa, K.; Liu, A.; Miljkovic, N., Nanoscale-Agglomerate-Mediated Heterogeneous Nucleation. *Nano Lett.* **2017**, submitted for publication.
197. Cao, P.; Xu, K.; Varghese, J. O.; Heath, J. R., The Microscopic Structure of Adsorbed Water on Hydrophobic Surfaces under Ambient Conditions. *Nano Lett.* **2011,** *11* (12), 5581-5586.
198. Lopez, G.; Biebuyck, H.; Frisbie, C.; Whitesides, G., Imaging of features on surfaces by condensation figures. *Science* **1993,** *260* (5108), 647-649.
199. Love, J. C.; Estroff, L. A.; Kriebel, J. K.; Nuzzo, R. G.; Whitesides, G. M., Self-Assembled Monolayers of Thiolates on Metals as a Form of Nanotechnology. *Chem. Rev.* **2005,** *105* (4), 1103-1170.
200. Mandler, D.; Turyan, I., Applications of self-assembled monolayers in electroanalytical chemistry. *Electroanalysis* **1996,** *8* (3), 207-213.
201. Anderson, D. M.; Gupta, M. K.; Voevodin, A. A.; Hunter, C. N.; Putnam, S. A.; Tsukruk, V. V.; Fedorov, A. G., Using Amphiphilic Nanostructures To Enable Long-Range Ensemble Coalescence and Surface Rejuvenation in Dropwise Condensation. *ACS Nano* **2012,** *6* (4), 3262-3268.
202. Thoroddsen, S. T.; Takehara, K.; Etoh, T. G., The coalescence speed of a pendent and a sessile drop. *J. Fluid Mech.* **2005,** *527*, 85-114.
203. Paulsen, J. D.; Burton, J. C.; Nagel, S. R.; Appathurai, S.; Harris, M. T.; Basaran, O. A., The inexorable resistance of inertia determines the initial regime of drop coalescence. *PNAS* **2012,** *109* (18), 6857-6861.
204. Wu, M.; Cubaud, T.; Ho, C.-M., Scaling law in liquid drop coalescence driven by surface tension. *Phys,. Fluids* **2004,** *16* (7), L51-L54.
205. Paulsen, J. D.; Burton, J. C.; Nagel, S. R., Viscous to Inertial Crossover in Liquid Drop Coalescence. *Phys. Rev. Lett.* **2011,** *106* (11), 114501.
206. Pham, Q. N.; Barako, M. T.; Tice, J.; Won, Y., Microscale Liquid Transport in Polycrystalline Inverse Opals across Grain Boundaries. *Sci. Rep.* **2017,** *7* (1), 10465.
207. Tuteja, A.; Choi, W.; Ma, M.; Mabry, J. M.; Mazzella, S. A.; Rutledge, G. C.; McKinley, G. H.; Cohen, R. E., Designing Superoleophobic Surfaces. *Science* **2007,** *318* (5856), 1618.
208. Bodla, K. K.; Murthy, J. Y.; Garimella, S. V., Direct Simulation of Thermal Transport Through Sintered Wick Microstructures. *J. Heat Transfer* **2011,** *134* (1), 012602-012602-10.
209. Dominguez Espinosa, F. A.; Peters, T. B.; Brisson, J. G., Effect of fabrication parameters on the thermophysical properties of sintered wicks for heat pipe applications. *Int. J. Heat Mass Transfer* **2012,** *55* (25), 7471-7486.
210. Zhang, C.; Rong, G.; Palko, J. W.; Dusseault, T. J.; Asheghi, M.; Santiago, J. G.; Goodson, K. E. In *Tailoring of Permeability in Copper Inverse Opal for Electronic Cooling Applications*, ASME 2015 International Technical Conference and Exhibition on Packaging and Integration of Electronic and Photonic Microsystems San Francisco, CA, San Francisco, CA, 2015; p V002T06A004.
211. Dusseault, T. J.; Gires, J.; Barako, M. T.; Yoonjin, W.; Agonafer, D. D.; Asheghi, M.; Santiago, J. G.; Goodson, K. E. In *Inverse opals for fluid delivery in electronics cooling systems*, IEEE Intersociety Conference on Thermal and Thermomechanical Phenomena in Electronic Systems (ITherm), Orlando, FL, 27-30 May 2014; Orlando, FL, 2014; pp 750-755.

212. Minkowycz, W. J.; Sparrow, E. M., Condensation heat transfer in the presence of noncondensables, interfacial resistance, superheating, variable properties, and diffusion. *Int. J. Heat Mass Transfer* **1966,** *9* (10), 1125-1144.
213. Adera, S.; Antao, D.; Raj, R.; Wang, E. N. In *Hotspot thermal management via thin-film evaporation*, IEEE Intersociety Conference on Thermal and Thermomechanical Phenomena in Electronic Systems (ITherm), Las Vegas, NV, May 31 2016-June 3 2016; Las Vegas, NV, 2016; pp 364-371.
214. Adera, S.; Antao, D.; Raj, R.; Wang, E. N., Design of micropillar wicks for thin-film evaporation. *Int. J. Heat Mass Transfer* **2016,** *101*, 280-294.
215. Lu, Z.; Narayanan, S.; Wang, E. N., Modeling of Evaporation from Nanopores with Nonequilibrium and Nonlocal Effects. *Langmuir* **2015,** *31* (36), 9817-9824.
216. Plawsky, J. L.; Fedorov, A. G.; Garimella, S. V.; Ma, H. B.; Maroo, S. C.; Chen, L.; Nam, Y., Nano- and Microstructures for Thin-Film Evaporation—A Review. *Nanoscale Microscale Thermophys. Eng.* **2014,** *18* (3), 251-269.
217. Xiao, R.; Maroo, S. C.; Wang, E. N., Negative pressures in nanoporous membranes for thin film evaporation. *Appl. Phys. Lett.* **2013,** *102* (12), 123103.
218. Byon, C.; Kim, S. J., Capillary performance of bi-porous sintered metal wicks. *Int. J. Heat Mass Transfer* **2012,** *55* (15), 4096-4103.
219. Semenic, T.; Catton, I., Experimental study of biporous wicks for high heat flux applications. *Int. J. Heat Mass Transfer* **2009,** *52* (21), 5113-5121.
220. Hwang, G. S.; Nam, Y.; Fleming, E.; Dussinger, P.; Ju, Y. S.; Kaviany, M., Multi-artery heat pipe spreader: Experiment. *Int. J. Heat Mass Transfer* **2010,** *53* (13), 2662-2669.
221. Liu, T.; Lingamneni, S.; Palko, J.; Asheghi, M.; Goodson, K. E. In *Optimization of hybrid wick structures for extreme spreading in high performance vapor chambers*, IEEE Intersociety Conference on Thermal and Thermomechanical Phenomena in Electronic Systems (ITherm), Las Vegas, NV, IEEE: Las Vegas, NV, 2016; pp 30-36.
222. Ćoso, D.; Srinivasan, V.; Lu, M.-C.; Chang, J.-Y.; Majumdar, A., Enhanced Heat Transfer in Biporous Wicks in the Thin Liquid Film Evaporation and Boiling Regimes. *J. Heat Transfer* **2012,** *134* (10), 101501-101501-11.
223. Patil, C. M.; Kandlikar, S. G., Review of the Manufacturing Techniques for Porous Surfaces Used in Enhanced Pool Boiling. *Heat Transfer Eng.* **2014,** *35* (10), 887-902.
224. Dai, X.; Famouri, M.; Abdulagatov, A. I.; Yang, R.; Lee, Y.-C.; George, S. M.; Li, C., Capillary evaporation on micromembrane-enhanced microchannel wicks with atomic layer deposited silica. *Appl. Phys. Lett.* **2013,** *103* (15), 151602.
225. Dai, X.; Yang, F.; Yang, R.; Lee, Y.-C.; Li, C., Micromembrane-enhanced capillary evaporation. *Int. J. Heat Mass Transfer* **2013,** *64*, 1101-1108.
226. Farokhnia, N.; Irajizad, P.; Sajadi, S. M.; Ghasemi, H., Rational Micro/Nanostructuring for Thin-Film Evaporation. *J. Phys. Chem. C* **2016,** *120* (16), 8742-8750.
227. Narayanan, S.; Fedorov, A. G.; Joshi, Y. K., Gas-Assisted Thin-Film Evaporation from Confined Spaces for Dissipation of High Heat Fluxes. *Nanoscale Microscale Thermophys. Eng.* **2009,** *13* (1), 30-53.
228. Narayanan, S.; Fedorov, A. G.; Joshi, Y. K. In *Gas Assisted Thin-Film Evaporation for Hotspot Thermal Management*, International Heat Transfer Conference, Washington, DC, Washington, DC, 2010; pp 671-674.

229. Narayanan, S.; Fedorov, A. G.; Joshi, Y. K., Heat and mass transfer during evaporation of thin liquid films confined by nanoporous membranes subjected to air jet impingement. *Int. J. Heat Mass Transfer* **2013,** *58* (1), 300-311.
230. Krein, P. T., *Elements of power electronics*. Oxford University Press: New York, 1998; p xviii, 766 p.
231. Kassakian, J. G.; Jahns, T. M., Evolving and Emerging Applications of Power Electronics in Systems. *Ieee J Em Sel Top P* **2013,** *1* (2), 47-58.
232. Lei, Y.; Barth, C.; Qin, S.; Liu, W.; Moon, I.; Stillwell, A.; Chou, D.; Foulkes, T.; Ye, Z.; Liao, Z.; Pilawa-Podgurski, R. C. In *A single-phase, 7-level, gan inverter with an active energy buffer achieving 216 w/in3 power density and 97.6% peak efficiency*, Applied Power Electronics Conference and Exposition (APEC), Long Beach, CA, IEEE, Ed. IEEE: Long Beach, CA, 2016.
233. Faghri, A., *Heat pipe science and technology*. 2nd ed.; Global Digital Press: Columbia, MO, 2010.
234. Barth, C. B.; Foulkes, T.; Chung, W.; Modeer, T.; Assem, P.; Lei, Y.; Pilawa-Podgurski, R. C. N. In *Design and control of a GaN-based, 13-level, flying capacitor multilevel inverter*, 2016 IEEE 17th Workshop on Control and Modeling for Power Electronics (COMPEL), Trondheim, Norway, IEEE, Ed. IEEE: Trondheim, Norway, 2016; pp 1-6.
235. Doty, J.; Yerkes, K.; Byrd, L.; Murthy, J.; Alleyne, A.; Wolff, M.; Heister, S.; Fisher, T. S., Dynamic Thermal Management for Aerospace Technology: Review and Outlook. *Journal of Thermophysics and Heat Transfer* **2016,** *0* (0), 1-13
236. Boreyko, J. B.; Chen, C. H., Self-Propelled Dropwise Condensate on Superhydrophobic Surfaces. *Phys Rev Lett* **2009,** *103* (18).
237. Cha, H.; Xu, C.; Sotelo, J.; Chun, J. M.; Yokoyama, Y.; Enright, R.; Miljkovic, N., Coalescence-Induced Nanodroplet Jumping. *Physical Review Fluids* **2016,** *1* (064102).
238. Watson, G. S.; Gellender, M.; Watson, J. A., Self-propulsion of dew drops on lotus leaves: a potential mechanism for self cleaning. *Biofouling* **2014,** *30* (4), 427-434.
239. Chavez, R. L.; Liu, F. J.; Feng, J. J.; Chen, C. H., Capillary-inertial colloidal catapults upon drop coalescence. *Applied Physics Letters* **2016,** *109* (1).
240. Enright, R.; Miljkovic, N.; Alvarado, J. L.; Kim, K.; Rose, J. W., Dropwise Condensation on Micro- and Nanostructured Surfaces. *Nanosc Microsc Therm* **2014,** *18* (3), 223-250.
241. Miljkovic, N.; Wang, E. N., Condensation heat transfer on superhydrophobic surfaces. *Mrs Bull* **2013,** *38* (5), 397-406.
242. Cho, H. J.; Preston, D. J.; Zhu, Y.; Wang, E. N., Nanoengineered materials for liquid–vapour phase-change heat transfer. *Nature Reviews Materials* **2016,** *2* (16092).
243. Shahriari, A.; Birbarah, P.; Oh, J.; Miljkovic, N.; Bahadur, V., Electric-field-based control and enhancement of boiling and condensation. *Journal of Nanoscale and Microscale Thermophysical Engineering* **2016**.
244. Boreyko, J. B.; Zhao, Y. J.; Chen, C. H., Planar jumping-drop thermal diodes. *Applied Physics Letters* **2011,** *99* (23).
245. Boreyko, J. B.; Chen, C. H., Vapor chambers with jumping-drop liquid return from superhydrophobic condensers. *International Journal of Heat and Mass Transfer* **2013,** *61*, 409-418.
246. Miljkovic, N.; Preston, D. J.; Enright, R.; Wang, E. N., Jumping-droplet electrostatic energy harvesting. *Appl Phys Lett* **2014,** *105* (1).

247. Boreyko, J. B.; Collier, P. C., Delayed Frost Growth on Jumping-Drop Superhydrophobic Surfaces. *Acs Nano* **2013,** *7* (2), 1618-1627.
248. Miljkovic, N.; Preston, D. J.; Enright, R.; Wang, E. N., Electrostatic charging of jumping droplets. *Nat Commun* **2013,** *4*.
249. Birbarah, P.; Li, Z. E.; Pauls, A.; Miljkovic, N., A Comprehensive Model of Electric-Field-Enhanced Jumping-Droplet Condensation on Superhydrophobic Surfaces. *Langmuir* **2015,** *31* (28), 7885-7896.
250. Prasher, R., Thermal interface materials: Historical perspective, status, and future directions. *P Ieee* **2006,** *94* (8), 1571-1586.
251. Conversion), E. E. P. *EPC2304 – Enhancement Mode Power Transistor*; 2016.
252. Nam, Y.; Ju, Y. S., A comparative study of the morphology and wetting characteristics of micro/nanostructured Cu surfaces for phase change heat transfer applications. *Journal of Adhesion Science and Technology* **2013,** *27* (20), 2163-2176.
253. Minkowycz, W. J.; Sparrow, E. M., Condensation Heat Transfer in Presence of Noncondensables Interfacial Resistance Superheating Variable Properties and Diffusion. *International Journal of Heat and Mass Transfer* **1966,** *9* (10), 1125-+.
254. Chavan, S.; Cha, H.; Orejon, D.; Nawaz, K.; Singla, N.; Yeung, Y. F.; Park, D.; Kang, D. H.; Chang, Y. J.; Takata, Y.; Miljkovic, N., Heat Transfer through a Condensate Droplet on Hydrophobic and Nanostructured Superhydrophobic Surfaces. *Langmuir* **2016,** *32* (31), 7774-7787.
255. Miljkovic, N.; Enright, R.; Nam, Y.; Lopez, K.; Dou, N.; Sack, J.; Wang, E. N., Jumping-Droplet-Enhanced Condensation on Scalable Superhydrophobic Nanostructured Surfaces. *Nano Letters* **2013,** *13* (1), 179-187.
256. Eggers, J.; Lister, J. R.; Stone, H. A., Coalescence of liquid drops. *J. Fluid Mech.* **1999,** *401*, 293-310.
257. Bergman, T. L.; Lavine, A. S.; Incropera, F. P.; DeWitt, D. P., *Fundamentals of heat and mass transfer*. Wiley: Hoboken, NJ, 2011.
258. Landauer, R., The Electrical Resistance of Binary Metallic Mixtures. *J. Appl. Phys.* **1952,** *23* (7), 779-784.
259. Gong, L.; Wang, Y.; Cheng, X.; Zhang, R.; Zhang, H., A novel effective medium theory for modelling the thermal conductivity of porous materials. *Int. J. Heat Mass Transfer* **2014,** *68* (Supplement C), 295-298.

APPENDICES

Appendix A. Supporting Information for Chapter 2: Exploring the Role of Habitat on the Wettability of Cicada Wings

A.1. Geometric parameters of the cicada wing structures

Nanopillars on the cicada wings are evenly distributed as shown in the AFM and SEM images (see Fig. 2-3 and Fig. 2-5). The topology of the nanopillars can be characterized by geometric parameters such as pitch (P), height (H), diameter (D) and opening angle (α). Pitch is defined as center-to-center distance of two adjacent nanopillars. Height is defined as base-to-tip distance, and diameter is defined as the diameter of the base of nanopillars. Opening angle is defined as the angle formed by the perpendicular line to the base and the external curvature of a nanopillar at the apex.

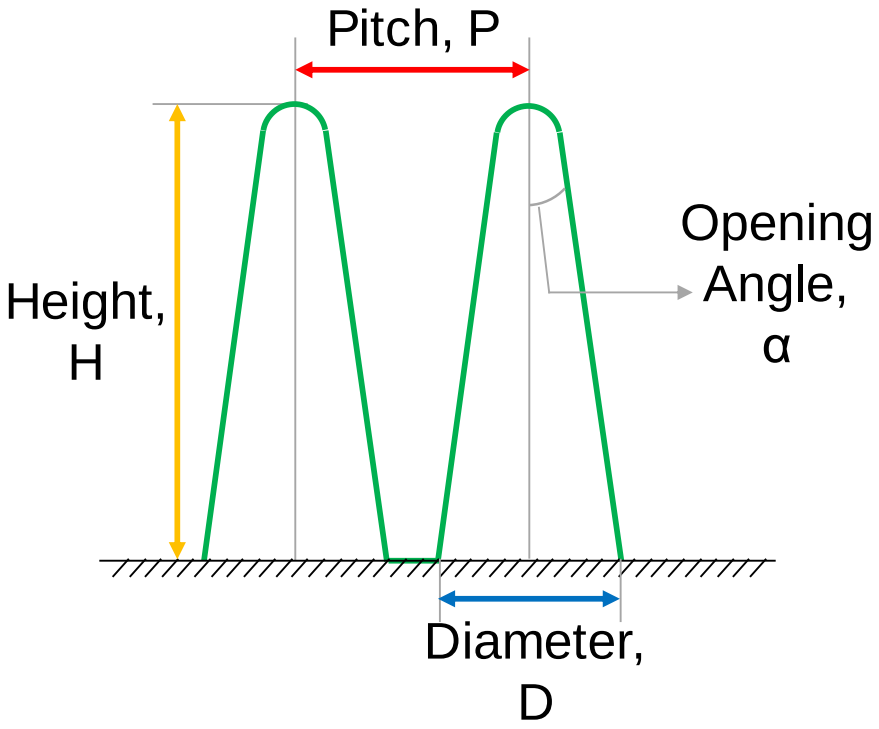

Figure A-1 Topological parameters of nanopillars on a cicada wing.

A.2. Comparison of AFM height profile data for all selected cells

We conducted AFM scans for all selected cells to characterize spatial variations on a wing of a certain species, as well as their special differences. Two cells near the corps (u3, mc) and three peripheral cells (a3, a5, a8) were selected to exhibit better representativeness. Height profile data from all selected cells were provided as in Fig. A-2 for four cicada species. Note, the height profile data were re-zeroed base on the flattened AFM data and the lowest the lowest z-coordinate of the extracted profiles.

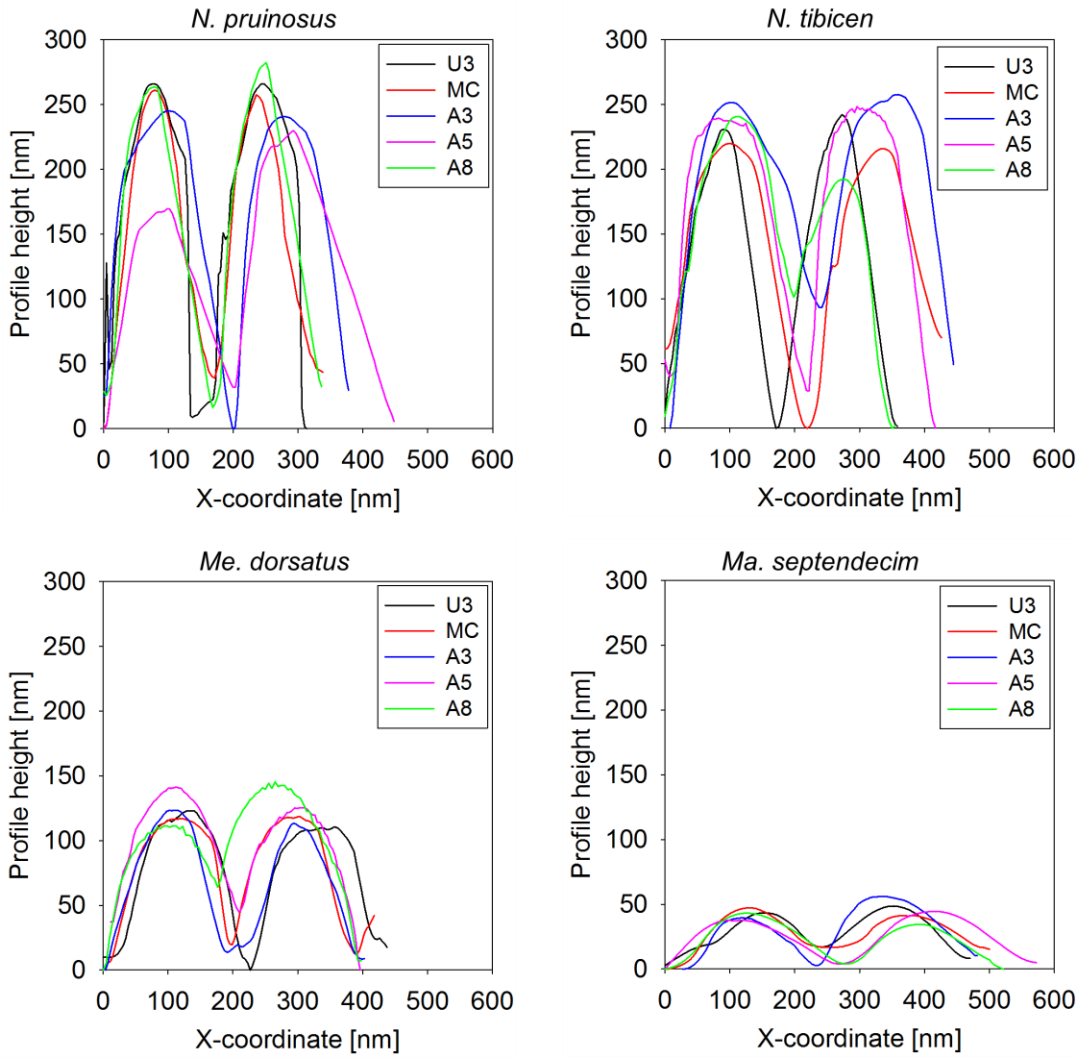

Figure A-2 Height profile of the nanopillars on different species of cicada wings at five different locations on the wings

Appendix B. Fabrication of nanostructure replicated from cicada wings using nanoimprinting lithography

B.1. Methods

This study developed a novel nanoimprinting lithography method (NIL) called dissolvable template nanoimprinting lithography (DT-NIL). We utilized acyrilic polymer based nail poilish to fabricate negative template from original cicada wings as master surfaces. Figure B-1 illustrates the detailed fabrication steps to make replica of nanopillars on cicada wing. First, we applied ~ 2 ml/cm^2 of nail polish on a cicada wing. The resin then was left in the air to dry or exposed UV light (λ=265 nm) for a UV gel resin to be cured using UV crosslinker (Fisher Scientific, Spectroline™ XL1000), at 10 mJ/cm^2 for 600 sec. Drying resin left being cured for 0.5-2 hours to be cured in room temperature, or left immersed in an iced cold water bath to accelerate curing. The cured resin layer carefully peeled off from master, and left cured further in between sterile microscope glass slide to prevent it being rolled back due to residual stress from peeling. The peeled half-cured resin film further cured itself under UV exposure or drying and becomes more rigid and brittle. After removal of the template, original sample was cleaned with acetone in a sonicating bath to get rid of possible stains and residues on sample, followed by IPA wash and N_2 dry to prevent the solvent stain.

Using the template fabricated, we produced replica of the original master from PDMS fabrication and metal electroplating. Thin film of Au was deposited on the template to prevent nanopillars made of PDMS from collapsing after the template dissolving process or to make the template conductive for electroplating as shown in the Fig. B-1b&c. This method is a low-key, room temperature and atmospheric pressure nanoimprinting method, which is applicable to various type

of samples from flexible to rigid, and from engineered to natural surfaces replicating nanostructures.

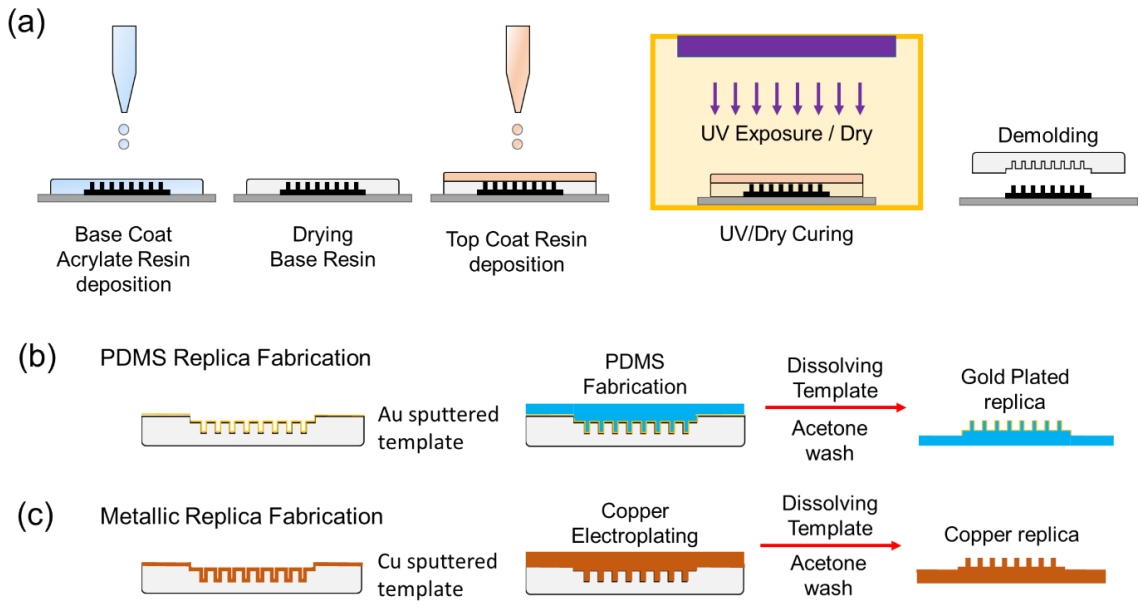

Figure B-1. Schematic diagram of dissolvable template nanoimprinting lithography (DT-NIL). Fabrication of (a) template using acrylic polymer (nail polish) and replica using (b) PDMS (polydimethylsiloxane) and (c) electroplating of Cu

B.2. Replicated Nanopillars on Cicada Wing

Figure B-2 shows the nanopillars on cicada wings and replica wings, and template fabricated for DT-NIL made from the acrylic polymer resin. Fig. B-2a shows the original nanopillars on cicada wing of *Neotibicen pruinosus* (*N. pru*) and B-2b shows the scanning electron microscopy (SEM) and atomic force microscopy (AFM) image of template molded from the original nanostructures of cicada wings. The height of nanopillars on *N. pru* wings were approximately 450 nm, and the well depth from the template from the AFM image were approximately 400 nm, which showed good agreements with the original feature height. The templates were then removed after the

fabrication process using PDMS and metal electroplating. Fig. B-2c,d shows the replica of a *N. pru* cicada wing made from PDMS and the replica generated from copper, respectively.

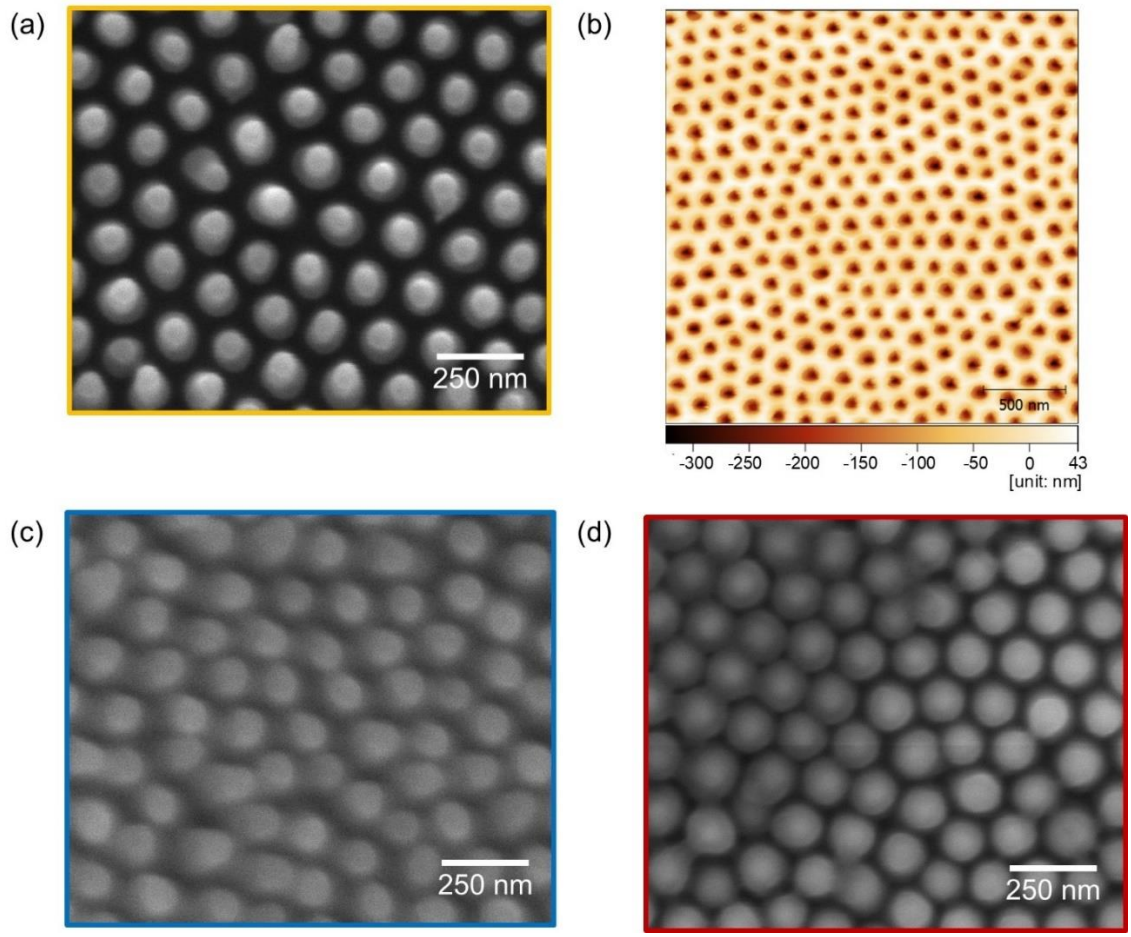

Figure B-2 (a) Scanning electron microscopy (SEM) image of nanopillars on the original *Neotibicen pruinosus* cicada wing and (b) atomic force microscopy (AFM) image of a template fabricated from the original N. pru cicada wing. The scan area was 5 µm by 5 µm showing uniformity of features. SEM image of replica made from (c) PDMS and (d) copper electroplating.

Appendix C. Supporting Information for Chapter 5: Thin Film Condensation on Nanostructured Surfaces

C.1. ToF-SIMS Analysis

To elucidate the surface chemistry after polyimide (Kapton, $[C_{22}H_{10}N_2O_5]_n$) decomposition and re-deposition on the surface, we conducted a Time-of-Flight Secondary Ion Mass Spectroscopy (ToF-SIMS) analysis on the inverse opal structure.

Figure C-1 show the mass spectral data of positive secondary ions for decomposed polyimide coated NIO. We observed the presence of polymers consisted of carbon, nitrogen and hydrogen such as $C_4H_{11}N$ (73 amu) or $C_6H_{19}N_4$ (147 amu) for the coated NIO surface indicating the presence of polymers decomposed from polyamide and radicals on the surface that re-deposited after decomposition at elevated temperatures.

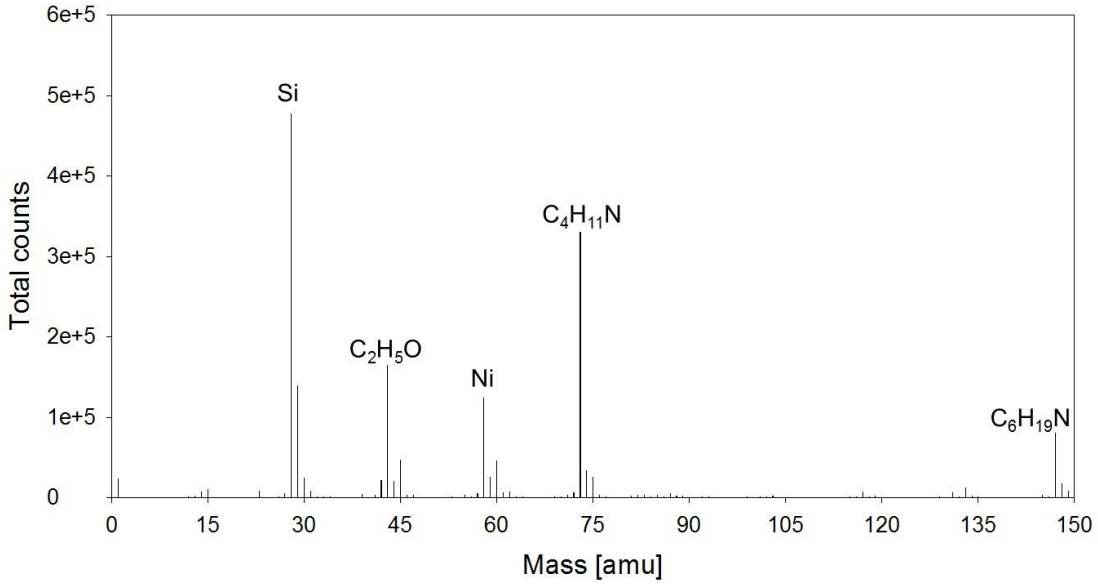

Figure C-1 Mass spectra of positive secondary ion from polymer coated hydrophobic NIO surface obtained using Time-of-Flight Secondary Ion Mass Spectroscopy (ToF-SIMS).

C.2. Derivation of Bridge Impinging Velocity

To explain the capillary suction phenomena, we begin by examining the hydrodynamics of droplet coalescence between two equally sized droplets on the superhydrophobic NIO top layer. Immediately after the interfaces of the two droplets touch, a radially accelerating liquid bridge develops due to the curvature difference between the bridge radius ($1/\mathrm{r_b}$) and the radii of the coalescing droplets ($1/R$). For the droplet length scales of coalescing droplet observed here (R < 20 μm), the Ohnesorge number $Oh = \mu/(\rho\gamma R)^{1/2}$, where μ (= 1.73mPa·s), ρ (= 999.85 kg/m^3), and γ (=75.5 mN/m) are the water dynamic viscosity, density, and surface tension, respectively, corresponds to Oh > 0.044. For Oh < 1, droplet coalescence occurs in two distinct regimes[203, 205]. When $r_b/R < Oh$, droplets undergo coalescence in the inertially limited viscous regime, where growth of the bridge radius is governed by a balance between viscous, inertial, and surface tension forces $r_{b,v} = \gamma\tau/\mu$, where τ is time. As the liquid bridge proceeds to grow and reaches $r_b/R < Oh$, the droplets enter the inertially limited regime where growth of the bridge radius is governed by a balance between inertia and surface tension forces as[256]:

$$r_b = D_0 \left(\frac{\gamma R}{\rho}\right)^{1/4} \tau^{1/2} \qquad \textbf{(}\text{Eq. C-1)}$$

where D_0 is a constant with value ranging between 1.39 and 1.62[202-205]. We obtain the velocity of the bridge $u(\tau)$ by taking time derivative of the bridge radius as:

$$\frac{dr_b}{d\tau} = u(\tau) = D_0 \left(\frac{\gamma R}{\rho}\right)^{1/4} \frac{d}{d\tau}(\tau^{1/2}) = D_0 \left(\frac{\gamma R}{\rho}\right)^{1/4} \frac{2}{\sqrt{\tau}} \qquad \text{(Eq. C-2)}$$

When the bridge radius reaches the NIO surface ($r_b = R$), the time at initial contact ($\tau = \tau_c$) can be solved by substituting $r_b = R$ into Eq. C-1, solving for $\tau = \tau_c$ and subsequently solving for the liquid-bridge velocity at initial contact (U) as:

$$\tau_c = \tau(r_b = R) = \frac{R}{D_0}\left(\frac{\gamma R}{\rho}\right)^{1/4} \quad \text{(Eq. C-3)}$$

$$U = U(\tau = \tau_c) = 2{D_0}^2\left(\frac{\gamma}{\rho R}\right)^{1/2} \quad \text{(Eq. C-4)}$$

The water hammer pressure (static pressure) generated by the impinging liquid bridge scales as $P_{infiltration} \sim \rho U^2$. If the pressure induced by impinging overcomes the capillary pressure barrier ($P_{infiltration} > P_{cap} = 2\gamma/r_p$), the bridge will connect with the liquid residing in the superhydrophilic sub-layer and wick into the porous structure. Indeed, scaling of the two competing pressures reveals a dependence of coalescing droplet radii (*R*) on the pore neck radius as:

$$P_{infiltration} > P_{cap} \quad \text{(Eq. C-5)}$$

$$\rho U^2 = 4\rho {D_0}^4 \frac{\gamma}{\rho R} \sim \frac{2\gamma}{r_p} \quad \text{(Eq. C-6)}$$

$$R < 2{D_0}^4 r_p \quad \text{(Eq. C-7)}$$

C.3. Derivation of the Viscous Pressure Drop (ΔP_v)

The NIO structures fabricated in this study can be considered as porous media whose porosity is approximately 0.8. Darcy's law states that the viscous pressure drop (ΔP_v) through a porous medium for a flowing fluid is related to the volumetric flow rate (Q'), viscosity (μ), permeability (κ), flow length (L), and flow cross section area (A_c) by:

$$Q' = \frac{-\kappa A_c \Delta P_v}{\mu L} \quad \text{(Eq. C-8)}$$

The flow area can be related to the porous structure thickness (t) as $A_c = Lt$, while the mass flow rate ($\dot{m}$) can be related to the volumetric flow rate via the fluid density (ρ) as $\dot{m} = \rho Q'$. Back substituting these relations into Eq. C-8, we obtain:

$$\Delta P_v = \frac{\mu \dot{m}}{\kappa \rho t} \quad \text{(Eq. C-9)}$$

To relate the Darcy flow to the condensation rate, we can first relate the condensation heat transfer (Q) to the latent heat of vaporization (h_{fg}) as:

$$Q = hA\Delta T = \dot{m} h_{fg} \quad \text{(Eq. C-10)}$$

where h is the condensation heat transfer coefficient, A is the condensation area ($A=L^2$), ΔT is the temperature difference between the vapor pressure and wall temperature ($\Delta T = T_v - T_c$).

By rearranging Eq. C-9 and C-10 with respect to mass flow rate ($\dot{m}$) of condensate, we can relate the viscous pressure drop through the porous media with the rate of the condensation obtained from heat transfer as shown in the Eq. C-11.

$$\Delta P_v = \frac{hL^2 \Delta T \mu}{h_{fg} \kappa \rho t} \quad \text{(Eq. C-11)}$$

C.4. Detailed Darcy Flow Analysis

The thin film condensation behavior on inverse opal structures is governed by the viscous pressure drop across the porous medium (ΔP_v, Appendix C.3.), and the Laplace pressure of a droplet emerging from the top of a pore (ΔP_c):

$$\Delta P_c = \frac{2\sigma}{r_p} \quad \text{(Eq. C-12)}$$

where r_p is the radius of the top pore, and σ is the surface tension of the condensate. If the viscous pressure drop exceeds the Laplace pressure barrier pressure drop ($\Delta P_v > \Delta P_c$), the condensate will burst out of the top pores, which will eventually result in flooded condensation as illustrated by the shaded region in orange in Figure 5.5 in Chapter 5. Otherwise, when $\Delta P_v < \Delta P_c$ (green-shaded region), liquid condensate will be confined and propagate inside the structure.

In Eq. C-11, we derived the viscous pressure drop induced via conservation of mass applied to the condensate flowing laterally through the porous structure. The flow length (L) was assumed to be the distance from the center of the sample to the edge. However, condensate does not all originate at the center of the sample, making Eq. C-11 a conservative estimate of viscous pressure drop. In order to compute the non-linear pressure drop along the sample length as condensate accumulates, we discretized the condensation domain and utilized a mass balance approach (Figure C-3a). We numerically modeled a 1 cm-long thin porous structure discretized into 1 mm sections (L =1 mm) as shown in Figure C-2(a) to determine the effect of different pore size (r_p = 100 nm and 1 μm) with varying condensation heat transfer (h) on condensate viscous pressure drop across the structure from center ($x = 0$) to edge ($x = 5L$). To account for the incremental addition of mass in each discretized section, we first determined the mass flow rate of condensate in the first discretized domain (n = 1) using the condensation heat transfer coefficient and latent heat of phase

change ($Q = \dot{m}h_{fg} = hA\Delta T = h(2L)^2\Delta T$). After determining the mas flow rate, we calculated the viscous pressure drop via Eq. C-11 assuming L = 1 mm. After computing for n = 1, we then moved to the n = 2 domain taking into account the increased condensation area. By summing the pressure and mass flow rate from each previous domain solution, we were able to determine the pressure drop up in the n^{th} discretized section as:

$$\Delta P_{v,n} = \frac{h(2nL)^2\Delta T\mu(5-n)}{h_{fg}\kappa\rho n^2 t} \quad \text{(Eq. C-13)}$$

$$\Delta P_{v,tot} = \sum_{k=1}^{n} \Delta P_{v,6-k} \quad \text{(Eq. C-14)}$$

Figure C-2(b) shows the gauge pressure inside the porous structure as a function of the distance from the center of the square structure (Figure C-2a) for small (100 nm) and large (1 µm) pores. As expected, using larger size pores, the viscous pressure drop becomes 100X smaller for the same condensation heat transfer conditions (100 kW/m^2·K). Note, the calculated total viscous pressure drop is approximately 10X smaller than the conservative estimate using Eq. C-11.

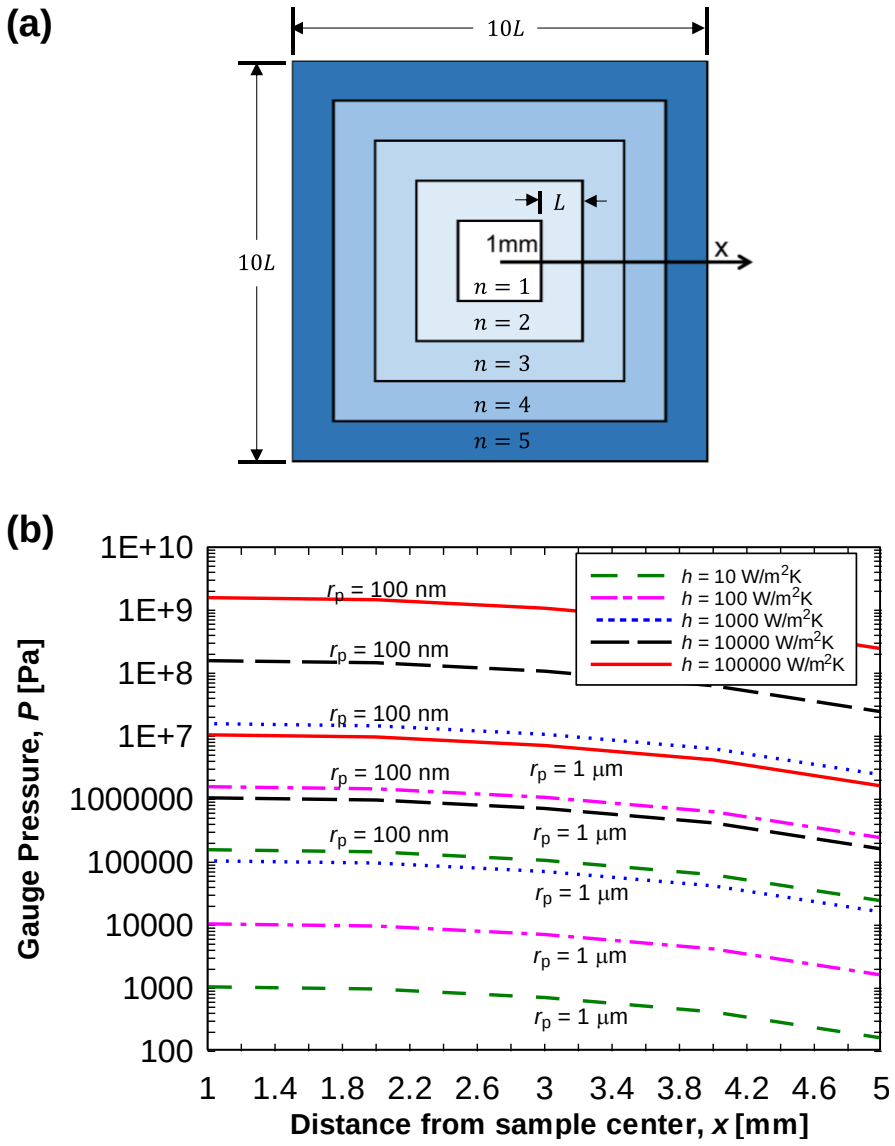

Figure C-2 (a) Schematic diagram of the modeled porous structure and (b) gauge pressure across the surface with smaller (100 nm) and larger (1 μm) pores. All calculations done at ΔT= 5 K.

C.5. Analytical Models of Thin Film and Filmwise Condensation

Thin Film Condensation. We developed an analytical heat transfer modeling of thin film condensation to quantify and validate the effectivity of thin film condensation compared to the dropwise condensation. The local condensation heat transfer coefficient on a thin liquid film layer (h_x) can be modeled as conduction through the layer as related by the condensation heat flux (q'') temperature difference between the vapor and wall ($\Delta T = T_v - T_c$), thermal conductivity of the condensate (k_f), liquid film thickness (t), solid fraction (φ), and condensation heat transfer coefficient:

$$\frac{q''}{\Delta T} = h_x = \frac{k_f(1-\phi)}{t} \quad \text{(Eq. C-15)}$$

Note, here we made the important assumption that the condensation process is limited by conduction through the liquid film, and that the interfacial heat transfer coefficient (h_i) at the liquid-vapor interface due to accommodation of condensing vapor molecules is much higher (h_i ≈ 500 kW/m^2·K) than the effective local heat transfer coefficient due to conduction ($h_x < h_i$). This assumption is deemed appropriate due to the high accommodation coefficient of clean water and previous studies showing that conduction through the liquid film dominates. A second major assumption to the model is related to the nature of heat transfer. We assume that condensation only occurs on the exposed liquid vapor interface, and that no-heat transfer occurs via heat conduction through the inverse opal structures. Although not exact, this assumption acts as a conservative estimate given the low thermal conductivity of water. The presence of NIO nanostructures will only act to increase the overall thermal conductivity and thin film performance.

Filmwise Condensation. To model filmwise condensation on a vertical flat plate, we utilized the laminar filmwise condensation Nusselt analysis[257]. For a vertically aligned (gravity parallel to the

surface) plate of length LL, assuming laminar condensate flow, quiescent vapor conditions, constant vapor to surface temperature difference (ΔT), condensate density (ρ_f) and dynamic viscosity (μ), vapor density (ρ_g), gravitational acceleration (g), and latent heat of vapor to liquid phase change (h_{fg}), the film thickness (t) can be formulated as:

$$\delta(L) = \left(\frac{4k_f \Delta T \mu L}{\rho_f(\rho_f - \rho_g) g h_{fg}}\right)^{1/4} \quad \text{(Eq. C-16)}$$

Assuming pure conduction through the liquid film, the average condensation heat transfer coefficient over the whole vertical plate becomes:

$$\overline{h} = \frac{4}{3}\left(\frac{\rho_f(\rho_f - \rho_g) g h_{fg} {k_f}^3}{4\Delta T \mu L}\right)^{1/4} \quad \text{(Eq. C-17)}$$

C.6. Thin Film Condensation Heat Transfer Effective Thermal Conductivity

In section C-5, we derived the analytical heat transfer model of thin film condensation. We assumed the thin film to be composed of water (k_f) and void fraction (φ) for thermal conductivity calculations as in Eq. C-15, to estimate the heat transfer using a conservative approach. Here, we calculate the heat transfer in more realistic manner by more accurately treating the thermal conductivity of the thin film using a linear relation with solid fraction (φ). For the thermal conductivity of water (k_f= 0.68 W/m·K) and nickel (k_{Ni} ≈ 91 W/m·K):

$$k_{eff} = (1 - \varphi)k_f + \varphi k_{Ni} \quad \text{(Eq. C-18)}$$

To obtain higher fidelity, we also used a more complex model (Maxwell-Garnett equation) based on the effective medium theory (EMT) as:[258-259]

$$k_{eff,EMT} = k_{Ni}\left(\frac{2k_{Ni} + k_f + 2\varphi(k_{Ni} - k_f)}{2k_{Ni} + k_f - \varphi(k_{Ni} - k_f)}\right) \quad \text{(Eq. C-19)}$$

Figure C-3(a) shows the comparison of thermal conductivity calculated with the aforementioned methods. The thermal conductivity based on the simple linear model with a Ni solid fraction of ϕ= 0.3 was k_{eff} = 27.8 W/m·K. On the other hand, the thermal conductivity based on EMT was $k_{eff,EMT}$=20.8 W/m·K. These results were calculated at an approximate porosity of inverse opal structure (φ = 0.3), where the manuscript results were k_{eff} = 0.47 W m^{-1} K^{-1}. From this calculation, as shown in Figure C-3(b), the k_{eff} that we used in the manuscript predicted the heat transfer coefficient more conservatively, nearly two orders lower magnitude lower compared to that possible with the more accurate $k_{eff,EMT}$. The effect of using a more accurate effective thermal conductivity not only increases the thin film condensation heat transfer, but allows for the use of thicker structure (*t*), resulting in significantly reduced viscous pressure drop and hence higher possible heat fluxes (Figure 5-5 in Chapter 5).

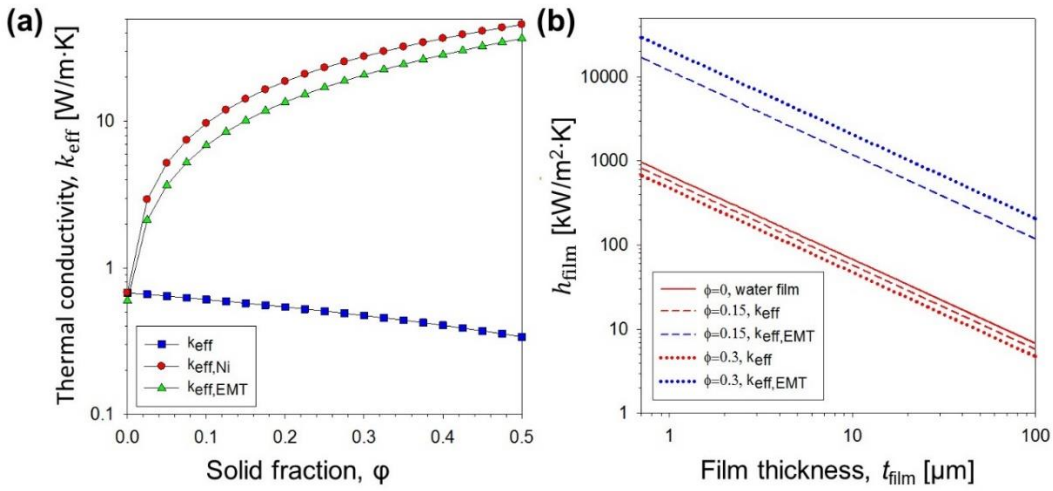

Figure C-3 Comparison of different effective thermal conductivity models of NIO for heat transfer coefficient estimation. (a) Thermal conductivity calculated using 1) void fraction and water film (blue symbols), 2) effective medium theory (EMT) (green symbols), and 3) solid fraction with NIO and water (red symbols). (b) Thin film condensation heat transfer coefficient versus film thickness predicted with k_{eff} and $k_{eff,EMT}$ for a water film and thin film where solid fraction (φ) is 0.15 and 0.3 (similar to the NIO sample studied in this study).

C.7. Thin Film Condensation in Bi-Porous Structures

In order to calculate the hydrodynamic performance of bi-porous thin film condensation, we modified the hydrodynamic model to decouple the viscous pressure loss (Eq. C-11) and the Laplace pressure barrier (Eq. C-12) by assuming two differing pore size radii. Figure C-4 shows the pressure drop as a function of superhydrophilic sub-layer pore size for a bi-porous structure with a top layer pore size of r_p = 100 nm. The results show that the accessible thin film region is expanded when compared to a monodisperse porous structure, enabling condensation heat transfer coefficients of > 100 kW/m^2·K to be reached (green shaded region).

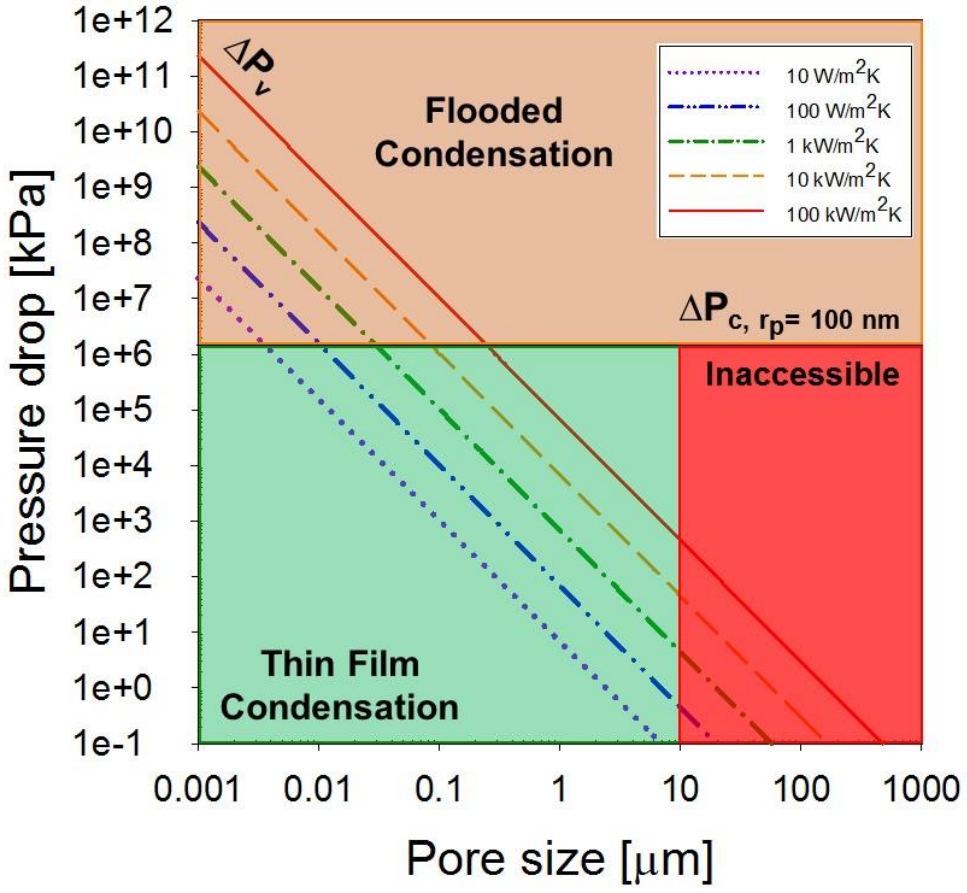

Figure C-4 Comparison of hydrophobic barrier pressure drop (ΔP_c, black horizontal solid line) and viscous pressure drop through (ΔP_v, colored lines) as a function of superhydrophilic sub-layer pore size (r_p) for different heat condensation transfer coefficients and film thickness, t_{film} = 10 μm. To prevent flooding and ensure stable thin film condensation, the viscous pressure drop from the sample center to the edge must be lower than the barrier pressure drop ($\Delta P_v < \Delta P_c$, green shaded area). If the viscous pressure drop exceeds the barrier pressure drop ($\Delta P_v > \Delta P_c$, orange shaded area), liquid will propagate through the top structures and flood the surface. The red shaded area labeled inaccessible represents the length scale at which the pore size is greater than the film thickness.

Appendix D. Supporting Information for Chapter 7: Jumping Droplets Electronics Hot Spot Cooling

D.1. Detailed Heat Transfer Modeling

Figure D-1 shows the thermal circuit corresponding with the experimental setup. The GaN transistor is considered with a lumped temperature T_G. Joule heating is generated inside the GaN at a rate of RI^2 where $R = 0.007 \pm 0.002\ \Omega$ is the internal electrical resistance of the GaN transistor, and $I = 15$ A is the current flowing through the transistor. The heat is dissipated either to the backside (through the board, then to ambient air, $T_{amb} = 23 \pm 1$°C), either to the front side (towards the superhydrophobic sample, $T_s = 5 \pm 1$°C). Miscellaneous losses to ambient air have been lumped into a thermal resistance R_{losses}. Table C-1 summarizes the parameters used.

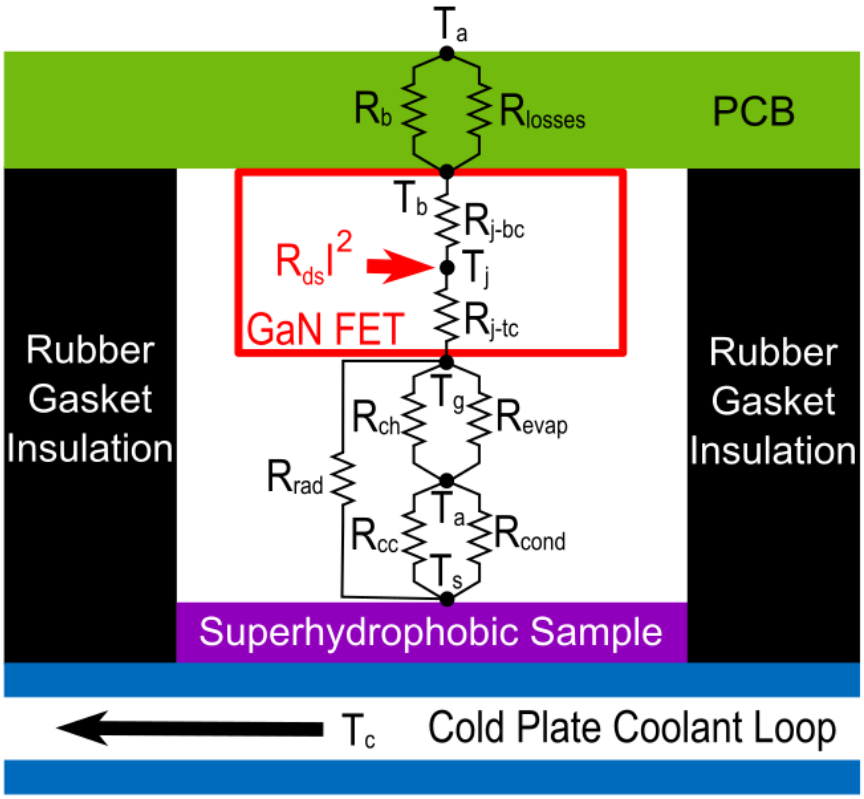

Figure D-1 Thermal circuit of the experimental setup

Table D-1 Summary of thermal parameters used

Symbol / Equation	Thermal Resistance	Value (K/W)
$R_{\mathrm{B}} = R_{\mathrm{sp}} + R_{\mathrm{nat}}$	Backside resistance	79.2
R_{sp}	Spreading resistance within the PCB	47.2
$R_{\mathrm{nat}} = \frac{1}{h_{\mathrm{nat}} A_{\mathrm{PCB}}}$	Natural convection on the PCB	32
R_{losses}	Miscellaneous thermal losses to ambient air	-
$R_{\mathrm{ch}} = \frac{1}{h_{\mathrm{ch}} A_{\mathrm{GaN}}}$	Natural convection at the hot side	4806
$R_{\mathrm{cc}} = \frac{1}{h_{\mathrm{cc}} A_{\mathrm{s}}}$	Natural convection at the cold side	80
$R_{\mathrm{evap}} = \frac{1}{h_{\mathrm{evap}} A_{\mathrm{GaN}}}$	Evaporation of jumping droplets	-
$R_{\mathrm{cond}} = \frac{1}{h_{\mathrm{cond}} A_{\mathrm{s}}}$	Condensation on the superhydrophobic sample	0.4
$R_{\mathrm{rad}} = \frac{1}{h_{\mathrm{rad}} A_{\mathrm{GaN}}}$	Radiation thermal resistance	1114

The heat transfer coefficients and areas are as expressed in Table D-1, and: $h_{\mathrm{rad}} = \sigma({T_G}^2 + {T_S}^2)(T_G + T_S)$, $\sigma =$ 5.67x10-8 W/m^2·K^4 is Stephan-Boltzmann's constant, $A_{\mathrm{PCB}} = 62$ cm^2 is the PCB backside surface area.

The spreading resistance was found by:

$$R_{\mathrm{sp}} = \frac{\tan^{-1}\left[\frac{a+b}{c} - \frac{\pi}{4}\right]}{\pi c k_{\mathrm{PCB}}} \quad \text{(Eq. D-1)}$$

where a = 1.6 mm and b = 5.2 cm are thickness and width of PCB, respectively, and c = 1.8 mm represents the radius of the GaN if it were a circular spot. The thermal conductivity of the PCB, k_{PCB}, is found by:

$$k_{\mathrm{PCB}} = f_t k_{\mathrm{PCB},t} + (1 - f_t) k_{\mathrm{PCB},n} \quad \text{(Eq. D-2)}$$

$$k_{\mathrm{PCB},t} = \frac{k_{\mathrm{FR4}} t_{\mathrm{FR4}} + k_{\mathrm{Cu}} t_{\mathrm{Cu}}}{t_{\mathrm{FR4}} + t_{\mathrm{Cu}}} \quad \text{(Eq. D-3)}$$

$$k_{\mathrm{PCB},n} = \left(\frac{t_{\mathrm{FR4}}}{t_{\mathrm{FR4}} + t_{\mathrm{Cu}}} \frac{1}{k_{\mathrm{FR4}}} + \frac{t_{\mathrm{Cu}}}{t_{\mathrm{FR4}} + t_{\mathrm{Cu}}} \frac{1}{k_{\mathrm{Cu}}}\right)^{-1} \quad \text{(Eq. D-4)}$$

where $t_{\mathrm{Cu}} = 140$ µm is the thickness of copper layers, t_{FR4} =302.5 µm is the thickness of FR4 layers, $k_{\mathrm{PCB},t}$ is tangential thermal conductivity weighted by f_t and $k_{\mathrm{PCB},n}$ is normal thermal conductivity, which has been weighted to 95% as most of the spreading was normal in this geometry. In order to determine the value of the miscellaneous losses in our system, we plotted the results of h_{evap} in terms of the GaN temperature for different values of R_{losses}, as shown in Figure D-2. Experimentally, without jumping droplets ($h_{\mathrm{evap}} = 0$), the temperature of the GaN was determined to be 90 ± 1°C which results in R_{losses}= 100 ± 5 K/W. With this value of R_{losses}, we can determine the value of h_{evap} for different GaN temperatures.

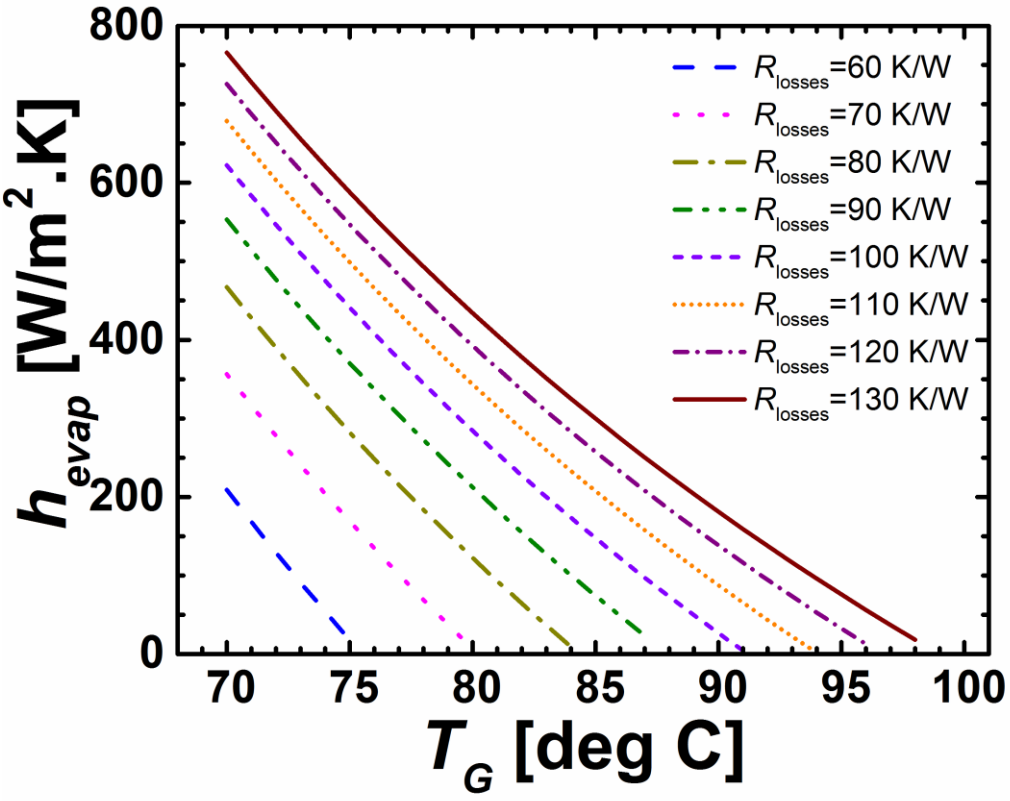

Figure D-2 Evaporation heat transfer coefficient in terms of the GaN temperature for different values of R_{losses}.

D.2. Probing Thermal Steady State of System

Two different schemes were employed to verify independently both the thermocouple measurements of the GaN devices and the PCB and the model for the spreading resistance in the PCB. First, an infrared (IR) camera can provide a map of heat spreading such as Figure 7-2a but not absolute temperature measurements because emissivity of the PCB and components are difficult to determine. For this experiment, a piece of opaque Kapton was placed on the PCB to provide a reference emissivity of approximately 0.95 to calibrate the IR measurement.

In contrast, thermochromic liquid crystals (TLCs) are a tool to observe the absolute temperature of the circuit. TLCs reflect visible light in response to temperature. The TLCs from LCR Hallcrest (Product #: SPN100R70C20W) used in this study had an activation temperature of 70°C and a bandwidth of 20°C. The printed circuit board (PCB) and components were coated with black paint before applying the TLCs such that all reflected light would correspond to a continuous mapping of color to temperature from 70°C (red) to 90°C (violet). Both the black paint and the TLCs were applied uniformly using an airbrush. The time delayed images of Figure 6-2c track how the heat map changes as the system approaches thermal steady state for a continuous drain current of 15 A in each transistor. Specifically, the images corresponding to t=10s and t=30s highlight the validity of the assumption that the spreading resistance follows a three dimensional ellipsoid. Thus, the measurement obtained with the TLCs supplements the IR and the thermocouple measurements with an independent probe of the system's heat map during thermal steady state.